Stability of the Structure in Multicomponent Flows

Thesis by

Harri Kaarlo Kytömaa

In Partial Fulfillment of the Requirements

for the Degree of

Doctor of Philosophy

California Institute of Technology

Pasadena, California

1987

(Submitted October 1, 1986)

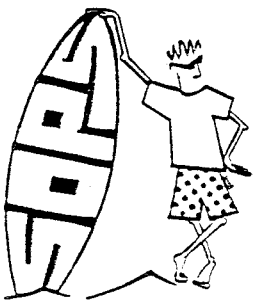

ACKNOWLEDGEMENTS.

I wish to express my deepest gratitude to my advisor Professor Christopher Brennen for his guidance of my graduate studies. Not only is he dedicated to scientific advancement, but also to education. My thanks go to Professor Rolf Sabersky for his support during my graduate studies.

The contributions from a professional group of people enabled the completion of this dissertation. Elmer Szombathy provided quality machining and advice during the building of the apparatus. Technical assistance was also provided by Elton Daly, Joe Fontana and Lou Johnson and his team. Expedient administrative support was provided by Susan Berkley, Jackie Beard and Jan Patterson. I thank them all for making this study possible.

I extend my thanks to the people of the Caltech Gravity Physics Laboratory headed by Professor Ronald Drever, for kindly allowing access to their equipment.

This work was partly supported by The Jet Propulsion Laboratory and the Department of Energy under the NASA/DOE Interagency Agreement No.DE-A101-82-FE-21002.

Thanks go to my colleagues Nick Jones, Luca d'Agostino, Scott Patton and Mike Moser who contributed helpful suggestions and were always available to discuss work-related problems.

I would especially like to thank my parents for their support throughout my studies. Their ambitions and encouragement have always been a strong source of inspiration.

I am indebted to Sirkku Konttinen for her patience and caring during the studies that have led to the completion of this work. I dedicate this thesis to her.

ABSTRACT.

Friction pressure drop measurements were made in vertical bubbly and particulate flows, and friction factors up to two orders of magnitude higher than pure liquid values were obtained. The two-phase friction multiplier for air-water flows was shown to attain values up to 15 times higher than the predictions given by the Lockhart & Martinelli correlations (1949). These findings exemplify the lack of detailed understanding of multi-component flow phenomena. The lack of understanding of the flow kinematics and the small amount of information available on the topic has been primarily due to the primitive stage of development of flow measuring instrumentation.

A shielded, temperature compensated and non-intrusive Impedance Volume Fraction Meter (IVFM) was built and shown to have good spatial and temporal resolution. The dynamic calibration of the device demonstrated that the volume fraction measuring device could also be used to measure both the dispersed medium velocity and concentration. This device enabled us to carry out measurements of small and large amplitude kinematic stability and wave propagation in two-component and three-component flows. The velocities of small amplitude kinematic waves in both air-water and solids-water flows were measured using a cross-correlation technique and these were shown to be non-dispersive. The persistence of flow structure was quantified using the coherence of the IVFM noise at two locations. The structure in solids-water flows was found to be more persistent than in air-water flows, and the most coherent wave length was measured to be of the order of .5 m, or five pipe diameters in both flows. The statistical properties in the inherent noise in the IVFM output was shown to contain valuable information on two- and three-component flow quantities and regime.

In this thesis, we show that much can be learned about the complex nature

of multi-component flows with adequate instrumentation, and we emphasize the need for further development of critical flow measuring techniques for use not only in fundamental investigations but also in the monitoring and control of practical multiphase flow processes.

TABLE OF CONTENTS.

LIST OF FIGURES.

NOMENCLATURE.

A	Cross-sectional area of pipe.
A	Parameter of the liquid friction factor fit.
B	Parameter of the liquid friction factor fit.
B_i	Buoyancy force on particle of species i.
C_D	Drag coefficient of particle or bubble.
C_i	Propagation speed of infinitesimal kinematic waves.
C_s	Propagation speed of kinematic shocks.
D	Pipe diameter.
D_p	Particle diameter.
D_{ij}	Rate of change of flux of component i with respect to the volume fraction of component j.
f_i	Dimensionless velocity of disperse component i relative to liquid.
$f_{1\phi}$	Friction factor in pure liquid flow.
$f_{2\phi}$	Friction factor in two-component flow.
F_D	Drag force on particle or bubble.
Fr	Froude number ($= V_0/\sqrt{gD_p}$).
g	Gravitational acceleration.
h	Separation between IVFM's.
$h(\tau)$	Filter function of IVFM.
H	Amplitude of IVFM filter function.
i	$\sqrt{-1}$.
j	Volumetric flux.
j_{dj}	Drift flux of disperse material.
k(N)	Attenuation time constant of small amplitude kinematic perturbations corresponding to the measured ζ.

K	Added mass coefficient (=1/2).
L	Separation of pressure tappings.
m	IVFM calibration slope (V/%).
n	Dimensionless wave number of kinematic perturbations.
N	Wave number of small amplitude kinematic perturbations.
p	Liquid pressure.
q	Generic variable.
Q	Amplitude of generic variable.
r	Correlation coefficient of regression fit.
$R_{\tilde{V}\tilde{V}}(\tau)$	Auto-correlation function of the fluctuating IVFM signal.
$R_{\tilde{V}_1\tilde{V}_2}(\tau)$	Cross-correaltion function of the fluctuating IVFM signal at two closely spaced locations.
Re	Reynolds number based on liquid flux (j_l) and liquid kinematic viscosity.
S	Reduced kinematic perturbation propagation speed.
$S_{\tilde{V}_1\tilde{V}_1}(\tau)$	Spectral density of IVFM output noise.
$S_{\tilde{V}_1\tilde{V}_2}(\tau)$	Cross-spectral density of the IVFM output noise of two closely spaced IVFM's.
STNR	Signal to Noise Ratio of IVFM output.
t	time.
T(N)	Residence time of small amplitude kinematic wave of number N between the two IVFM's.
v	velocity.
v_{Xcorr}	velocity derived from the cross-correlation measurement.
V	Voltage output of IVFM.
V_0	Velocity of particle or bubble relative to liquid at zero volume fraction.

V_s	Measured shock speed.
$\tilde{\mathbf{V}}_1$	Fourier transform of $\tilde{V}_1$.
W_i	Weight of paticle of species i.
y	Vertical spatial dimension.
α	Volume fraction of air.
δ	Kronecker delta.
ΔH_{H_2O}	Head of water corresponding to measured pressure difference.
Δp	Measured pressure difference between the two pressure tappings.
$\Delta p_{1\phi}$	Friction pressure drop in pure liquid pure liquid flow.
$\Delta p_{2\phi}$	Friction pressure drop in a two-component flow between the two pressure tappings.
γ	Ratio of density differences.
$\gamma(N)$	Coherence of the IVFM fluctuating components of wave number N at two locations.
$\epsilon\{q\}$	error in generic measured quantity q.
ε_f	error factor in friction factor measurement.
$\varsigma(N)$	Attenuation of small amplitude kinematic wave of number N between the two IVFM's.
η	Density of Poisson process (the number of bubbles per unit time).
κ	Dimensionless time constant of kinematic perturbations.
μ	Liquid dynamic viscosity.
ν	Volume fraction of solids.
ξ	Decay time constant of IVFM filter function derived from the auto-correlation function of IVFM noise.
ρ	Material density.

τ	Dummy integration time variable.
τ_{max}	Time of location cross-correlation peak.
Υ	Volume of bubble or particle.
$\phi(N)$	Cross-spectral density phase of wave number N.
Φ_m	Two-phase friction multiplier.
ω	Reduced frequency of kinematic perturbations.

Subscripts:

air	Air.
c	Continuous medium.
d	Disperse medium.
g	gas.
i	Component i.
j	Component j.
l	Liquid.
p	Particle.
water	Water.
0	Unperturbed state.
1	Condition upstream of shock.
2	Condition downstream of shock.

Superscripts:

~	Fluctuating quantity.
-	Time averaged quantity.
*	quantity of perturbation order.
*	Complex conjugate.
'	Unsteady component.

Chapter 1. INTRODUCTION.

1.1 General Background.

Two-component flows have been of concern to the engineer for a long time in a number of technologies. Of historical interest in early developments in the field is Darcy's work (1856) on the flow of a fluid through porous media. His results are used to this day by civil engineers to evaluate the flow of water in soils. Of no less significance is Albert Einstein's (1906) first estimate of the viscosity of a dilute two component medium.

Today's advances are predominantly driven by emerging technological needs in the fields of mechanical, petroleum, mining, chemical, nuclear engineering and soil mechanics. Improvements in instrumentation have allowed objective studies and have been closely linked to improvements in understanding the mechanics of multi-component flows.

The advent of synthetic fuels such as coal slurries have called for flow management devices (pumps, let-down valves, etc.) with better resistance to the adverse environment imposed by the fluid . This need has encouraged studies into the factors reponsible for the destructive properties of these flows (Roco (1983), Coughlin & Brennan (1980)).

Accidents in nuclear power plants have focused concern for the safety of this type of power station. For example, the event of forcing vapor into a pool of water subsequent to a loss of coolant accident can lead to a thermohydraulic instability (chugging) which can impose potentially destructive dynamic loads on the structure (Glass & Kadlec (1976)).

Chemical engineers have been mostly concerned with low Reynolds number flows encountered in fluidized beds and sedimentation tanks. Because of the large area of contact between the elements in multi-component flows and good mixing in the host fluid, fluidized beds have found numerous industrial

applications , for example, in catalytic reactions, mixing and coating processes and the combustion of low grade coal. In most applications, efficient operation of fluidized beds is only achieved with a homogeneously distributed flow. However, this ideal is not always attainable, particularly in gas fluidized beds where, despite homogeneous initial fluidization, voidage irregularities known as "bubbles" have been shown to develop upon further increase of the gas flow rate. Further details of the behavior of fluidized beds are given by Zenz (1971) and Richardson (1971).

Separating the components of a suspension, for example, a precipitate or the elements of a colloid, has received much attention in the chemical industries; a recurring objective has been to speed up the process. The topic of one-dimensional sedimentation in a mono-disperse medium under the action of gravity is well reviewed by Barnea & Mizrahi (1973). Faster techniques have recently been suggested. Acrivos & Herbolzheimer (1979) were able to enhance sedimentation by placing inclined walls in settling vessels. Fessas & Weiland (1981) showed that introducing buoyant particles to render the homogeneous dipersion unstable can greatly increase the settling rates of the suspension. One suggested way of implementing this finding is by introducing gas bubbles at the bottom of the sedimentation tank.

Subsequent to the discovery of rich manganese nodule deposits on the bottom of the oceans much work was directed into bringing the minerals to the surface, thus opening the new field of deep ocean mining. The air-lift pump has received much attention as a method of transporting the ore up (Grote & Burns (1980)), to the surface. The air-lift pump has the advantage over regular pumping techniques of having no moving parts. It bases its operation on the entrainment of the solids into a buoyant air-water upward flow in a pipe. The resulting flows are poorly understood and the technique is far from being well

implemented for production. In both two- and three-phase flows, the nodules have a tendency to plug up the pipe by forming a self supporting bridge or arch across the pipe bore thus preventing further transport. Despite the engineering problems in deep ocean mining tasks, the lack of progress has been primarily caused by political obstacles concerning the rights of mining international ocean floors.

With decreasing world oil reserves, less accessible deposits have become econonomically profitable to exploit. The necessity of drilling deeper, often into reservoirs of lesser yield than previously exploited, has led to developments in enhanced oil recovery techniques. Topics in three component flows consisting of crude oil, natural gas and rock chips have received much attention in the oil industry both in reservoir modelling and in oil well flow studies. Unfortunately, much of this work is proprietary and therefore unavailable to the general scientific public. Also, it is clear that the recent slump in the oil industry has diluted the research efforts in this field.

The primary aim of this thesis is to investigate a) friction pressure drops in two-component flows and b) the flow structure which was found to have a marked effect on the flow pressure drop. We focus on vertical flows, a subject that has received little attention in the past. Most of the work on this topic has concentrated on horizontal flows, which are inherently different due to the perpendicular orientation of the gravitational body force with respect to the flow. The lack of predictability of flow regime changes in two- and three-component flows that in turn introduces uncertainty into the friction pressure drop motivated an analytical and experimental study on the stability of homogeneous mono-disperse and bi-disperse media. The secondary purpose of this thesis is to improve the existing Impedance Volume Fraction Meter which was developed by Bernier (1981). This device serves the purpose of monitoring the concentra-

tion of the disperse medium by measuring the bulk electrical impedance of the flowing material. The volume fraction signal typically displays "noise" which is caused by the discrete nature of muli-component flows. Instead of eliminating this "noise" by filtration or other means, we explore its information content, with the aim of extracting flow quantities from its easily measured statistical properties.

1.2 Thesis outline.

An experimental facility was built and instrumented for the study of vertical one-dimensional, two- and three-component flows. The facility is able to accommodate a wide range of different upward and downward flows of air-water, solid-water and air-solid-water mixtures in a 4 inch (.1016 m) pipe. The solids used in this study were polyester particles of cylindrical shape (plastic stock used for injection molding), and the air bubbles were introduced through small perforations in brass tubes. The flow loop, its particle flow control equipment and the instrumentation are described in detail in Chapter 2.

The problem of friction pressure drop in two-phase flows has been studied by numerous investigators. Most of this work has concentrated on horizontal flows , which do not have the ambiguity concerning the unknown hydrostatic head contribution to the pressure gradient (Armand (1946), Lockhart & Martinelli (1949)). Aoki & Inoue (1965) and more recently Nakoryakov et al. (1981) cast some doubt on the previously accepted models by demonstrating marked deviations from those correlations under certain flow conditions. The Three Component Flow Facility designed and built for this work was used to study friction pressure drops in vertical two-component flows of both air bubbles in water and polyester particle-water mixtures. Friction factors of up to two orders in magnitude higher than those at zero volume fraction were observed for both bubbly and slurry flows. This deviation is shown to decrease with increasing

liquid Reynolds number. Bubbly and slurry flow friction factors were comparably large in magnitude and displayed the same decreasing trend as a function of Reynolds number. The two-phase friction multiplier for bubbly flow was shown to attain values up to one order in magnitude higher than the prediction given by Lockhart & Martinelli, whose correlation is better for high air quality agitated flows. Nakoryakov et al. (1981) measured higher bubble concentrations in the vicinity of the pipe wall in bubbly flows, which supports the speculation that the increased wall shear stress is due to enhanced mixing close to the wall. Furthermore, the friction pressure drop in air-liquid flows exhibits non-monotonic behavior as a function of the liquid flow rate. This is observed to take place in conjunction with an onset of unsteadiness in the flow. The change in flow structure is believed to be responsible for the pressure drop anomaly, and for this reason, the stability of the homogeneous two-component dispersion is studied in later chapters.

The lack of data on multi-component flow kinematics is not due to a lack of interest in the topic, but rather to limited availability of instruments with adequate dynamic response. Reviews of two-phase flow instrumentation (Hewitt (1978, 1972), Jones & Delhaye (1976)) point out that only a few instruments can be used for transient measurement of the volume fraction. In the past, the only reliable and available methods of measuring volume fraction in two-component media with good dynamic response were the X-ray attenuation technique (Zuber et al (1967), Schrock (1963)) and the later developed γ-ray attenuation methods (Taylor et al. (1979)). The accompanying equipment with this type of device is typically costly and cumbersome and safety precautions must be exercised. Local point measurement techniques using hot film anemometry (Toral (1981), Delhaye & Galaup (1977), Jones O.C. (1966)), miniature resistivity probes (Burgess & Calderbank (1975)), or more recently optical probes (Abuaf et al. (1978), van

der Lans (1985)) have proved to be successful in gas-liquid flows, but are not suited to the abrasive environment of solid-liquid flows. The advent of ultrasonic detectors shows promise in measuring volume fraction of gas-liquid mixtures as suggested by Arave and Fickas (1979). Volume fraction meters that base the measurement on the electrical impedance of the medium have been shown to be capable of unsteady dynamic measurement (Garrard & Ledwidge (1971), Jallouk et al. (1979)).

Bernier (1981) developed an Impedance Volume Fraction Meter (IVFM) designed to monitor the volume fraction of non-conducting material in water (bubbles or particles). The instrument is entirely non-intrusive and has the advantage of being rugged and easy to use in comparison with ray attenuation techniques. This device was modified for the present study by the installation of temperature compensation and by shielding the active electrodes. The steady state and dynamic calibrations of this transducer are documented in Chapter 4. The IVFM is shown to have good spatial and temporal resolution, and proved to be a useful tool for monitoring the passage of individual particles or bubbles as well as infinitesimal and finite kinematic waves.

Two phase flows are susceptible to numerous hydrodynamic instabilities which are reviewed by Bouré et al. (1971). These instabilities are manifested by waves which for our purposes can be grouped into acoustic or pressure waves and kinematic waves (also called concentration or continuity waves). Both systems of waves are generally coupled but they do have distinct characteristics. The acoustic waves typically assume high frequencies and high speeds whereas the kinematic waves which are driven by slip between components are characterized by low speeds and frequencies. The kinematic instability is responsible for flow regime changes where deviation from the homogeneous suspension occurs, such as with bubbling in gas fluidized beds. Further details on fluidized bed

instabilities are given by Zenz (1971) and Richardson (1971).

Kinematic waves were first uncovered by Kynch (1952) in his work on sedimentation and were used by Lighthill & Whitham (1955) to analyze flood waves and traffic flow on long highways. Later Wallis (1962) and Zuber (1964) used kinematic wave theory to describe the propagation speed of volume fraction which they showed to be quite different from the mean bubble speed. More recent developments in modelling two-component flows have been made by Anderson & Jackson (1967,1968) and Homsy et al. (1980).

In Chapter 4, the theory of one-dimensional kinematic wave propagation and attenuation is studied using three approaches. The Drift Flux Model is first described. This quasi-steady model based on the continuity of both components yields the speed of infinitesimal waves, and predicts these to be neutrally stable. Then the effect of inertia is introduced and shown to make perturbations of all wave numbers unstable, while giving wave speeds that are in close agreement with the Drift Flux Model. Finally, the effect of size distribution is studied. Recent work by Batchelor (1986) is extended to predict the kinematic wave speed and attenuation in bi-disperse flows. This model is applied to a two-component medium which is narrowly distributed in size. The medium is represented by a dispersion of two distinct size groups of narrowly spaced diameters. The results yield wave speeds similar to the earlier ones. Of interest is the instability which only sets in at high concentrations, higher than the maximum physically attainable values. This result may only be of academic interest, however it does indicate that the size distribution has a destabilizing effect at high volume fraction. The bi-disperse model is also used to determine the theoretical stability boundary for the solid-liquid-gas medium which was studied experimentally. In these studies, the loss of stability of the multi-component system is manifested by the onset of large vortical structure in the flow. The results are compared

with experimental observations in Chapter 8.

An experimental study of kinematic waves was carried out by measuring the propagation and attenuation of the coherent component in the naturally occurring random fluctuations in the volume fraction. This work is described in Chapter 6. The volume fraction was measured at two locations and the coherent signal common to both signals was used to extract the desired information. Using a cross-correlation technique, small amplitude kinematic speeds were determined. These are found to agree well with the predictions in Chapter 5. The linear phase of the cross power spectrum proved the kinematic waves to be non-dispersive. The coherence function in the frequency domain was used to evaluate the attenuation of kinematic waves as a function of perturbation wave number. These results constitute an experimentally determined dispersion relation for two-component flows, of the bubbly and particulate kinds. In bubbly flows of high volume fraction (40%) the IVFM fluctuations are found to contain much more common coherent signal just before the onset of instability (churn-turbulence) than at any other bubbly flow volume fraction.

In Chapter 7, the propagation speed of finite amplitude stable kinematic shocks is studied in vertical bubbly and particulate flows. Experimental measurements of bubbly shock speeds are compared to the semi-empirical predictions based the Drift Flux Model. The good agreement led us to use particle shock speed measurements to extract the drift flux curve for solid-liquid mixtures at low flow rates. This function is used in Chapter 5 to determine the infinitesimal kinematic wave speed based on the Drift Flux Model.

Data for solidification shocks is also presented. The propagation of this type of shock has been studied previously in conjunction with batch sedimentation for zero net flow processes (Wallis (1962)). The problem has also attracted interest in the field of soil mechanics in studies on of water-saturated sands

(Scott (1986), Gibson (1958), Terzaghi (1943)). Violent shaking can cause such deposits to liquefy such that individual sand grains become suspended in the host liquid, resulting in a free flowing medium. Following liquefaction, solidification of the material occurs. In the present experiments on high particle concentration flows, solidification shocks were captured and all flow quantities were monitored. Above such shocks, the medium is fluidized; below it the solids are packed. The wave is called a solidification shock because the particles are supported by the liquid above the shock whereas below the shock, the weight and forces on the particles are supported by the particle matrix itself. These shocks are found to be dramatically faster than fluidized flow shocks and therefore potentially more destructive.

The regimes of two- and three-component flows are studied in Chapter 8 and novel measurement techniques are suggested for these flows based on the statistical properties of the fluctuations of the IVFM output. In disperse two-component flows, the coherent time scale, ξ, in this noise is found to be approximately proportional to the particle or bubble speed. In churn turbulent flows, ξ is found to be well correlated to the air volume flux. The Signal To Noise Ratio (STNR) is shown to be uniquely related to the volume fraction in disperse two-component flows. In three-component flows, the STNR and ξ remain good indicators of total volume fraction and the characteristic speed of the flow structure respectively.

Fessas & Weiland (1981) demonstrated the existence of two flow regimes in bi-disperse sedimenting flows of two solid species. In the present work, three-component flows of intermediate Reynolds numbers (based on the particle diameter and speed) are found to undergo a regime change from a disperse nature to a very agitated one. In the less violent regime, the hindering in the rise velocity of the bubbles is found to be high as manifested by the low mean air

velocities measured. After the flow regime change, the mean air velocity relative to the liquid-solid flux is found to rise dramatically and the flow exhibits a large vortical structure. The relative velocity measurements show marked similarities with the results of Fessas & Weiland; both studies observed a fall in hindered settling velocities with increased volume fraction followed by an increase after the flow regime change.

Chapter 2. THREE COMPONENT FLOW FACILITY.

For the purpose of flow studies and instrumentation development a Three Component Flow Facility (TCFF) was designed and constructed. This facility (Figures (2.1)) is capable of generating a wide range of different liquid-gas, liquid-solids or liquid-solids-gas flows in a test section (presently a vertical 2 m length of .1016 m I.D. lucite tube). It operates as follows. Liquid (water) is circulated through the system by means of a 3 hp centrifugal pump producing velocities of up to about 2 m/s in the .1016 m I.D. working section. The system of valves shown in Figure (2.1) permits adjustment of the water flow rate to any value up to this maximum in either direction. The water flow rate is measured by means of an electromagnetic flowmeter in the water circuit. A gas (air) injector can be located at either end of the working section, though it is presently installed at the lower end. This air injector consists of 21, 1/8 in. tubes criss-crossing the flow in various directions and staggered over an axial length of about 6 in. Air is ejected through many 1/64 in. holes drilled in the 1/8 in. tubes. This arrangement yields both a very uniform injection of bubbles over the cross-section and a uniform resistance to the water flow through the device so that the two-phase flow which emerges from the injector is as uniform as possible. The mass flow rate of air is measured by means of a calibrated orifice meter with a series of interchangeable orifices.

The most novel aspect of the present facility is its ability to handle solids and to control the solids flow rate independently of the liquid without having to continuously add or remove solids from the system. It operates as follows. The facility is presently configured for the downward flow of solids which have a specific gravity greater than unity. Such solids are initially stored in the upper tank with the control cylinder (Figure (2.2)) in the fully down position. Water can circulate in the system by passing up or down through the control cylinder

which is essentially a continuation of the working section; the solids simply reside in the backwater outside of the control cylinder. Raising the control cylinder causes solids to flow down into the working section at a rate which can be controlled by varying the gap between the control cylinder and the surrounding tank bottom (conical). As is the case in most granular material hopper flows the solids flow remains almost independent of the amount of material in the hopper until the latter is almost exhausted. The experiment then continues until all the solids have collected in the lower tank (they are prevented from travelling further by a fine mesh screen). To recycle the solids the control cylinder is lowered to the closed position and sufficient upward water flow is generated to fluidize the solids in the lower tank (this accounts for the smaller I.D. and longer length of this tank) and to carry them back up to the upper tank where they settle into their original position. A screen at the top of the upper tank prevents the solids from escaping from that tank.

The present configuration of the facility is designed for solids with specific gravities between unity and three. The lower density limit comes from the requirement that the particles should sink, and the upper bound is dictated by the pumps ability to fluidize the packed bed. For the work described in this thesis the facility was loaded with polyester plastic stock which consists of cylindrical beads of about 3 mm diameter and 1.43 specific gravity. Several sizes of glass beads with specific gravity of 2.5 are also available but have not, as yet, been tested. The facility could also be used for coal.

If anything, the facility operated better than anticipated with the plastic beads. The only problems experienced occurred at large air flow rates with countercurrent downward flow of water. As the flooding condition was approached (and this condition varied with the solid flow) there was an expected tendency for excessive water rejection from the system via the water overflow.

2.1 Instrumentation

Two Impedance Volume Fraction Meters (IVFM) were installed in the working section. This non-intrusive instrument was previously developed for the purpose of measuring the void fraction in gas-liquid two component flows. It is based on the measurement of the high frequency electrical impedance of the mixture and consists of two shielded stainless steel electrodes laid flush with the interior surface of the tube (.1016 m I.D.) as seen in Figure (4.1). The axial dimension of the electrodes is small (6.5 mm) in order to resolve short wavelength structures in the flow. Essential characteristics of the electronic processing are the 50 kHz excitation and the double-bridge signal processor. The device has excellent frequency response and axial spatial resolution of a few centimeters. The device will measure either the air void fraction in water-air flow or the solid volume fraction in water-solids flow. In either case, the calibration of the device is obtained by comparison with the hydrostatic pressure gradient when there is zero water flow. In a three component water-air-solids flow it will measure the combined volume fraction of solids and air. Making use of a bulk hydrostatic pressure gradient measurement, we are able to separate the volume fractions of the two disperse components. The IVFM is described in more detail in Chapter 4.

Two Electromagnetic Flowmeters (EF) are installed in the facility. These consist of standard Foxboro commercial hardware with special excitation/signal processing equipment built in the Caltech laboratory. The latter produces a high frequency (328 Hz) magnetic field in order to obtain good dynamic response (as opposed to the standard 60 Hz field, which is inadequate in this respect). The signal is processed through a 68 dB preamplifier and a demodulator. Previous experiments have shown that this device has excellent dynamic response up to a frequency of about 40 Hz in velocity fluctuations; indeed it proved superior

to an Laser Doppler Velocimeter (LDV) system in those earlier experiments insofar as measurement of unsteady volume flow rate of a single component water flow was concerned. In single component water flows the EF has two very useful characteristics. First, its calibration is independent of the electrical conductivity of the fluid. Second, it yields the total volume flow rate independent of the velocity profile provided the latter in axisymmetric. Even this caveat has been shown to be minor in some recent experiments.

One of these meters is used to measure the total flow rate in the TCFF. A previous test program investigated its use in an air-water two component flow (Bernier (1983)). In those tests it was shown that the device has further advantages. It measures the average water velocity (not the water flow rate) and does this irrespective of the distribution of voids over the cross-section, provided again that the distribution is axisymmetric in the mean. This was confirmed over a substantial range of void fractions, water flowrates, slip ratios and flow regimes by Bernier. However, in the present work, it was found that slight non-uniformities in the magnetic field introduce error into the measurements at low flow velocities. Since most flows considered in this study were no larger than .3 m/s, the EF was not used in the multi-component test section, but only in the single phase part of the loop.

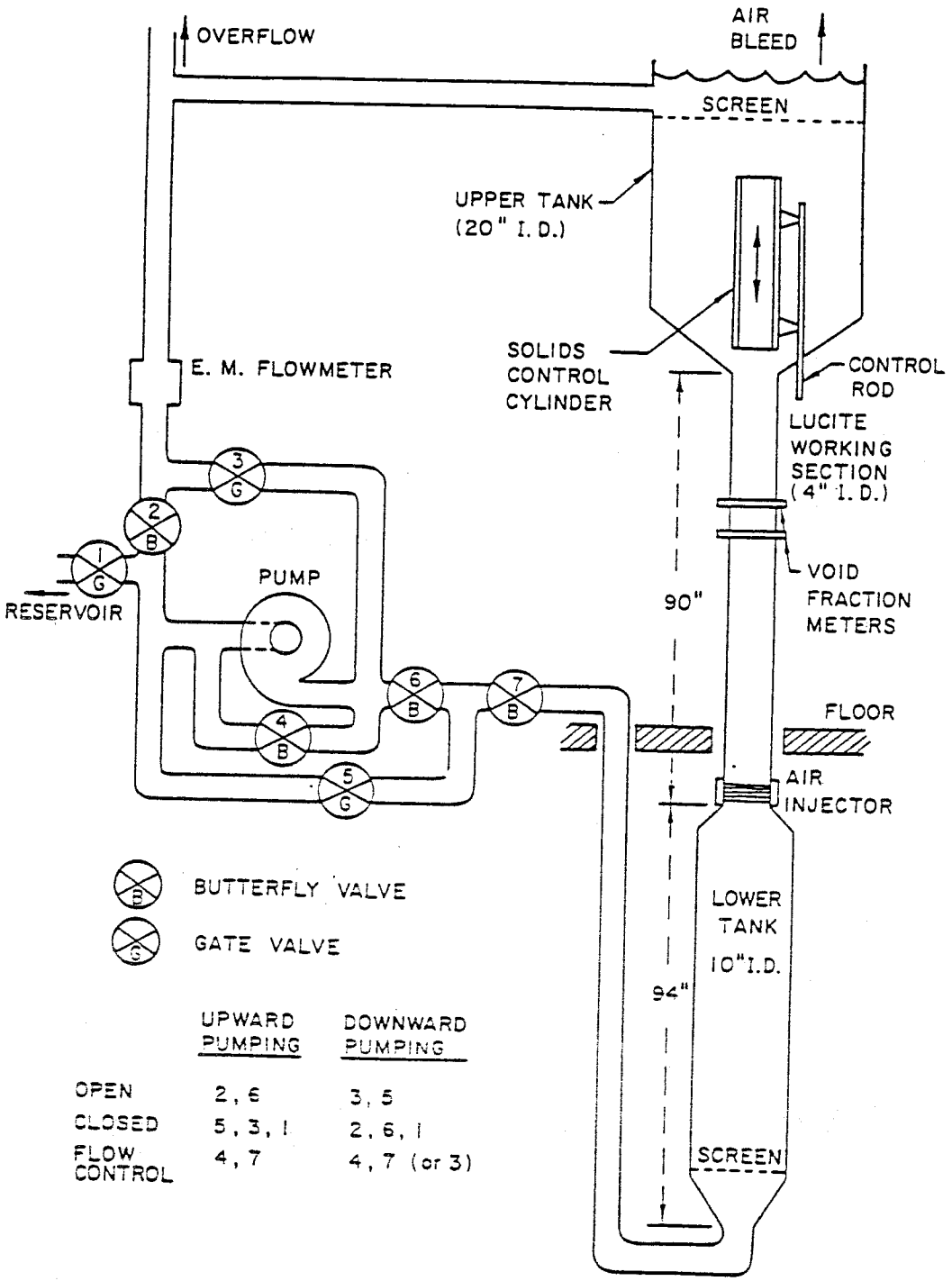

Figure (2.1) Schematic of the Three Component Flow Facility.

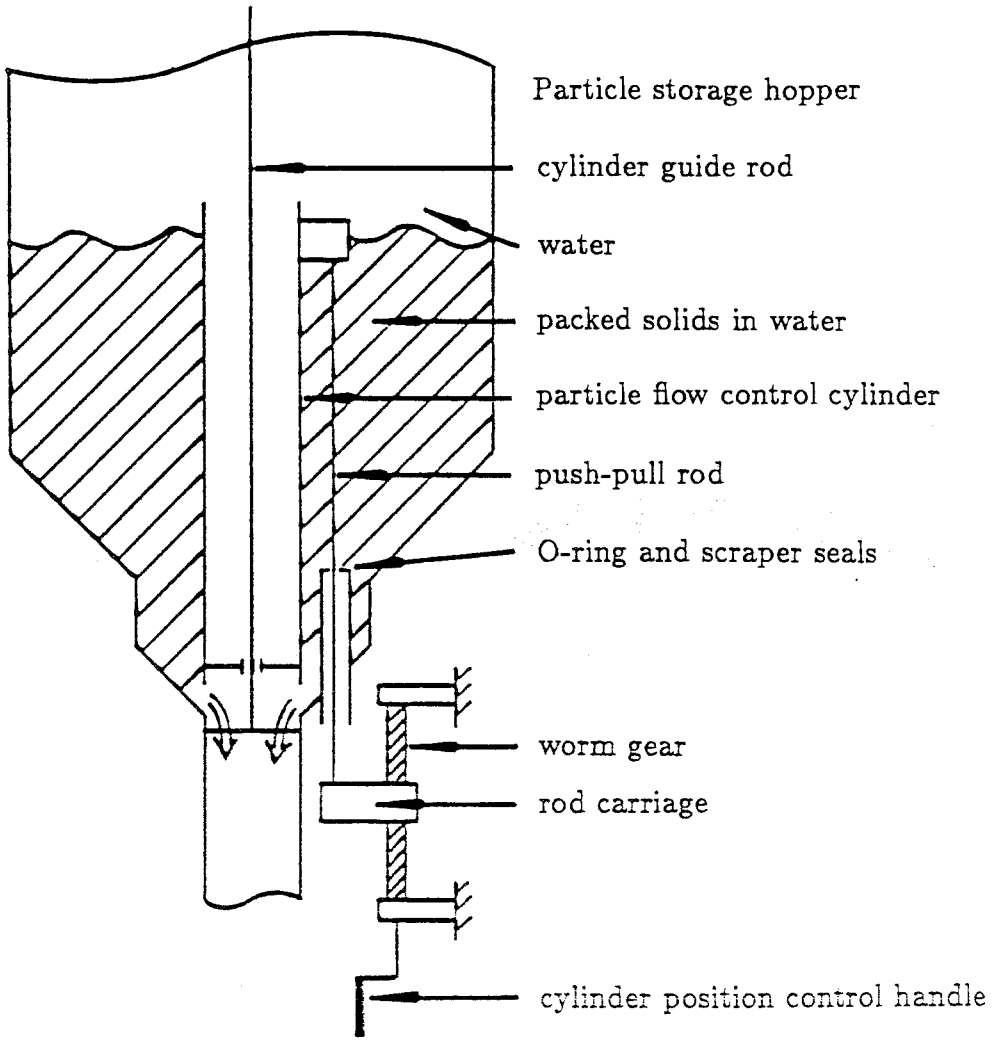

Figure (2.2) Schematic of the Control Cylinder used to regulate the flow rate of solids.

Chapter 3. MEASUREMENT OF FRICTION PRESSURE DROP IN VERTICAL SLURRY AND BUBBLY FLOWS.

The problem of friction pressure drop in two-phase flows has been studied by numerous investigators. Most of this work has concentrated on horizontal flows on which models were based that have been widely used. Of note is Lockhart & Martinelli's (1949) model which has been applied to both vertical and horizontal flows. More recent studies have shed some doubt on these previously accepted results by demonstrating marked departure from these under certain flow conditions (Nakoryakov et al.(1981), Aoki & Inoue (1965)). The Three Component Flow Facility is used to study friction pressure drops in vertical two component flows of both air bubbles in water and polyester particle-water mixtures.

3.1 Experimental facility and procedure.

The Three Component Flow Facility described in Chapter 2 was used to study friction pressure drops in both air-water and polyester particle-water mixtures. The bubbly flows are formed by introducing air through an injector situated inside the vertical 4 inch (.1016 m) pipe, 60 cm below the test section. The bubbles formed have an average diameter of 4 mm ($\pm$.7 mm). The polyester particles are introduced at the top of the test section from the particle hoppper through a particle flow control gate. The particles have an average diameter of 3 mm ($\pm$ .5 mm) and are cylindrical in shape. A three horse power pump controls the water flow rate which is monitored with an electromagnetic flow meter. The static pressure difference between two points 1.694 m apart in the test section is measured with an inverted air on water manometer. The static pressure measurement contains a large hydrostatic component and a smaller contribution from the frictional pressure drop. The volume fraction of the disperse medium is monitored with the Impedance Volume Fraction Meter (IVFM). The accu-

rate knowledge of the volume fraction allows us to extract the friction pressure drop from the measured static pressure gradient by subtracting the hydrostatic contribution.

Experiments with different air and water flow rates were carried out with the air flow held constant and the water flux, j_l (volume flow rate divided by the pipe cross-sectional area), incremented from 0 to 1 m/s. This was done for volume fractions of 0 to 40%. After each adjustment, conditions were allowed to settle for 15 seconds and all monitored quantities were recorded. All air-water flows studied were cocurrent and upward.

The polyester particle slurry flows studied were cocurrent and downward. With a pre-set liquid flow rate the solid fraction was incremented between each run. For each set of conditions, the liquid flow rate, the static pressure gradient in the test section and the solid fraction were monitored. The solid fraction ranged from 0 to 50%. The liquid flux was incremented through a range of 0-.6 m/s. In both types of flow the raw data were stored in random access files on a microcomputer floppy disc for manipulation and presentation.

3.2 Pressure losses in vertical upward air-water flows.

Pressure losses in vertical upward air-water flows were obtained by subtracting the vertical static pressure difference in the flow from the pressure gradient caused by the gravitational body force. The latter was obtained by calculating the bulk density, ρ_b, from the volume fraction, α and the known densities of air, ρ_g, and water, ρ_l.

$$\begin{aligned} \Delta p_{2\phi} &= \Delta p - \rho_b g L, \\ &= \rho_l g L \left(\frac{\rho_l - \rho_g}{\rho_l} \right) (\alpha - \Delta H_{H_2O}/L). \end{aligned} \tag{3.1}$$

where $\Delta p_{2\phi}$ is the two phase frictional pressure drop, and ΔH_{H_2O} is the measured pressure difference as a head of water. We have chosen to represent the

pressure loss data in terms of both a friction factor, $f_{2\phi}$, and a two phase multiplier, Φ_m, defined as

$$f_{2\phi} = \frac{\Delta p_{2\phi}}{2\rho_l j^2} \frac{D}{L}, \tag{3.2}$$

$$\Phi_m = \frac{\Delta p_{2\phi}}{\Delta p_{1\phi}}. \tag{3.3}$$

where $\Delta p_{1\phi}$ is the pressure drop which would occur for the single component flow with the same water flow rate.

3.2.1 Friction factor.

The friction factor is presented as a function of Reynolds number with the volume fraction, α, as a parameter (Figure (3.1)). All the two phase friction factors are significantly larger than the pure liquid ($\alpha = 0$) curve, indicating a trend of increased resistance to flow with large volume fractions. Non-monotonic behavior can be seen within friction factor results which generally decrease with Re. This is best shown by the $5\% < \alpha < 10\%$ curve which goes through a minimum at Re=2×10^4 and a maximum at Re=4×10^4. This phenomenon is somewhat similar in nature to the transition from laminar to turbulent flow observed in pure liquid pipe flow. It is generally accepted that bulk two phase viscosity is increased with volume fraction (Barnea & Mizrahi (1973)); therefore, for the higher volume fraction curves, a Reynolds number based on a bulk kinematic viscosity would be much smaller than the one chosen here for simplicity (based on the kinematic viscosity of water). Using such a Reynolds number would then shift constant α curves progressively to the left with increasing α. Ultimately, the bulk Reynolds number will be small enough to be in the transition zone where non-monotonic $f_{2\phi}/Re$ behavior is seen in single component flows. These results suggest the existence of bulk laminar and bulk turbulent flows. At higher Reynolds numbers all the constant α curves come together indicating a decreasing dependence of f on α at larger flow rates.

3.2.2 Two phase friction multiplier.

The two phase friction multiplier is the mixture pressure loss normalized with the pure liquid pressure loss at the same liquid flow rate. The pure liquid friction factor curve used (shown in Figures (3.1) and (3.3)) was a least squares regression fit of the present measurements to Prandtl's Formula for fully turbulent pipe flow:

$$1/\sqrt{f_{1\phi}} = A\,log\left(Re\sqrt{f_{1\phi}}\right) + B, \tag{3.4}$$

where A and B are the parameters of the fit. A complete derivation of this equation is found in White (1974). The curve of best fit corresponds to the friction factor curve of dimensionless pipe relative roughness of .0008 on the Moody Diagram. This curve which is shown in Figures (3.1) and (3.3) (labelled $\alpha = 0$) is used to determine the equivalent pure liquid friction pressure drop, $\Delta p_{1\phi}$ required to calculate the friction multiplier. The air-water flow friction multiplier results are shown in Figure (3.2). These are for the bubbly flow regime only. The churn-turbulent results exhibited great scatter and are omitted for clarity. In Figure (3.2) the friction multiplier takes on dramatically high values at low flow rates. There is a rise and fall off with increasing air volume quality in the form of a "hump" which decreases in size with increasing liquid flow rate. For a Reynolds number of 30,000, the friction multiplier has a maximum of 15 whereas for Re=75,000 the maximum is 5. This same phenomenon was documented by Aoki and Inoue (1965) and by Nakoryakov et al. (1981) who found friction multiplier maxima of 20 (Re=6,000) and 11 (Re=19,000) respectively. The values of Reynolds number over which Aoki observed this phenomenon ($6 \times 10^3 - 40 \times 10^3$) are much below those of Nakoryakov's ($19 \times 10^3 - 177 \times 10^3$) or the present experiments. The discrepancy between the results of the three investigations and the geometrical flow differences suggest that in addition to the variation with the Reynolds number, the different bubble to pipe diameter

ratios (Aoki .1, Nakoryakov .03, present experiments .035) in the investigations has a strong effect on the friction multiplier. As can be expected, the results for diameter ratios of .03 and .035 are closest to one another.

Air-water friction pressure drop measurements reveal large deviations from previously accepted correlations. The discrepancy is particularly evident at low liquid flow rates where the two-phase friction multiplier assumes as high a value as 15 in comparison with a maximum of 1.1 according to Lockhart and Martinelli's correlations. The discrepancy decreases at higher flow rates at which the dependence of the friction factor on volume fraction on volume fraction weakens. The ratio of bubble to pipe diameter is noted to have a marked effect on the friction pressure drop.

3.3 Pressure losses in vertical slurry flows.

3.3.1 Friction factor.

Frictional pressure drops in polyester particle slurry flows were obtained by subtracting the vertical static pressure difference from the hydrostatic pressure difference as in the bubbly flows. The hydrostatic component is derived from the bulk density obtained from the monitored particle volume fraction. Then the friction component of the pressure difference, $\Delta p_{2\phi}$, is given by

$$\begin{aligned} \Delta p_{2\phi} &= -\Delta p + \rho_b g L, \\ &= \rho_l g L \left(\nu \frac{\rho_p - \rho_l}{\rho_l} - \Delta H_{H_2O}/L \right), \end{aligned} \tag{3.5}$$

where ν is the volume fraction of solids. The friction factor is defined as

$$f_{2\phi} = \frac{\Delta p_{2\phi}}{2\rho_l j^2} \frac{D}{L}. \tag{3.6}$$

The slurry flow friction factor in Figure (3.3) reaches values of up to 15 times the zero volume fraction equivalent at the lower Reynolds numbers considered. This represents a static pressure loss gradient 15 times that experienced with the

pure liquid (water) alone. The deviation from the zero volume fraction curve decreases with increasing Reynolds number and the constant volume fraction curves asymptotically tend to the zero volume fraction curve as the Reynolds number increases. Unlike the bubbly flow friction factor results, these trends are monotonic.

3.4 Error analysis.

The error analysis proved to be a vital tool in the presentation of our results through the elimination of data with intolerable error content. Such an analysis is found to be imperative when the required results are derived by subtracting the large hydrostatic component from the measured pressure difference. Based on the estimated error in each measurement we obtain an expression for the overall error in the frictional pressure drop.

The maximum errors in the volume fraction, the static pressure head and the water Reynolds number were estimated in proportion to the measurement amplitude; these estimates are shown below:

$$\frac{\epsilon\{\alpha\}}{\alpha} = \frac{\epsilon\{\Delta H_{H_2O}\}}{\Delta H_{H_2O}} = \frac{\epsilon\{Re\}}{Re} = .05, \tag{3.7}$$

where the notation $\epsilon\{q\}$ denotes the error in the quantity q. We have represented the volume fraction using α, which is the air volume fraction. In this section, we use α to interchangeably denote either the air or the solids volume fraction.

3.4.1 Error content in the friction multiplier.

The error in the friction multiplier, Φ_m can be written using its definition (3.3):

$$\frac{\epsilon\{\Phi_m\}}{\Phi_m} = \frac{\epsilon\{\Delta p_{2\phi}\}}{\Delta p_{2\phi}} + \frac{\epsilon\{\Delta p_{1\phi}\}}{\Delta p_{1\phi}}. \tag{3.8}$$

This can now be written in terms of the actual measurements using (3.1):

$$\frac{\epsilon\{\Phi_m\}}{\Phi_m} = \left\{ \frac{\epsilon\{\alpha\} + \epsilon\{\Delta H_{H_2O}\}/L}{\alpha - \Delta H_{H_2O}/L} \right\} + \frac{\epsilon\{f_{1\phi}\}}{f_{1\phi}} + 2\frac{\epsilon\{Re\}}{Re}. \tag{3.9}$$

In single phase flows, a change in Reynolds number results in a comparatively large change in the friction factor. The friction factor error term is therefore negligible compared to the Reynolds number one. The error in the two phase multiplier is rewritten as

$$\epsilon\{\Phi_m\} = \Phi_m \left\{ \left\{ \frac{\epsilon\{\alpha\} + \epsilon\{\Delta H_{H_2O}\}/L}{\alpha - \Delta H_{H_2O}/L} \right\} + +2\frac{\epsilon\{Re\}}{Re} \right\}. \tag{3.10}$$

Equation (3.10) is used to determine the error in the air-liquid flow two-phase multiplier, Φ_m, and all measurements that did not satisfy

$$\epsilon\{\Phi_m\} < 5 \tag{3.11}$$

were disgarded. The results containing smaller errors than the above tolerance are shown in Figure (3.2).

3.4.2 Error content in the friction factor.

The error in the friction factor can be written using (3.1) and (3.2) in the case of air-liquid flows and (3.5) and (3.6) for solid-liquid flows. The error analysis is identical for both cases, so we only present air-liquid case. The error in the friction factor is

$$\frac{\epsilon\{f_{2\phi}\}}{f_{2\phi}} = \left\{ \frac{\epsilon\{\alpha\} + \epsilon\{\Delta H_{H_2O}\}/L}{\alpha - \Delta H_{H_2O}/L} \right\} + 2\frac{\epsilon\{Re\}}{Re}. \tag{3.11}$$

The friction multiplier is presented on a logarithmic scale. We therefore define an error factor, ε_f, which behaves as a error of fixed size on a logarithmic scale:

$$\varepsilon_f = \left\{ \frac{1 + \epsilon\{f_{2\phi}\}/f_{2\phi}}{1 - \epsilon\{f_{2\phi}\}/f_{2\phi}} \right\}. \tag{3.12}$$

Equations (3.11) and (3.12) are used to evaluate the only points satisfying

$$\varepsilon_f < 5. \tag{3.13}$$

are shown in Figures (3.1) and (3.3). All other points are disgarded.

3.5 Conclusions

The present study has revealed some very large discrepancies between the measured frictional pressure gradients and existing empirical correlations.

The bubbly flow pressure loss measurements display a marked departure from commonly used models (Lockhart-Martinelli (1949), Armand (1950)). At small liquid and air flow rates, the measured pressure drops were up to an order of magnitude higher than predicted by the aforementioned authors. This phenomenon is as yet poorly understood and has only been documented in some recognizable form in two other experimental studies (Aoki and Inouie (1965), Nakoryakov et al. (1981)) which were carried out for different pipe diameters. High friction multiplier values were shown to correspond to flows with volume fraction peaks in the vicinity of the wall by Nakoryakov at al. This supports the theory of increased wall shear stresses due to enhanced mixing close to the wall caused by the presence of the disperse medium. A mixing length theory based on this and empirically obtained constants has been developed by N. Clarke (1983), who predicts a sharp rise in the friction multiplier with respect to the air volume quality.

The bubbly and slurry flow friction factors were close to one another in magnitude and in both cases were found to be much more sensitive to the volume

fraction of the disperse medium at low liquid Reynolds numbers than at high Re. At high Reynolds numbers ($\sim 7 \times 10^4$) unsteadiness can be observed in the flow on a larger scale than the bubble or particle diameter. This visual evidence of a "bulk turbulence" appears after the point at which the friction factor displays non-monotonic behavior in Figure (3.1). Further work on the flow structure is described in Chapter 5,6 and 8.

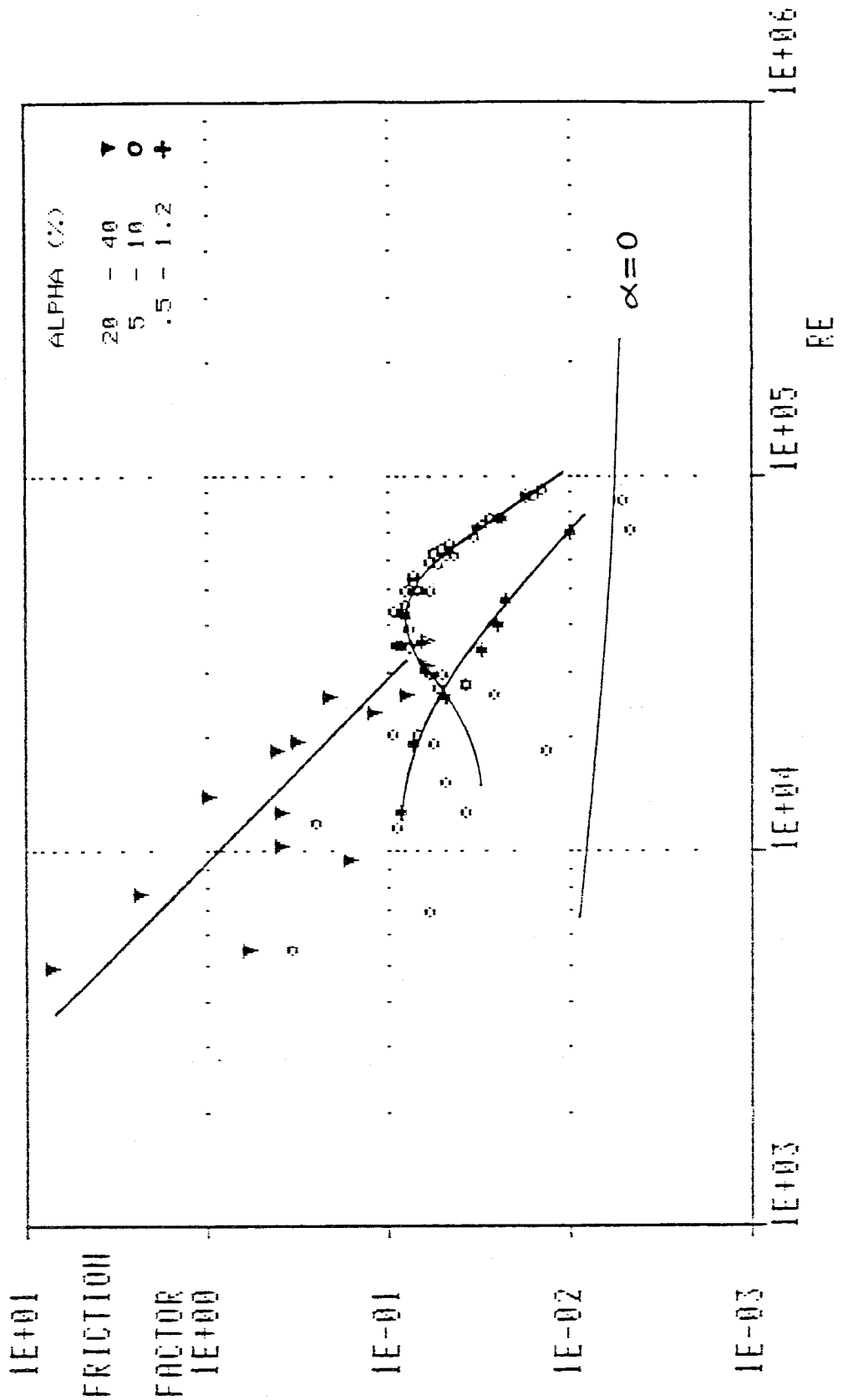

Figure (3.1) Air-water flow friction factor (based on the total flux and the liquid density) versus the flow Reynolds number (based on the total flux and the liquid viscosity).

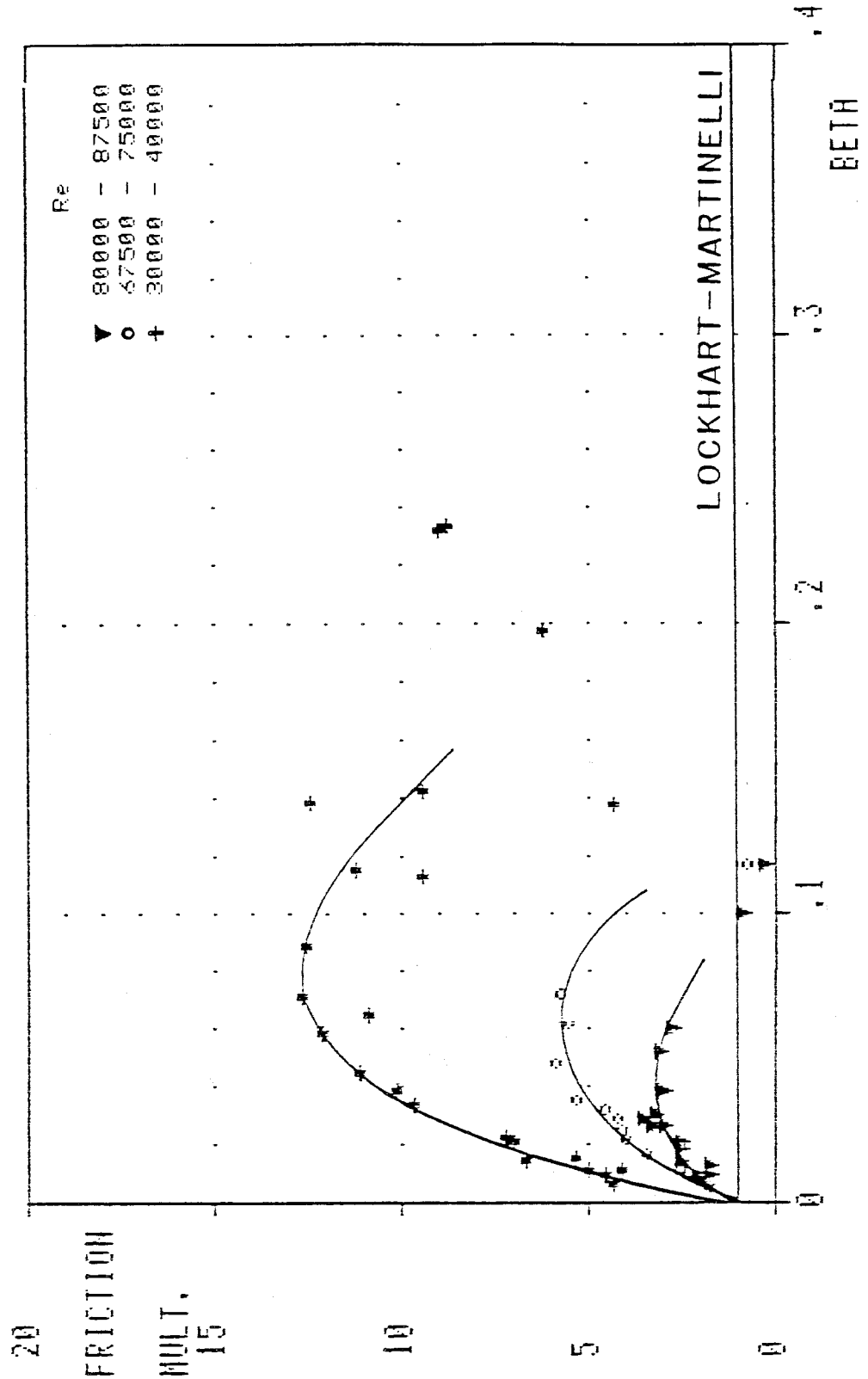

Figure (3.2) Air-water two-phase friction multiplier Φ_m presented versus the air volumetric quality, showing the large deviation of the present measurements from Lockhart & Martinelli's correlation.

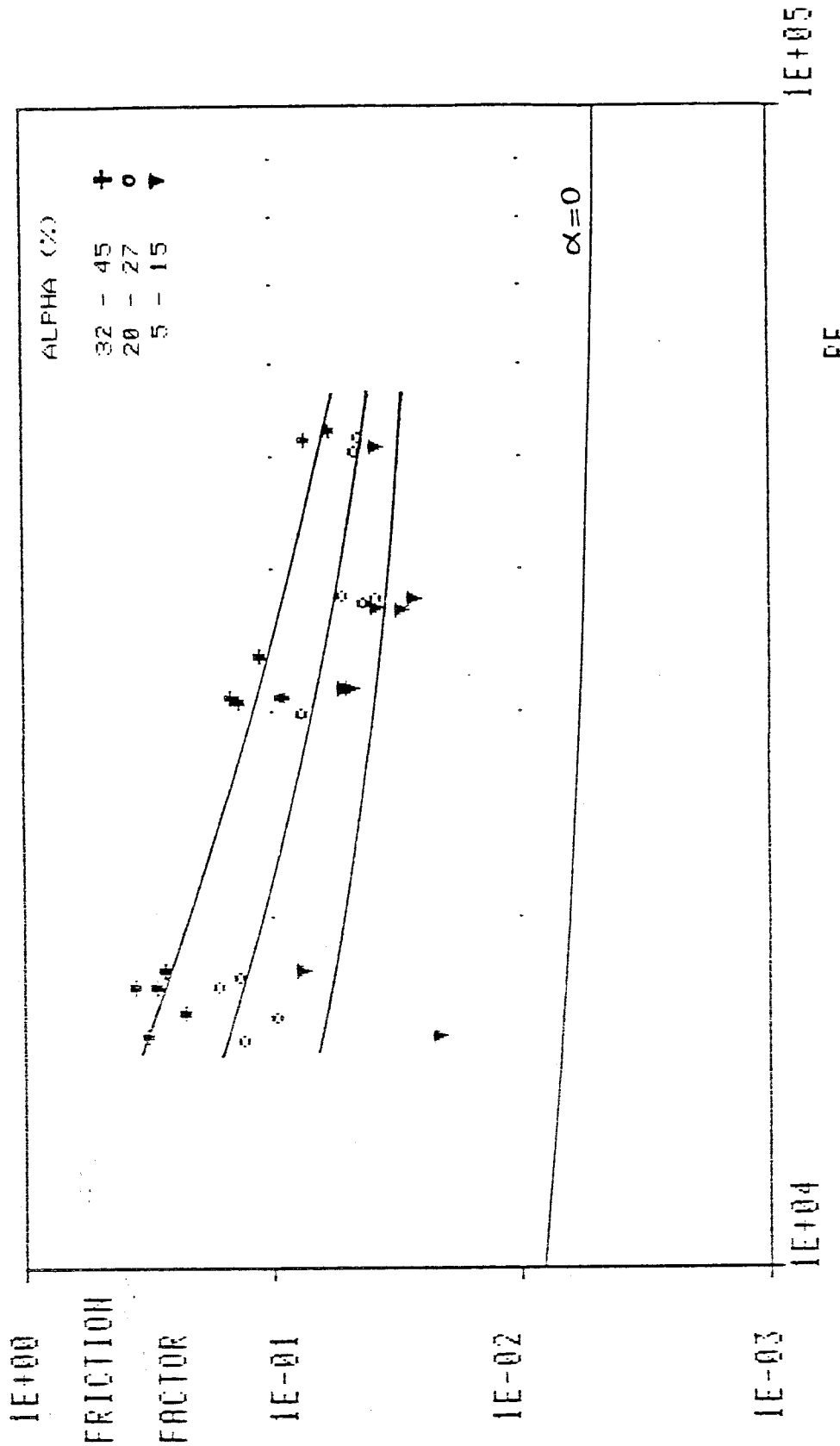

Figure (3.3) Solid-liquid flow friction factor (based on the total flux and the liquid density) versus the flow Reynolds number (based on the total flux and the liquid viscosity).

Chapter 4. IMPEDANCE VOLUME FRACTION METER.

4.1 Introduction.

A variety of methods have been used by investigators for unsteady measurement of volume fraction in two phase media. In liquid-gas mixtures, intrusive hot wire anemometers (Toral (1981), Delhaye & Galaup (1977), Jones O.C. (1966)) and optical probes yield a point measurement (van der Lans (1985), Abuaf et al. (1978)) representative of the medium in the vicinity of the probe (such devices could not withstand the mechanical wear of particulate flows). With such transducers, the signal needs to be averaged over time to obtain useful volume fraction information thereby decreasing the dynamic resolution of the device. On the other hand X-ray (Zuber et al. (1967)) and Gamma-ray attenuation (Taylor (1979)) techniques inherently carry out an instantaneous line average of the volume fraction along the beam, with the added benefit of being nonintrusive. Capacitance and resistance measurements can be used to yield a volume average of the concentration of the dispersed medium. The size and shape of the averaging volume is determined by the geometry of the electrodes.

An impedance measuring technique with flush mounted electrodes was chosen for our purposes because of its nonintrusive nature and its ease of use. By comparison, ray attenuation methods are more cumbersome and often lack dynamic capability. The Impedance Volume Fraction Meter (IVFM) used in our study was developed by Bernier (1981). The original excitation and signal processing equipment are well documented in more detail in his thesis. This chapter will be confined to a discussion of the modifications made for temperature compensation and the new shielded electrode configuration implemented to decrease the axial extent of the influence volume of the measurement. The instrument is calibrated against a hydrostatic measurement of volume fraction in homogeneously distributed two phase media. This was done for both liquid-solid and

liquid-bubble mixtures. The device output is shown to vary linearly with the volume fraction with a slope that is found to be independent of the material of the disperse medium, solid or gas.

Due to the discrete nature of two and three component flows, the measurement of steady state volume fraction exhibits oscillations about a mean value. Statistical properties of the fluctuating flow quantities have been shown to contain valuable information on the mean properties of the flow. The fluctuating component of the pressure drop in two phase flow through an orifice has previously been used to derive the flow rates of the individual constituents by Ishagai et al. (1965). Jones and Zuber (1975) used the probability density function of X-ray attenuation volume fraction signals as a flow pattern discriminator for vertical bubbly, slug and annular flows. In this study, statistical analysis of the fluctuating component of the output signal of the present device is shown to yield valuable information on the volume fraction, mean velocity and flow rate of the disperse medium in two- and three-component flows.

4.2 Principle of operation of the Impedance Volume Fraction Meter.

This class of volume fraction measuring devices operates on the principle that the bulk electrical impedance of a two-component mixture differs from that of its constituents as long as the electrical impedances of the individual constituents are not equal. In general there are components of both resistance and capacitance in the impedance, and the choice of driving frequency determines the dominance of one or the other. In our case, water is the continuous medium and non-conducting air bubbles and polyester pellets are the dispersed medium. Polarization caused by ionization of the water in the vicinity of the electrodes has been shown to introduce a parasitic impedance (Olsen (1967)). This effect vanishes at high frequencies. For our experiments, a frequency of 40 KHz was chosen. This eliminates the parasitic impedance while keeping the

fluid cell impedance predominantly resistive.

4.3 Electrode geometry and bridge configuration.

The active stainless steel electrodes used by Bernier formed two diametrically opposed 90 degree circular arcs 6.35 mm in width and were flush mounted in a piece of lucite of the same diameter as the test section (10.16 cm) . He chose the axial dimension of the electrodes to be of the same order as the bubble size for good axial resolution of volume fraction. However, he found that the axial extent of his measurement was dictated by the spreading of the electric field caused by end effects rather than the electrode width. This field spreading effect was also found to be responsible for cross-talk between two electrode pairs if these were brought too close together, thereby preventing volume fraction measurements from being made close to one another.

With the objective of increasing the spatial resolution of the IVFM and of eliminating the cross-talk problem to allow a pair of IVFM's to operate accurately when closely spaced, shielding of the electrodes was introduced. Active electrodes similar to Bernier's were sandwiched between two 9.5 mm shielding electrodes that also form diametrically opposed 90 degree arcs. An isometric view of the described configuration is shown in Figure (4.1). The active electrode potential is duplicated onto the shielding electrodes with a high input impedance voltage buffer of gain one.

The resistance of the water was found to decrease significantly with increases in temperature caused by prolonged pumping of the water. Actual electrodes that are in contact with the water are used as a reference instead of variable resistors (as used by Bernier) to eliminate the drift in the IVFM signal caused by changes in electrical properties of the host fluid. The reference electrodes are a replica of those in the test section and are installed in the pure water part of the flow loop. The electrical bridge configuration is illustrated in Figure (4.2).

This addition therefore compensates for temperature fluctuations.

The bridge offset signal (caused by an imbalance in resistance between the reference and measuring electrodes) is demodulated and filtered in the signal processor to yield a voltage output proportional to the volume fraction. This process consists of multiplying the offset signal to the bridge driving signal and filtering out the 40 KHz component using a 500Hz low pass filter. No useful information is lost in filtering as the volume fraction signals in our experiments contain frequencies no higher than 100 Hz.

4.4 Steady state calibration of Impedance Volume Fraction Meter.

The calibration of the IVFM is carried out by measuring the liquid pressure gradient in the two-component medium. Two pressure tappings separated by a vertical distance of 1.694 m in the test section are connected to a differential pressure transducer. Under steady state conditions and zero liquid flow, the wall friction contribution to the pressure gradient is negligible. Therefore the pressure gradient in the test section is predominantly hydrostatic. The pressure difference is measured relative to the hydrostatic pressure difference in pure water since the lines leading to the pressure transducer were filled with water. Consequently, the volume fraction is linearly proportional to the monitored pressure difference for both solids and bubbles.

The volume fraction of air bubbles is given by the ratio of the measured pressure difference expressed as a head of water ΔH_{H_2O}, and L the distance between the taps:

$$\alpha(\%) = 100\frac{\Delta H_{H_2O}}{L}. \tag{4.1}$$

Similarly, the solid fraction of polyester particles in a solid-liquid flow is given by the following expression, where ρ_g, ρ_l and ρ_s are the air, water and polyester densities:

$$\nu(\%) = 100\frac{\Delta H_{H_2O}}{L}\left(\frac{\rho_l - \rho_g}{\rho_s - \rho_l}\right). \tag{4.2}$$

The IVFM is calibrated with both bubbly and particulate flows against the volume fraction obtained in this way from the static pressure gradient measurements. These two plots are shown in Figures (4.3) and (4.4).

$$\alpha(\%) = 6.53\overline{V} - 0.006. \tag{4.3}$$

$$\nu(\%) = 6.77\overline{V} - 0.41. \tag{4.4}$$

Equations (4.3) and (4.4) are the respective linear regression fits of these calibrations. The corresponding correlation coefficients for these fits are .9992 and .997. The discrepancy between the two fits (less than 1%) is attributed to experimental error in the measurement. Changes in the electrical properties of water are found to affect the slope of this calibration by $\pm 10\%$. For example after extensive pumping, which has the effect of warming up the water, the calibration becomes inaccurate. In practical terms, regular recalibration is required and was carried out. The IVFM is found to have excellent linearity up to volume fractions of at least 50%. With a sensitivity of .15 Volts per percent of volume fraction, the passage of individual bubbles (or particles) is readily detectable.

However, it must be noted that the calibration is a probably a function of the volume fraction distribution since the sensitivity of the IVFM is not uniform over the cross section. The volume fraction distribution has been shown to vary with total flow rate by a number of investigators. Therefore slight variations in the calibration can be expected for different flow rates.

4.5 Dynamic calibration of the IVFM.

4.5.1 IVFM output modelled as a shot-noise process.

The discrete nature of multicomponent flows typically causes measured flow quantities to exhibit fluctuations about a mean. It was shown by Bernier (1981) that the Impedance Volume Fraction Meter signal can be modelled as a shot-noise process. This was supported by the skewed fluctuating signal probability

density function which he demonstrated to shift toward a Gaussian distribution for larger volume fractions, as is expected according to the law of large numbers. We use the same approach for the new IVFM signals for bubbly and solids flows. Mathematically, the bubbly and particulate flows are equivalent. In the following outline of the shot-noise process, to prevent repetition, all the quantities refer to bubbly flows, but can be directly applied to solids flows. It is not the purpose of this section to describe in detail the shot-noise process; therefore some detail is omitted. More detail can be found in Papoulis (1965).

We model the volume fraction as a Poisson impulse distribution with each impulse representing a bubble. A Poisson process consists of a random distribution of constant magnitude impulses in time.

$$\alpha(\%) = 100\frac{\Upsilon}{Av_g}\sum_e \delta(t - t_e). \tag{4.5}$$

Here Υ is the volume of the bubble, A the pipe cross-sectional area, v_g the average gas velocity, δ is the Kronecker delta function, t is time and t_e are the points in time at which the bubbles pass the IVFM. The expected value of α is

$$\bar{\alpha}(\%) = 100\frac{\eta\Upsilon}{Av_g}, \tag{4.6}$$

where η is the density of the Poisson process or the number of events per unit time. As each bubble passes through the IVFM electric field, a "filter function" output signal represented by $h(t - t_e)$ is produced. The IVFM output voltage, V, is thus represented as the superposition of filter functions in time by the convolution integral of a Poisson impulse process (the volume fraction distribution) and the filter function.

$$V = \int_{-\infty}^{\infty} \alpha(t)h(t - \tau)d\tau. \tag{4.7}$$

The filter function is analogous to a weighting function over which the volume fraction measurement is made. The characteristic duration of this function is

representative of the residence time of a bubble in the influence volume of the IVFM electric field. This function is assumed to have the symmetric form:

$$h(t) = \begin{cases} He^{\xi t}, & t \leq 0; \\ He^{-\xi t}, & t \geq 0. \end{cases} \tag{4.8}$$

This filter function is by no means exact. Bernier (1981) showed that the auto-correlation function was not very sensitive to this function. The simple form assumed (only two unknown parameters) is therefore considered qualitatively adequate. The purpose of the dynamic calibration is to determine the variables H and ξ. Substituting (4.5) into (4.7) yields

$$V = \frac{\Upsilon}{Av_g} \sum_e h(t - t_e). \tag{4.9}$$

The expected value of V is obtained by averaging (4.9) in time:

$$\overline{V} = \frac{\eta \Upsilon}{Av_g} \int_{-\infty}^{\infty} h(t)dt, \tag{4.10}$$

and using (4.5)

$$\overline{V} = \bar{\alpha} \int_{-\infty}^{\infty} h(t)dt. \tag{4.11}$$

Thus the steady state IVFM calibration slope which we denote by m (see section (4.4)) such that

$$\overline{V} = m\bar{\alpha}, \tag{4.12}$$

is given by

$$m = \int_{-\infty}^{\infty} h(t)dt. \tag{4.13}$$

Hence integrating (4.8) yields

$$m = 2\frac{H}{\xi}. \tag{4.14}$$

Thus H can be eliminated by writing it in terms of m and ξ.

Now we are interested in the statistical properties of the fluctuating component of the IVFM output. The latter can be written as the convolution of the fluctuating component of the volume fraction $\tilde{\alpha}$ with the filter function:

$$\tilde{V} = \int_{-\infty}^{\infty} \tilde{\alpha}(t) h(t-\tau) d\tau. \tag{4.15}$$

By calculating the Fourier transform of the power spectrum of $\tilde{V}$ we obtain the following expression for the auto-correlation function of the fluctuating IVFM voltage:

$$R_{\tilde{V}\tilde{V}}(\tau) = R_{\tilde{V}\tilde{V}}(0) e^{-\xi|\tau|}(1+\xi|\tau|), \tag{4.16}$$

where the mean square of the fluctuations is given by

$$R_{\tilde{V}\tilde{V}}(0) = \overline{V}\left(\frac{m\Upsilon}{4A}\right)\left(\frac{\xi}{v_g}\right). \tag{4.17}$$

On the basis of (4.16) we proceed to experimentally determine ξ, which gives us a measure of the axial penetration of the IVFM influence field. In the following section, we show that the STNR based on (4.17) is only a function of volume fraction and geometric parameters.

4.5.2 The significance of auto-correlation properties.

Equation (4.16) provides us with a direct means of evaluating the fall off constant ξ from experimental auto-correlation records. These were obtained using a Hewlett Packard 3562 spectral analyser. A typical auto-correlation record is shown in Figure (4.5). The time $\tau_{1/2}$, at which the auto-correlation function has decayed to half of its maximum value, was noted for each record. The following relation is satisfied at that time:

$$e^{-\xi|\tau_{1/2}|}(1+\xi|\tau_{1/2}|) = \frac{1}{2}. \tag{4.18}$$

We numerically solve (4.18) for ξ in terms of $\tau_{1/2}$ to get:

$$\xi = 1.6783/\tau_{1/2}. \tag{4.19}$$

(4.19) is now used to derive ξ from the known $\tau_{1/2}$. The resulting time constants are plotted against the average bubble velocity in Figure (4.6). The ξ/v_g relationship is found to be close to linear and independent of volume fraction or of total flux. The linearity between the time constant ξ of fluctuations and the measured average bubble velocity is hardly surprising since the larger the velocity of the disperse medium, the shorter the residence time of the bubbles in the influence volume. In fact we expect the quantity in (4.17) to be close to constant for a homogeneous dispersion. Physically, this quantity is the decay constant of the spatial fall off in the IVFM influence function. Measured values of (v_g/ξ) (the axial extent of the IVFM field to one side of the plane formed by the electrodes) vary from $3\,mm$ for lower bubble velocities ($\sim .15\,m/s$) down to $2\,mm$ at higher velocities ($\sim .4\,m/s$). Since the influence volume of the electrodes is symmetric and falls off in sensitivity to both sides of the electrode plane, the axial length of the volume is twice the mentioned penetration. This measured dimension ranges from $4\,mm$ to $6\,mm$, which is of the same order as the average bubble size ($4\,mm$) and the electrode width ($6.35\,mm$).

Thus, since the volume of influence remains bounded within a narrow range, assuming it to be constant, the auto-correlation decay in time can be used to monitor the velocity of the dispersed medium. In practice this would be done by measuring ξ and reading off v_g from a calibration much like Figure (4.6).

Assuming the axial extent of the IVFM field (v_g/ξ) to be constant, (4.17) indicates that the mean square of the voltage fluctuations should then be linearly dependent on the mean IVFM voltage output for constant bubble volume and IVFM sensitivity. For convenience, we chose to present the magnitude of the fluctuations in terms of the dimensionless Signal To Noise Ratio (STNR) of the IVFM output. This is defined as the mean output voltage divided by the rms

value of the "noise" (fluctuations).

$$STNR = \frac{\overline{V}}{\sqrt{R_{\tilde{V}\tilde{V}}(0)}}. \tag{4.20}$$

Using (4.17) this becomes

$$\begin{aligned} STNR &= \sqrt{\frac{\overline{V}}{m}}\sqrt{\left(\frac{4A}{\Upsilon}\right)\left(\frac{v_g}{\xi}\right)}, \\ &= \sqrt{\overline{\alpha}}\sqrt{\left(\frac{4A}{\Upsilon}\right)\left(\frac{v_g}{\xi}\right)}. \end{aligned} \tag{4.21}$$

According to this analysis, the STNR is proportional to the square root of the mean volume fraction and the constant of proportionality is only a function of geometric parameters. The STNR is therefore independent of flow quantities other than the volume fraction. It is also independent of the slope of the calibration.

Experimental measurements of the STNR were made for steady state, constant volume fraction bubbly flows. The STNR was calculated from the $\tau = 0$ values of the auto-correlation records and the known mean IVFM outputs. The results are shown in Figure (4.7) and are plotted against the volume fraction of air. The curve displays the expected half power relation up to volume fractions of $\sim 25\%$, above which the STNR assumes higher values than predicted by the model as shown in Figure (4.7). Nevertheless, all bubbly flow points fall on the same curve irrespective of the total flux. The same experiments were carried out with solid-liquid flows. The particle flow STNR is shown against solid fraction in Figure (4.8). Again, all points fall on the same curve, and this curve coincides with the bubbly flow one in Figure (4.7), despite the difference of about 25% in the diameter of the bubbles and particles. We have thus demonstrated that not only does the average steady state IVFM output yield a measure of the volume fraction, but so do the statistical properties of the "noise". Moreover, the remarkable advantage of the STNR as a volume fraction indicator is its absence

in dependence on the device sensitivity. This property makes this measuring technique attractive in adverse conditions where recalibration of the IVFM is inconvenient if not impossible.

In Chapter 8 we explore the use of the IVFM in churn-turbulent air-water flows, as well as solid-water and three-component flows. There the statistical properties of the IVFM noise are used as a measure of flow quantities and as an indicator of flow regime.

4.6 Conclusion.

The Impedance Volume Fraction Meter with shielded electrodes is found to have excellent linearity up to volume fractions of at least 50%. The reason for which shielding was introduced was to decrease the axial penetration of the influence volume over which the measurement is made with the purpose of improving spatial resolution of dynamic volume fraction measurements. This goal was achieved, with an influence volume of approximately half of the original unshielded configuration.

The described dynamic calibration of the IVFM is based on measurements of the statistical properties of the fluctuations of the IVFM output. The maximum value and characteristic "width" of the auto-correlation function were used to describe these properties. For the mono-disperse bubbly and solids flows considered, the STNR which is representative of the size of the fluctuations can readily be used as a measure of volume fraction by means of the calibration curve in Figures (4.7) and (4.8). Also, the time constant of the IVFM output fluctuations calculated from measured cross-correlation records were close to being linearly related to the average gas velocity, as was shown in Figure (4.6).

The curve of the time constant ξ versus average gas velocity could also be used to measure the average gas velocity given the time constant. This method of determining the gas velocity involves computing the time the auto-correlation

takes to decay to a certain fraction of its $\tau = 0$ value. This technique contrasts favorably with the more demanding cross-correlation technique, in which the bubble speed is determined from the peak offset of the cross-correlation of two signals from two closely spaced transducers.

The fluctuations in the volume fraction signal contain a final bonus. Combining the volume fraction obtained from the STNR with the bubble velocity obtained from the filter function time constant ξ, we can compute the air volume flux j_{air} using the simple formula

$$j_{air} = \alpha v_g. \tag{4.22}$$

In summary, the concentration, speed and hence the flow rate of a mono-disperse medium can be extracted from the "noise" in the IVFM output.

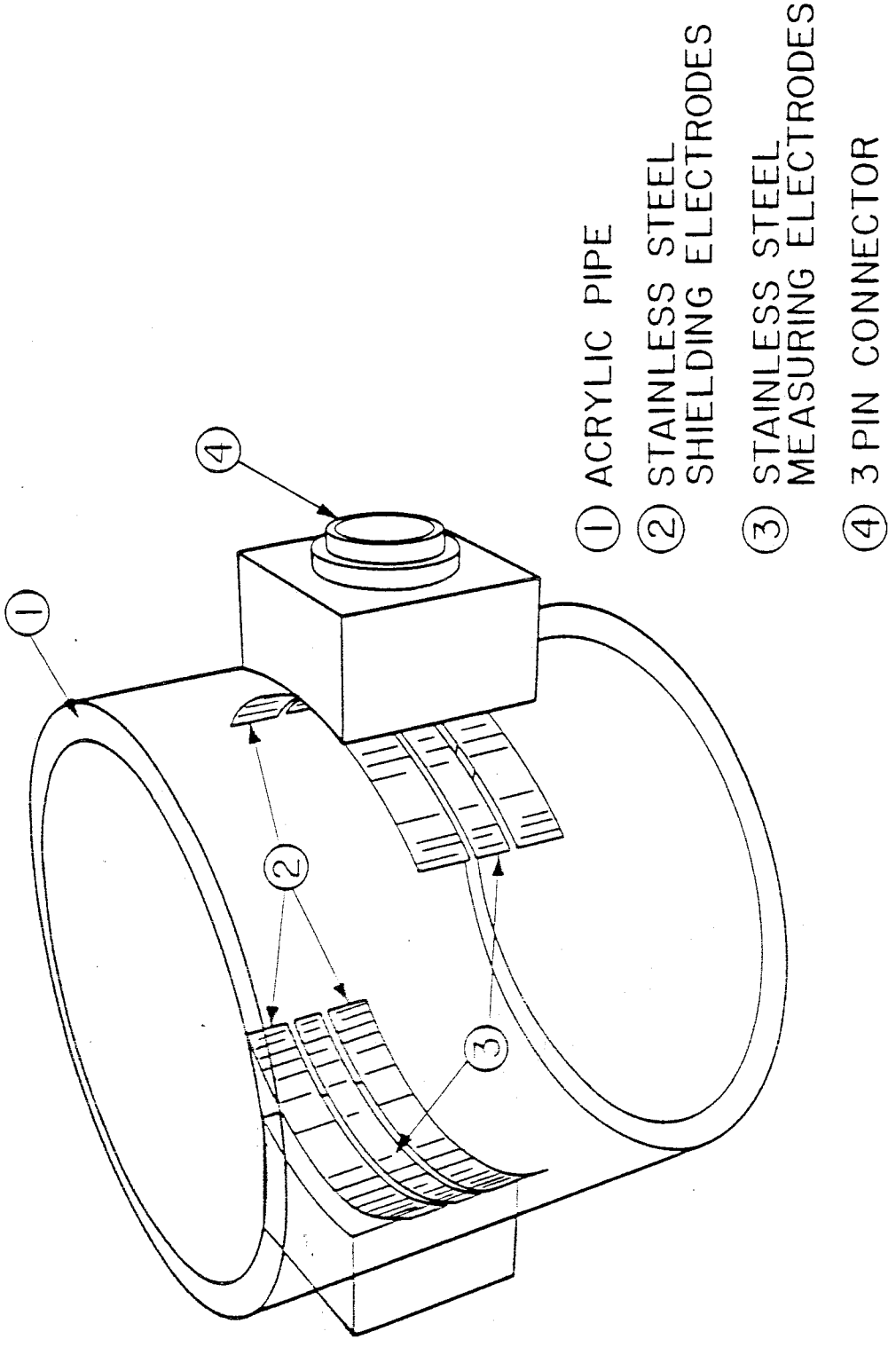

Figure (4.1) Isometric view of the shielded Impedance Volume Fraction Meter electrode geometry.

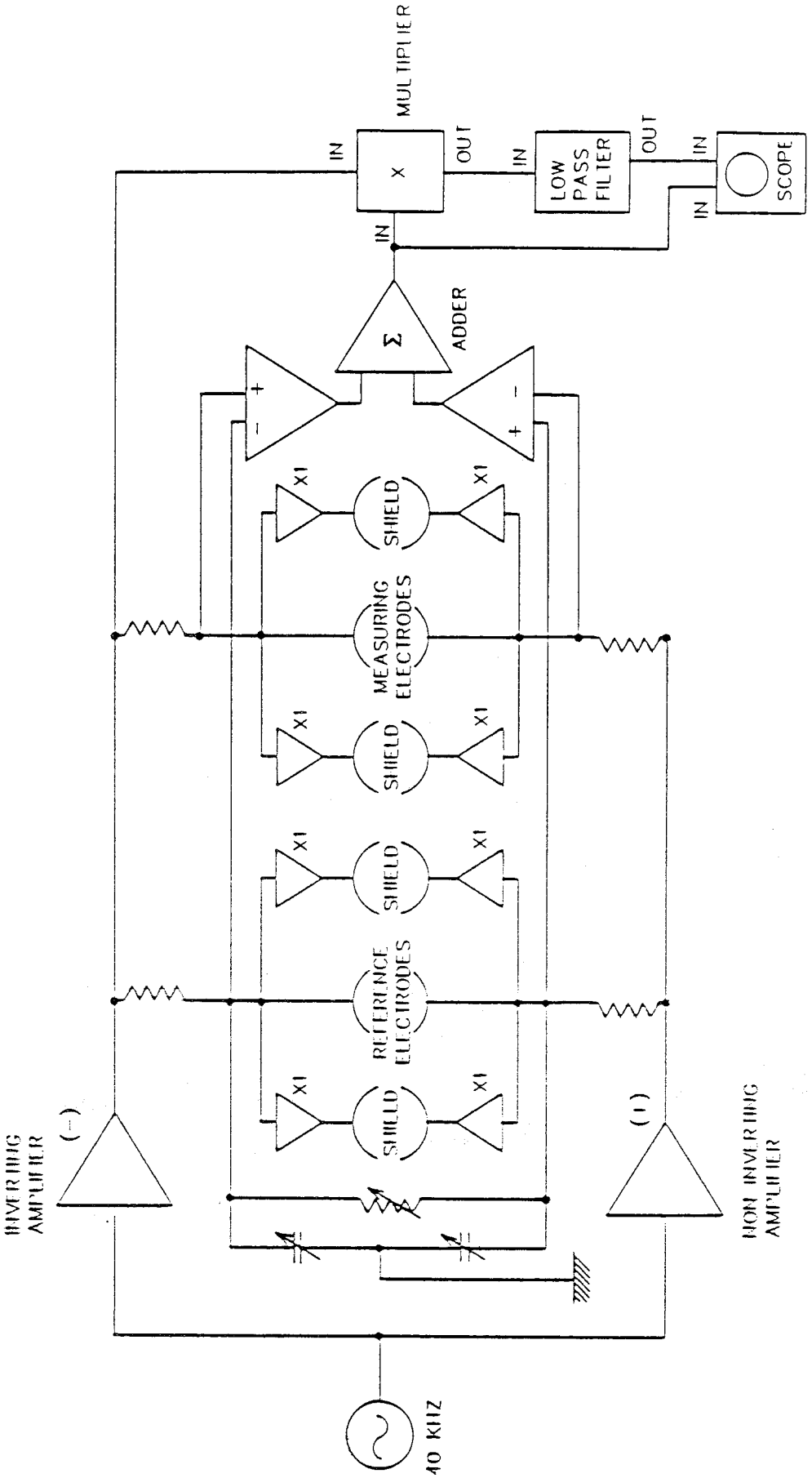

Figure (4.2) Schematic diagram of the Impedance Volume Fraction Meter signal processor.

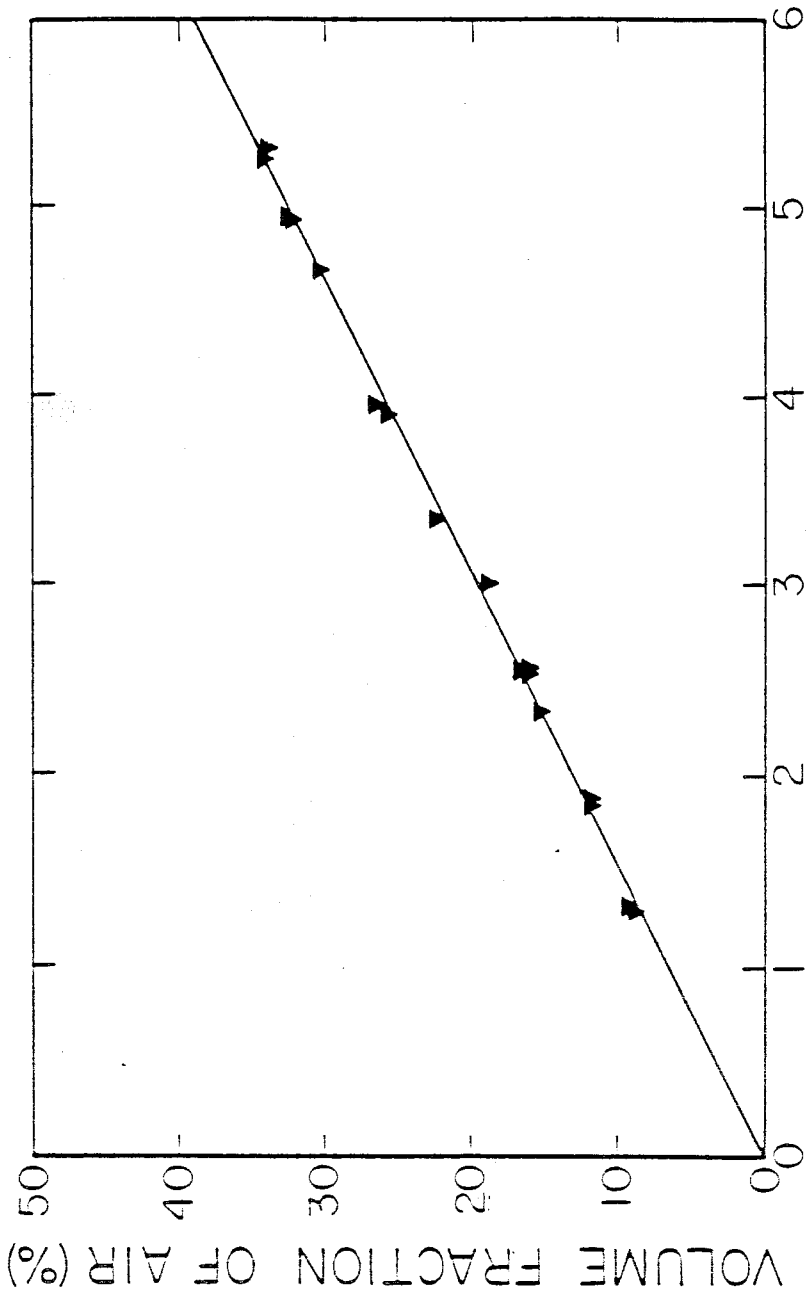

Figure (4.3) Steady state calibration of the Impedance Volume Fraction Meter with bubbly flows for zero water volumetric flux. The volume fraction was derived from the hydrostatic pressure gradient measurement.

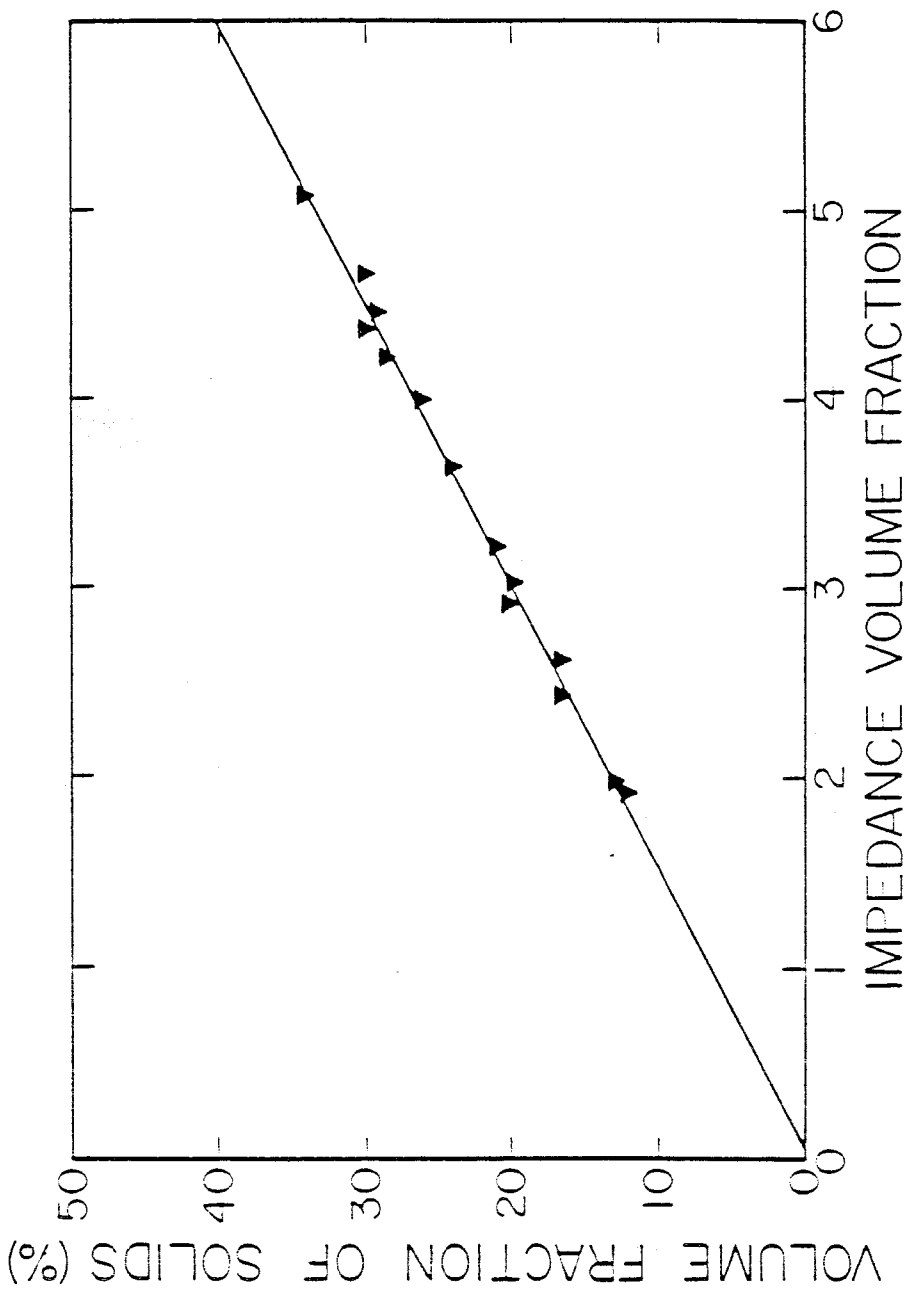

Figure (4.4) Steady state calibration of the Impedance Volume Fraction Meter with particulate flows for zero total volumetric flux. The volume fraction was derived from the hydrostatic pressure gradient measurement.

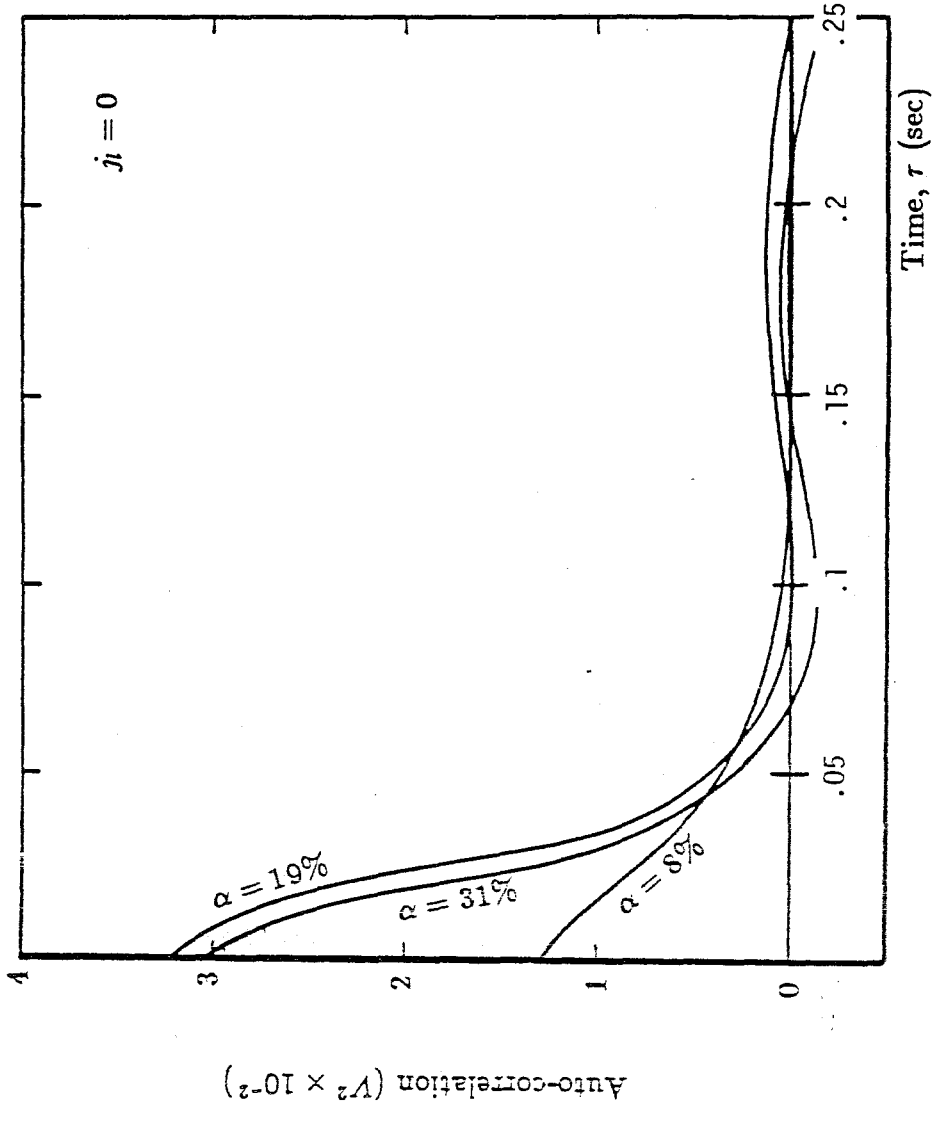

Figure (4.5) Typical auto-correlograms of the IVFM output fluctuations in a steady bubbly flow regime obtained from the HP 3562 Digital Signal Processor for a 60 second record.

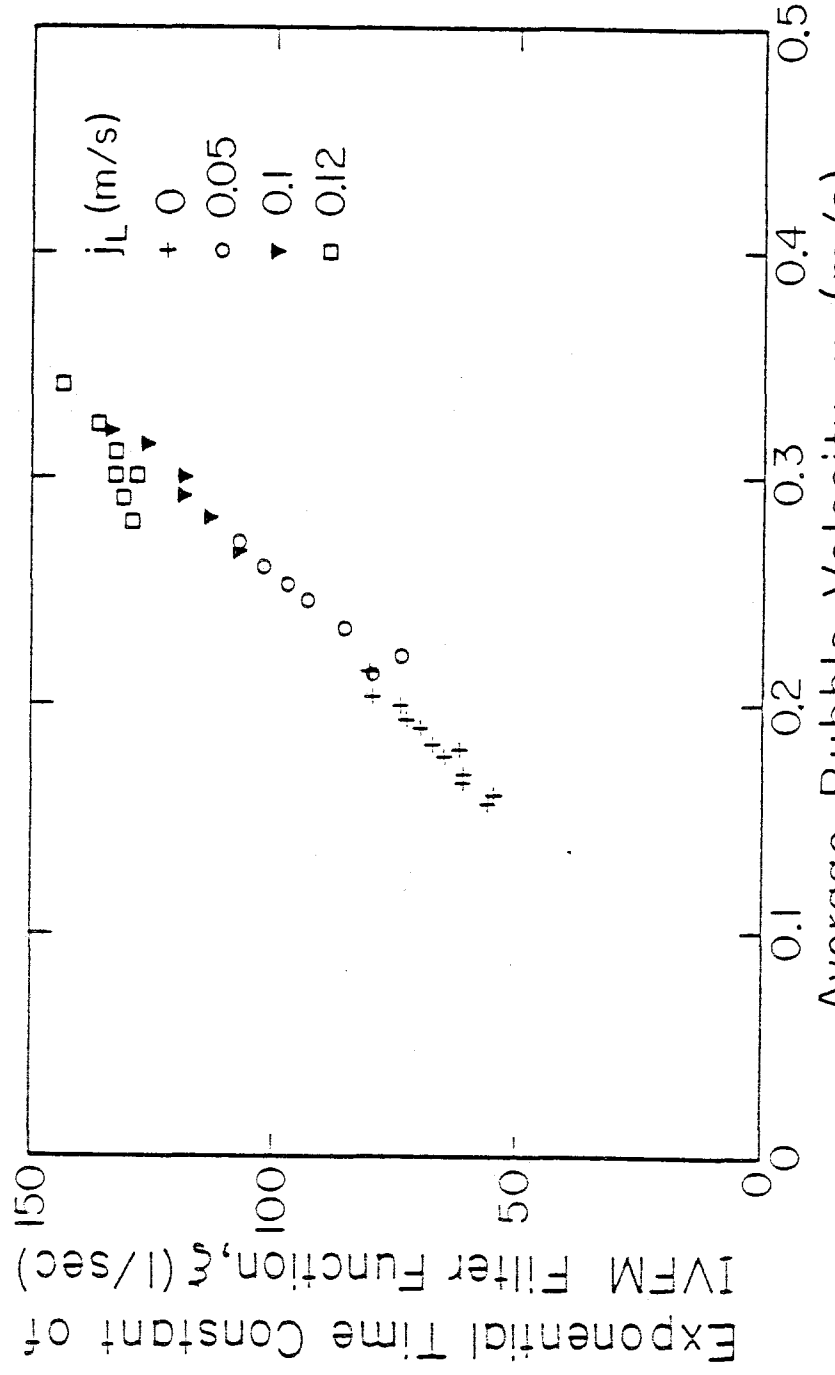

Figure (4.6) Time constant ξ of the IVFM output fluctuations versus the average bubble velocity for bubbly flows.

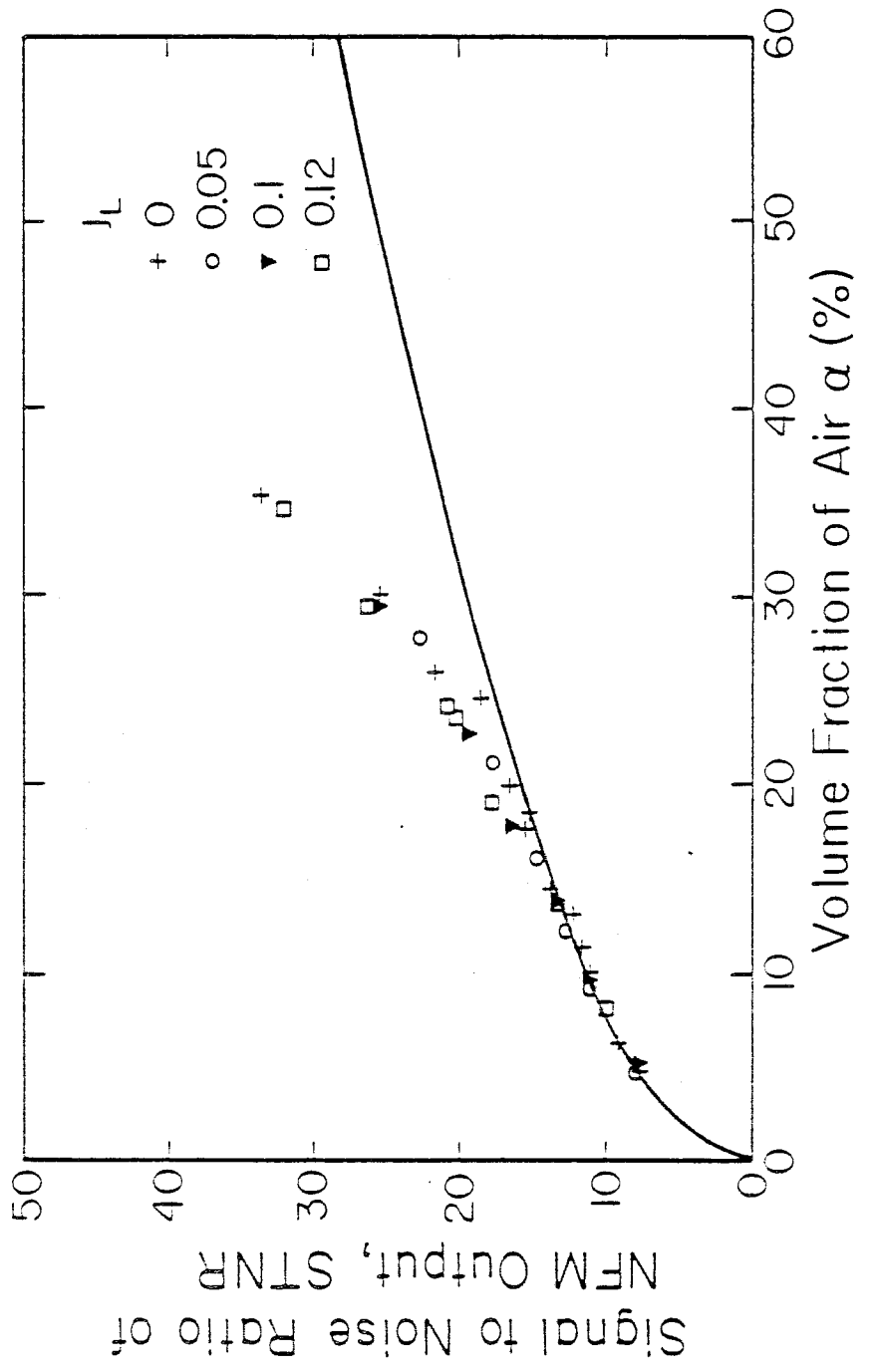

Figure (4.7) Signal To Noise Ratio of IVFM output for bubbly flows of different liquid fluxes plotted against air volume fraction. Also shown is the theoretical half power curve. The results deviate from this at an approximate volume fraction of 25%.

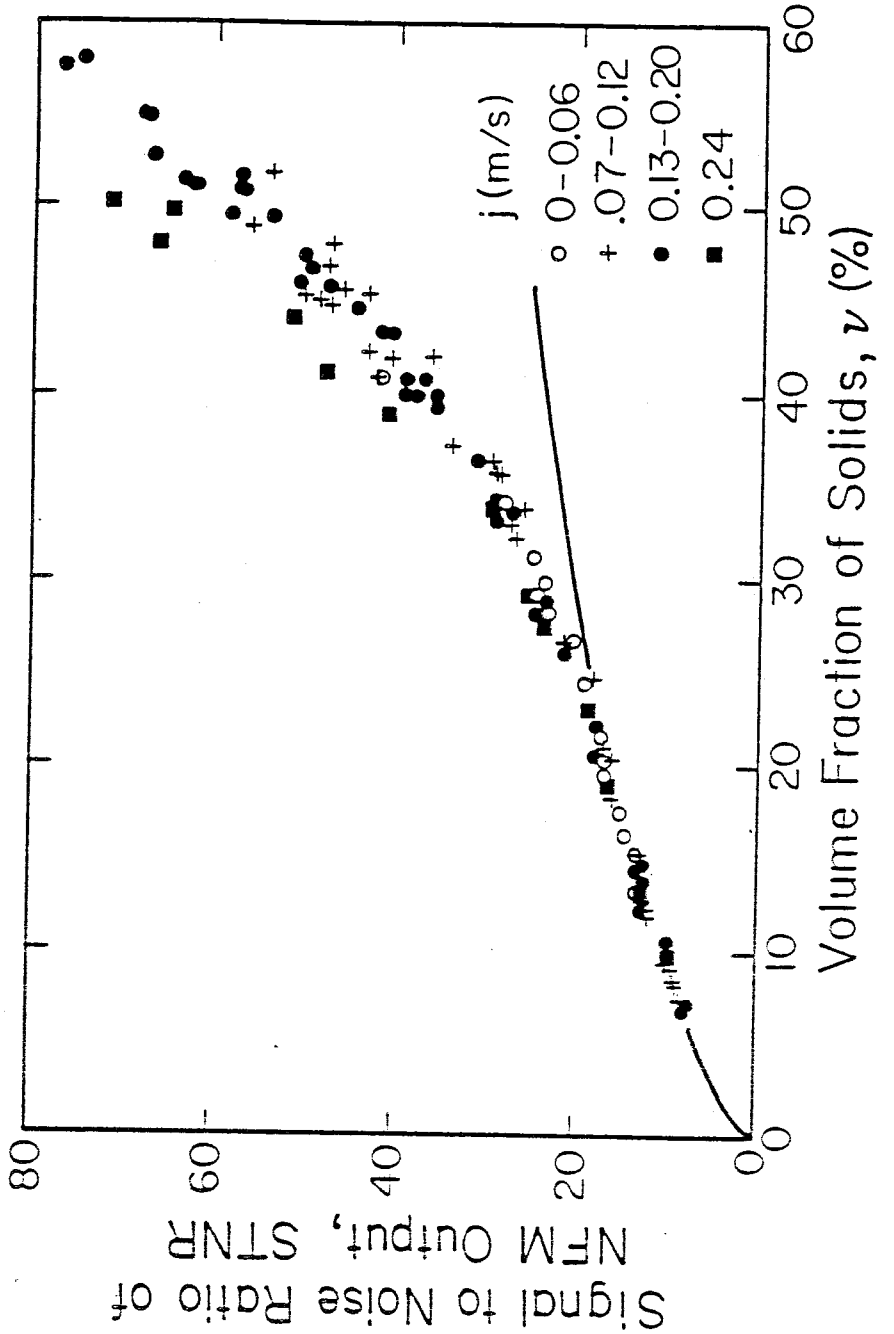

Figure (4.8) Signal To Noise Ratio of IVFM output for particle flows of different total fluxes plotted against the volume fraction of solids. Also shown is the theoretical half power curve. The results deviate from this at an approximate volume fraction of 25%.

Chapter 5. ONE DIMENSIONAL TWO-COMPONENT FLOW EQUATIONS.

5.1 Introduction.

In this chapter we summarize existing kinematic wave theories for incompressible bubbly and particulate one-dimensional, two component flows. Infinitesimal kinematic wave speeds and growth rates are obtained by studying the time behavior of small perturbations in volume fraction using the principles of conservation of mass and momentum.

Almost all conservation equations of two-component flows developed over the past three decades describe the medium as two interpenetrating and interacting continua. The variables are therefore averaged quantities over regions larger than the particle or bubble scale, but smaller than the small scale of the flow (bubble or particle diameter).

These models have led to better understanding of the properties of bubbly flows, fluidized beds, sedimentation processes and other two-component flows. However, many limitations and assumptions prevent the general use of any one existing set of equations due to the empirical way in which many effects have to be introduced. Indeed, we do not even know the exact solution for the unsteady flow of a single particle or bubble at large Reynolds numbers. Therefore, for example, in the particle equation of motion an experimentally obtained drag coefficient is used, a quantity which is very sensitive to the Reynolds number, and volume fraction.

Kynch (1952) derived a semi-empirical model for kinematic waves based on the assumption that unsteady effects in the momentum equation are negligible. The theory yields nondispersive infinitesimal kinematic wave speeds and predicts neutral stability for all wave numbers. The wave speed results of this model compare well with our experiments for both vertical bubbly and particle flows.

The issue of the stability of kinematic waves as a function of wave number is tackled in more detail by studying the full set of one-dimensional continuity and momentum equations. Derivations of the continuum equations by local volume averaging have been presented by many authors for different flow conditions (see Anderson and Jackson (1967,1968), Slattery (1967), Whitaker (1973) etc.). However, the observed relaxation effects in both finite and infinitesimal kinematic waves remain unexplained. Symington (1978) and Bernier (1981) both have shown that inertial effects are not responsible for these observed effects. The above efforts all have in common the assumption that the volume average of the product of two variables equals the product of the average of the variables. This assumption automatically rejects Reynolds-stress like terms. As shown by Anderson and Jackson (1967,1968), neglecting viscous effects other than the drag on the particle or bubble yields unstable infinitesimal kinematic waves for all wave numbers, contrary to the observed behavior. The additional inclusion of viscosity predicts a finite range of unstable waves for wave numbers between zero and a fixed value which depends on the initial volume fraction. Even though viscosity has a stabilizing effect on kinematic waves, it does not explain the observed stability of the air-water flows up to a volume fraction of 40% for bubbles in water and the complete stability of liquid-solid flows for all volume fractions.

Recent work by Batchelor (1986) on the stability of bi-disperse media provides a clue to what is missing from the theory. He visually demonstrated that concentration instabilities occur in media of two different dispersed species, one rising, the other falling in a liquid under the action of gravity . He then shows that a bi-disperse medium can become unstable due to the fluid mechanic coupling (interference) between the components, but stops short of estimating the magnitude of the coupling terms which are responsible for this phenomenon. In

this section we summarize Batchelor's work and proceed to estimate the previously undetermined coupling terms. These are then used to derive stability boundaries for an air-solids-liquid bi-disperse medium. These results are also applied to model a size-distributed mono-disperse medium as a bi-disperse system of two species of slightly different diameters. The stability boundaries are calculated for such a medium as a function of the two disperse species volume fractions. This kind of instability is found to resemble our real flow observations in its high total volume fraction onset.

5.2 Drift Flux model.

The Drift Flux Model was first introduced by Kynch (1952) and later embellished by Zuber (1964) to account for absolute flow rate effects. This model is based on the equations of continuity for the continuous and dispersed media, and the assumption that the relative velocity between the components is only a function of their respective volume fractions. Unsteady inertial and viscous effects are ignored, as well as effects of turbulent diffusion. Brownian diffusion is neglected as it is small for the size of particles and bubbles considered. For an infinite incompressible two-component medium with no heat or mass transfer the two one-dimensional continuity equations are

$$\frac{\partial \nu}{\partial t} + \frac{\partial (\nu v_d)}{\partial y} = 0, \tag{5.1}$$

for the disperse phase where ν and v_d are the volume fraction and the volume averaged speed of the dispersed medium respectively, and

$$\frac{\partial (1-\nu)}{\partial t} + \frac{\partial (1-\nu) v_c}{\partial y} = 0, \tag{5.2}$$

for the continuous phase where v_c is the volume averaged continuous phase velocity respectively. We define the average volumetric flux j as

$$j = \nu v_d + (1-\nu) v_c, \tag{5.3}$$

which is the sum of the continuous and dispersed phase fluxes. The addition of the continuity equations yields

$$\frac{\partial j}{\partial y} = 0. \tag{5.4}$$

Thus the volumetric flux depends only on time. A useful quantity is the average volumetric flux of the dispersed phase relative to the zero total flux plane, otherwise known as j_{dj}, the dispersed phase drift flux.

$$j_{dj} = \nu(v_d - j). \tag{5.5}$$

With the above definitions, this can be rewritten as

$$j_{dj} = \nu(1-\nu)v_{dc}, \tag{5.6}$$

where v_{dc} is the average relative velocity between the dispersed and the continuous phases. If the relative velocity is assumed to depend only on the volume fraction, then, the drift flux similarly depends only on ν. Using (5.5), v_d can be written in terms of the total flux, the drift flux and the volume fraction. Substituting v_d into (5.6) the dispersed phase continuity equation becomes

$$\frac{\partial \nu}{\partial t} + \left[j + \frac{\partial j_{dj}}{\partial \nu} \right] \frac{\partial \nu}{\partial y} = 0, \tag{5.7}$$

since j_{dj} is assumed to depend only on volume fraction. This equality has the general form of a quasilinear first order wave equation:

$$\frac{\partial \nu}{\partial t} + C_i \frac{\partial \nu}{\partial y} = 0, \tag{5.8}$$

where

$$C_i = \left[j + \frac{\partial j_{dj}}{\partial \nu} \right]. \tag{5.9}$$

C_i represents the propagation speed of infinitesimal perturbations in volume fraction and is a function of total volumetric flux and the derivative of the

drift flux function with respect to volume fraction. The validity of the predicted infinitesimal kinematic wave speeds is established in Chapter (6) where measured wave speeds are compared with predictions based on the experimentally obtained drift flux curve for bubbly flows. It should be noted that this equation predicts neutrally stable perturbations in volume fraction.

Due to the dependence of C_i on volume fraction, the latter can easily be shown to develop stable shocks using the method of characteristics. This has also been shown experimentally. The speed of shocks, or sudden discontinuities in volume fraction is obtained by applying the principles of conservation of mass across the "jump". The same result is also obtained by requiring continuous partial derivatives in a direction parallel to the shock in the y,t plane used to present characteristics. The speed of the shock is thus found to be

$$C_s = \frac{j_{dj}(\nu_2) - j_{dj}(\nu_1)}{\nu_2 - \nu_1}. \tag{5.10}$$

In Chapter 6, the above equation in conjunction with the drift flux curve is shown to accurately predict shock speeds for bubbly flows.

5.3 Equations of motion.

Unsteady inertial, viscous and Reynolds-stress like effects which were ignored in the above section can be introduced with the two-component momentum equations. These can be derived by applying momentum conservation principles to two components separately (Anderson and Jackson (1967,1968)) or by writing one equation for the two-component medium and the other for the motion of a single bubble or particle (Symington 1978). These two derivations are equivalent, in fact one set of equations can be derived from the other. In the equation of motion care must be taken to include the effect of volume fraction. It is easy to show that the steady state hydrostatic pressure gradient in the continuous phase is linearly proportional to the bulk density of the medium, and not

the liquid density as assumed by Symington. The buoyancy force on a sinking particle is increased by this effect which is responsible for the well documented decrease in steady state relative velocity between phases as a function of volume fraction.

We present these equations in the form derived by Symington with the added pressure gradient term in the particle equation of motion. The general one-dimensional combined momentum equation for the two-component medium is

$$\begin{aligned}\rho_c(1-\nu)\left[\frac{\partial v_c}{\partial t}+v_c\frac{\partial v_c}{\partial y}\right]+(\rho_d+K\rho_c)\nu\left[\frac{\partial v_d}{\partial t}+v_d\frac{\partial v_d}{\partial y}\right]= \\ -\frac{\partial p}{\partial y}+\mu(1-\nu)\frac{\partial^2 v_l}{\partial y^2}-\rho_c(1-\nu)\frac{\partial\overline{(v_c')^2}}{\partial y}-(\rho_d+K\rho_c)\nu\frac{\partial\overline{(v_d')^2}}{\partial y} \\ -\rho_c(1-\nu)g-\rho_d\nu g,\end{aligned} \tag{5.11}$$

where ρ_c and ρ_d are the component densities, p is the liquid pressure, g is the acceleration due to gravity and μ is the liquid viscosity. The terms $\overline{(v_c')^2}$ and $\overline{(v_d')^2}$ are the volume averages of the products of the fluctuating components of velocities and are not necessarily small. These terms are strong functions of the disperse volume fraction and are commonly called the Reynolds-stresses. K is a coefficient representative of the added mass for each particle. It is commonly taken to be $\frac{1}{2}$, which is obtained from the potential flow field around a sphere. However van Wijngaarden (1976) has shown that K can be a strong function of ν. The particle equation of motion is

$$\begin{aligned}(\rho_d+K\rho_c)\left[\frac{\partial v_d}{\partial t}+v_d\frac{\partial v_d}{\partial y}\right]= \\ -\frac{\partial p}{\partial y}-(\rho_d+K\rho_c)\frac{\partial\overline{(v_d')^2}}{\partial y}-\frac{3}{2}\frac{\rho_c C_D}{D_p}|v_d-v_c|(v_d-v_c)-\rho_d g,\end{aligned} \tag{5.12}$$

where D_p is the particle diameter,and $C_D(\nu, Re)$ is the drag coefficient for a

single sphere. It is based on the relative velocity between the two components.

$$C_D = \frac{F_D}{\frac{1}{2}\rho_d(u_d - u_c)^2}, \tag{5.13}$$

where F_D is the drag force on the particle. For a given dispersed species, C_D is found to increase with volume fraction. In these equations we have neglected particle-particle pressures, which are of importance at high volume fractions ($\sim$ 50%). Particle-particle stresses are addressed in a study of "solidification" waves in solid-liquid flows in Chapter 7. The liquid pressure term can be eliminated by combining (5.11) and (5.12) to yield

$$\begin{aligned}\rho_c(1-\nu)\left[\frac{\partial v_c}{\partial t} + v_c\frac{\partial v_c}{\partial y}\right] - (\rho_d + K\rho_c)(1-\nu)\left[\frac{\partial v_d}{\partial t} + v_d\frac{\partial v_d}{\partial y}\right] \\ - \mu(1-\nu)\frac{\partial^2 v_c}{\partial y^2} + \rho_c(1-\nu)\frac{\partial\overline{(v_c')^2}}{\partial y} - (\rho_d + K\rho_c)(1-\nu)\frac{\partial\overline{(v_d')^2}}{\partial y} \\ - \frac{3}{4}\frac{C_D\rho_c}{D_p}|v_d - v_c|(v_d - v_c) - (\rho_d - \rho_c)(1-\nu)g \quad = 0.\end{aligned} \tag{5.14}$$

Equations (5.1),(5.2) and (5.14) form a system of three non-linear partial differential equations for unsteady one-dimensional two-component flows.

5.4 Linear Stability of an Unbounded Two-Component Medium.

This analysis addresses the stability of volume fraction perturbations in an initially uniform medium. Both Reynolds and viscous stresses are neglected. The value of the variables for the uniform flow solution is denoted by the suffix 0. These quantities identically satisfy all four equations. A small perturbation is applied to the variables about the uniform flow solution, writing

$$v_d = v_{d0} + v_d^*, \quad v_c = v_{c0} + v_c^*, \quad \nu = \nu_0 + \nu^*. \tag{5.15}$$

These are substituted into (5.1),(5.2) and (5.14). For an observer following the continuous medium, making use of the uniform flow solution and linearizing we

obtain the following perturbation order equations:

$$\frac{\partial \nu^*}{\partial t} - v_{cd0}\frac{\partial \nu^*}{\partial y} + \nu_0 \frac{\partial v_d^*}{\partial y} = 0, \qquad (5.16)$$

$$-\frac{\partial \nu^*}{\partial t} + (1-\nu_0)\frac{\partial v_c^*}{\partial y} = 0, \qquad (5.17)$$

$$\rho_c(1-\nu_0)\frac{\partial v_c^*}{\partial t} - (\rho_d + C\rho_c)(1-\nu_0)\left[\frac{\partial v_d^*}{\partial t} + v_{cd0}\frac{\partial v_d^*}{\partial y}\right] + (\rho_d - \rho_c)g\nu^* + \frac{3}{2}\frac{C_D\rho_c}{D_p}v_{cd0}|v_c^* - v_d^*| = 0, \qquad (5.18)$$

where v_{cd0} is the relative uniform flow velocity between the continuous and the dispersed media. This quantity is a function of volume fraction for a given dispersed species. To model this we choose a simple and adequate empirical form for the dependence of v_{cd0} on ν_0 which was obtained by fitting data for bubbly flows.

$$v_{cd0} = V_0(1-\nu_0)^{\frac{3}{2}}. \qquad (5.19)$$

From (5.19) and the uniform flow equations, setting time and space derivatives to zero in (5.18), we obtain a corresponding expression for the dependence of C_D on ν_0:

$$C_D(\nu_0) = C_D|_{\nu_0=0}\frac{1}{(1-\nu_0)^2}, \qquad (5.20)$$

We then substitute (5.20) into (5.18). One-dimensional plane wave solutions of (5.16),(5.17) and (5.18) are sought in the form

$$q^* = Qe^{(\kappa - i\omega)\frac{V_0 t}{D_p} + in\frac{y}{D_p}}, \qquad (5.21)$$

where q^* is a generic variable, κ is the dimensionless time constant of the perturbation, ω the reduced frequency and n the dimensionless wave number. The scales V_0 and D_p are introduced for the purpose of non-dimensionalization. Real solutions for the mentioned variables are sought. The amplitude Q is complex in general. Using (5.21) the set of equations reduces to a set of three linear

homogeneous algebraic equations with three unknowns, the amplitudes of the variables. A non-trivial solution exists only if the determinant of the coefficient matrix vanishes. Applying this condition yields the functions $\kappa(n,\nu_0)$ and $\omega(n,\nu_0)$ which describe all plane wave solutions. The determinant of the matrix is complex; therefore both its real and imaginary parts must vanish. The two equations obtained are shown here in dimensionless form.

$$\kappa^2\ [(\rho^*+K)(1-\nu_0)+\nu_0]+\kappa\ \left[\frac{2(\rho^*-1)}{Fr^2(1-\nu_0)^{\frac{3}{2}}}\right] - \left[(1-\nu_0)(\rho^*+K)\left(\omega+n(1-\nu_0)^{\frac{3}{2}}\right)^2+\omega^2\nu_0\right]=0, \tag{5.22}$$

$$\kappa=-\frac{(\rho^*-1)}{Fr^2(1-\nu_0)^3}\left\{\frac{\omega+n(1-\frac{3}{2}\nu_0)(1-\nu_0)^{\frac{3}{2}}}{\omega\left[\frac{(\rho^*+K)(1-\nu_0)+1}{(1-\nu_0)^{\frac{3}{2}}}\right]+n(\rho^*+K)(1-\nu_0)}\right\}, \tag{5.23}$$

where ρ^* is the density ratio (ρ_d/ρ_c) and Fr is the Froude number based on the particle diameter D_p, $(V_0/\sqrt{gD_p})$. Equations (5.22) and (5.23) can be reduced to a single fourth order algebraic equation for κ, with two real and two imaginary roots. The form of (3.22) requires its real solutions to occur in pairs of values opposite in sign for all values of the wave number. This signifies that there are both stable and unstable solutions. An iterative scheme is used to obtain the real solutions for the reduced time constant $\kappa(n,\nu_0)$ and $S(n,\nu_0)$,the reduced perturbation propagation speed which is defined as

$$S(n,\nu_0)=\frac{C_i}{V_0}\quad=\frac{\omega}{n}. \tag{5.24}$$

The negative real solution to (3.26) is large in size ($\kappa<-1$) in comparison with the positive real root. It describes an attenuation of kinematic waves of typical decay length of the order of the particle diameter. Since we are considering

length scales much larger than the particle diameter, this result is not meaningful. The positive time constant is found to increase monotonically with the wave number. This was demonstrated by Jackson (1963). It is practically more interesting to compare the stability at different volume fractions. For a given wave number, the time constant is shown in Figure (5.1) to reach a maximum at $\nu_0 \sim 20\%$ and to always remain positive for volume fractions up to 50%. It should be noted that our model is no longer meaningful at wave numbers corresponding to wave lengths of the order of the particle separation since considering such small dimensions in the flow violates the averaging assumption that only length scales significantly larger than particle separation can be considered. For this reason our results are presented up to $n = .8$, which corresponds to a minimum wavelength considered of approximately $8D_p$. The kinematic wave speed S is shown to be relatively insensitive to wave number in Figure (5.2). In summary, inertial effects have a destabilizing effect on two-component media for all wave numbers. The infinitesimal kinematic speed however is hardly affected by including these effects.

The purpose of this section was to study the stability of mono-disperse media which were predicted to be neutrally stable for all wave lengths of the perturbation by the Drift Flux Model. The infinitesimal kinematic wave speeds calculated from the set of continuity and momentum equations used are found to fall close to the results of the quasi-steady Drift Flux Model. The effect of inertia was introduced by means of the equations of motion of both the disperse and continuous media. For an inviscid two-phase flow, neglecting effects of the pipe wall, it has a destabilizing effect on the two-component system. All wave lengths are found to be unstable for all volume fractions, with a least stable volume fraction of $\sim 20\%$. The growth rate of the perturbation increases monotonically with wave number. Anderson & Jackson (1968) showed that viscosity

stabilizes the high wave number perturbations, leaving a range of unstable wave numbers. Experimental observations reveal that vertical air-water flows are stable up to a volume fraction of $\sim 40\%$, and our solid-liquid flows are stable for all volume fractions. We conclude that neither inertial or viscous effects explain the observed stability of the vertical two-component flows studied.

5.5 Effect of Size Distribution.

All real multi-component flows exhibit a distribution in the dispersed medium diameter. Considering only the continuity of individual particle size groups, Batchelor (1986) showed that flow interference between these groups can lead to instability of the initial distribution in one-dimensional unbounded three- component flows. In his model for bi-disperse flows, the stability of the dispersion depends on the influence of one size group on the flow rate of the other as a function of the two volume fractions. Batchelor falls short of quantifying this function which is vital to the stability analysis. In the next section, we outline Batchelor's model and, making certain assumptions, proceed to quantitatively estimate the flow coupling function between species for a general bi-disperse flow. We apply the model to an air-solids-liquid three component flow for which we determine the stability boundary. The bi-disperse analysis is also used to determine the stability boundary of a size-distributed mono-disperse flow modelled as medium of two species with a diameter difference representative of the width of the size-distribution.

5.5.1 Batchelor's bi-disperse model.

This model is based on the continuity equations of the two individual disperse species. Let us consider a bi-dispersed medium which consists of two distinct particle sizes. The continuity equations, one for each species, are

$$\frac{\partial \nu_1}{\partial t} + \frac{\partial (\nu_1 v_{d1})}{\partial y} = 0, \tag{5.25}$$

$$\frac{\partial \nu_2}{\partial t} + \frac{\partial (\nu_2 v_{d2})}{\partial y} = 0. \tag{5.26}$$

As in the Drift Flux model, it is now assumed that for a given total flux, the fluxes of the components are only a function of the two volume fractions. (5.25) and (5.26) thus become

$$\frac{\partial \nu_1}{\partial t} + D_{11}(\nu_1, \nu_2)\frac{\partial \nu_1}{\partial y} + D_{12}(\nu_1, \nu_2)\frac{\partial \nu_2}{\partial y} = 0, \tag{5.27}$$

$$\frac{\partial \nu_2}{\partial t} + D_{21}(\nu_1, \nu_2)\frac{\partial \nu_1}{\partial y} + D_{22}(\nu_1, \nu_2)\frac{\partial \nu_2}{\partial y} = 0. \tag{5.28}$$

where D_{ij} is the rate of change of flux of component i with respect to the volume fraction of component j.

$$D_{ij} = \left.\frac{\partial \nu_i v_i}{\partial \nu_j}\right|_{\nu_1, \nu_2} \quad \text{(no summation over } i\text{)}, \tag{5.29}$$

(5.27) and (5.28) can be written as a matrix equation. Let us call $[D_{ij}]$ the flux matrix. The system of two quasi-linear partial differential equations is perturbed about the uniform flow solution to study the linear stability of the bi-disperse medium. A perturbation order solution of the form of a plane wave is sought as imposed by (5.23). The problem is now reduced to two simultaneous algebraic equations for the amplitudes of the perturbations. A non-trivial solution exists only if the determinant of the coefficient matrix vanishes. From this condition we get the non-dimensional wave speed S $(= \omega/n)$ and time constant κ.

$$S = \frac{D_{11} + D_{22}}{2V_0}, \tag{5.30}$$

$$\kappa^2 = \left[1 + \frac{4D_{12}D_{21}}{(D_{11} + D_{22})^2}\right]\left(\frac{D}{V_0}\right)^2. \tag{5.31}$$

For the flow to be unstable, κ must be positive. This can only occur if

$$(D_{11} + D_{22})^2 + 4D_{12}D_{21} < 0. \tag{5.32}$$

5.5.2 Bi-disperse stability analysis.

The flux matrix is derived by calculating the velocity of each of the disperse components relative to the liquid through a steady state force balance. The forces considered are the weight of the particle, the buoyancy force and the drag on the particle. The weight of the particle of species i is

$$W_i = \rho_{di} g \frac{\pi D_i^3}{6} \quad (i = 1, 2). \tag{5.33}$$

The buoyancy force is the product of the liquid pressure gradient and the volume of the particle. In a fluidized medium, the particles are supported by the continuous phase (the liquid). It follows that the liquid pressure gradient is linearly proportional to the bulk density, not the liquid density. The buoyancy force, B_i on a particle of species i is

$$B_i = \left[(1 - \nu_1 - \nu_2)\rho_c + \nu_1 \rho_{d1} + \nu_2 \rho_{d2}\right] g \frac{\pi D_i^3}{6} \quad (i = 1, 2). \tag{5.34}$$

In an infinite bi-disperse medium, the drag coefficient of the particles depends on the volume fractions of the two species, and there is the additional effect of forces imposed by one species on the other, that become important at large volume fractions. Lockett and Al-Habbooby (1973,1974) obtained good agreement with experimental data for the vertical sedimentation of low Reynolds number bi-disperse systems by assuming that the fall velocity of a particle relative to the liquid depended only on the total local particle concentration and applying a known mono-disperse sedimentation velocity correlation. This approach is adopted to derive the drag on a particle. For a mono-disperse medium, the particle drag coefficient was found indirectly from measurements of the relative velocity of the two components. The derived dependence of the drag coefficient on volume fraction is depicted by (5.21). Using (5.21), and writing the sum of the disperse volume fractions instead of the single mono-disperse ν, the

bi-disperse drag coefficients are:

$$C_{Di} = \frac{4}{3}\frac{gD_i}{V_{0_i}^2}\frac{(\rho_{di}-\rho_c)}{\rho_c}\frac{1}{(1-\nu_1-\nu_2)^2} \quad (i=1,2), \tag{5.35}$$

where the suffixes $_1$ and $_2$ denote disperse components 1 and 2. This approach is convenient, but it underestimates the extent of hindering to the particle velocities at higher volume fractions, since we have neglected the effect of particle collisions.

The sum of the forces given by (5.33)-(5.35) on a particle of species i settling at a steady speed is equated to zero. This equation gives us the average velocity of each disperse component relative to the liquid:

$$\begin{aligned}\frac{v_{dci}}{V_{0i}} &= f_i(\nu_i,\nu_j,\gamma),\\ &= (1-\nu_i-\nu_j)^{\frac{3}{2}}\,(1-\nu_i-\gamma\nu_j)\,,\end{aligned} \tag{5.36}$$

where

$$\gamma = \frac{\rho_{dj}-\rho_c}{\rho_{di}-\rho_c}, \tag{5.36}$$

for (i =1,2), (j =1,2) and $i \neq j$, with no summation over repeated indices.

The flux of the two components can written in terms of the relative velocities:

$$\nu_1 v_{d1} = \nu_1(1-\nu_1)f_1V_{01} - \nu_1\nu_2V_{02}f_2, \tag{5.37}$$

$$\nu_2 v_{d2} = \nu_2(1-\nu_2)f_2V_{02} - \nu_2\nu_1V_{01}f_1. \tag{5.38}$$

The desired $D_{ij}(\nu_1,\nu_2)$ are then derived by differentiating the flux of species i in (5.37) and (5.38) with respect to the volume fraction of species j. The infinitesimal kinematic speeds and stability boundaries for bi-disperse media can now be computed using (5.32).

To apply this analysis to a specific problem, we need to specify the terminal velocities of each species relative to the fluid at zero volume fraction (V_{01} and V_{02})

and the density ratio parameter γ. This is done below for two problems of interest to demonstrate the typical high volume fraction onset of this class of instability.

5.5.3 Instability in bi-disperse air-solids-liquid flow.

The stability of the three component medium studied experimentally in Chapter 7 is analysed in this section. The material of the disperse media are air bubbles and polyester particles; water is the continuous medium. The bubbles and particles have average diameters of $4\,mm$ and $3\,mm$, respectively. The pertinent material properties for our analysis are the densities and terminal velocities relative to the liquid at zero volume fraction:

$$solids: \quad \rho_{d1} = 1429\,Kg/m^3 \quad V_{01} = .13\,m/s, \tag{5.39}$$

$$air: \quad \rho_{d2} = 1.43\,Kg/m^3 \quad V_{02} = .24\,m/s, \tag{5.40}$$

$$liquid: \quad \rho_c = 1000\,Kg/m^3. \tag{5.41}$$

These constants are substituted into (5.36)-(5.38). For each set of volume fraction pairs, the flux matrix $[D_{ij}]$ is derived by numerically differentiating the individual component fluxes in (5.37) and (5.38). Then we test to see if the inequality (5.32) is satisfied. If it is not, the flow is considered neutrally stable, if it is, the flow is unstable. The volume fractions of both disperse species were scanned from 0 to 50%, and the result of the test is displayed in Figure (5.3). The curve shown separates the region of neutral stability and instability. To the larger volume fraction side of the curve, the dispersions are predicted to be unstable. For values of air volume fraction above 14% or values of solids fraction above 12%, the flow is is expected to always be unstable.

5.5.4 Size-distribution driven instability in mono-disperse media.

We now proceed to another application and examine bi-disperse mixtures of particles or bubbles with the same density but slightly different diameter.

The difference in the diameters chosen is representative of the width of the size-distribution in a mixture with a narrow size-distribution in such a way that 50% of the particles fall between these sizes. These are $D_{mean} + .67\sigma$ and $D_{mean} - .67\sigma$ where D_{mean} is the mean diameter and σ is the standard deviation of the distribution being modelled. Values pertinent to the experimental observations were obtained photographically for the bubbles and directly measured for the particles.

$$D_{bubble} = 4\ mm \quad \sigma = .7\ mm, \tag{5.42}$$

$$D_{particle} = 3\ mm \quad \sigma = .5\ mm. \tag{5.43}$$

Based on the above values and the densities of the materials, and imposing the equality in (5.32), we obtain stability boundaries for the described bi-disperse bubbly and particulate flows. These are shown in Figures (5.4) and (5.5). According to this model, instabilities set in at volume fractions much higher than are physically attainable. The maximum volume fraction for a narrow size-distribution of particles is typically 60%, whereas this analysis predicts onset of the instability at total volume fractions above 80%. However, one must recall that the hindrance is underestimated with the exclusion of forces between disperse species. Including these effects is expected to bring the stability boundary to lower volume fraction values. The nature of this instability in its onset at high volume fraction is similar to what is observed in the experiments unlike the results of the mono-disperse models considered. Therefore instabilities driven by size-distribution may dominate in the flows studied.

The speed of the infinitesimal kinematic waves (equation (5.30)) is similar in form to the mono-disperse Drift Flux Model result where it was found to be the rate of change of the flux of the disperse medium with respect to its volume fraction. For the bi-disperse case, the wave speed is simply the mean of these two quantities, one for each constituent. By observation, for a narrow

size distribution of the kind considered, C_i is not expected to differ significantly from the mono-disperse result. Indeed, this is shown to be the case in Figure (5.6), for the particulate and bubbly flows considered. The experimental results are decribed in detail in Chapter 6.

5.6 Conclusion.

In this chapter we studied the stability of one-dimensional two-component flows of intermediate Reynolds numbers using three different models based on the conservation equations. The Drift Flux model is the simplest. It is a quasi-steady model based on the equation of continuity and the assumption that the relative (slip) velocity is only a function of the volume fraction. The momentum equations were then introduced to account for inertial effects. This is followed by a brief discussion of the effect of including viscosity in the model. Finally, the influence of size distribution and coupling between different size groups on the stability of the flow is studied.

The three linear perturbation approaches to infinitesimal kinematic waves analysed yield similar results for the wave propagation speed. The differences are seen in the growth rate of the perturbations. The Drift Flux Model yields neutrally stable waves for all wave numbers. Inertial effects are found to have a destabilizing effect on the two-phase medium predicting all wave numbers to be unstable with the larger wave numbers (short wave lengths in perturbation) being the least stable. Size-distribution is taken into account by modelling the size-distributed two-component medium as a bi-disperse system. The drag coefficient of the individual particles is assumed to depend on the total volume fraction only, and forces between the dispersed species are neglected. This analysis yields unstable kinematic waves at very high volume fractions $\sim 80\%$. The hindrance between species is underestimated here; including particle-particle pressures is likely to bring down the stability boundary to lower values of vol-

ume fraction. No wave number dependence of wave speed or growth rate is obtained in this model. The results of the three models considered are limited by the continuum assumption which breaks down at wave lengths of the order of the particle separation. The developed bi-disperse model is used to find stability criteria in terms of the constituent volume fractions for an air-solid-liquid mixture consisting of air bubbles and polyester particles in water. This analysis predicts instability of the mixture if the volume fraction of either constituent is approximately 15% or above. The resulting stability boundary is compared to experimental observations in Chapter 8.

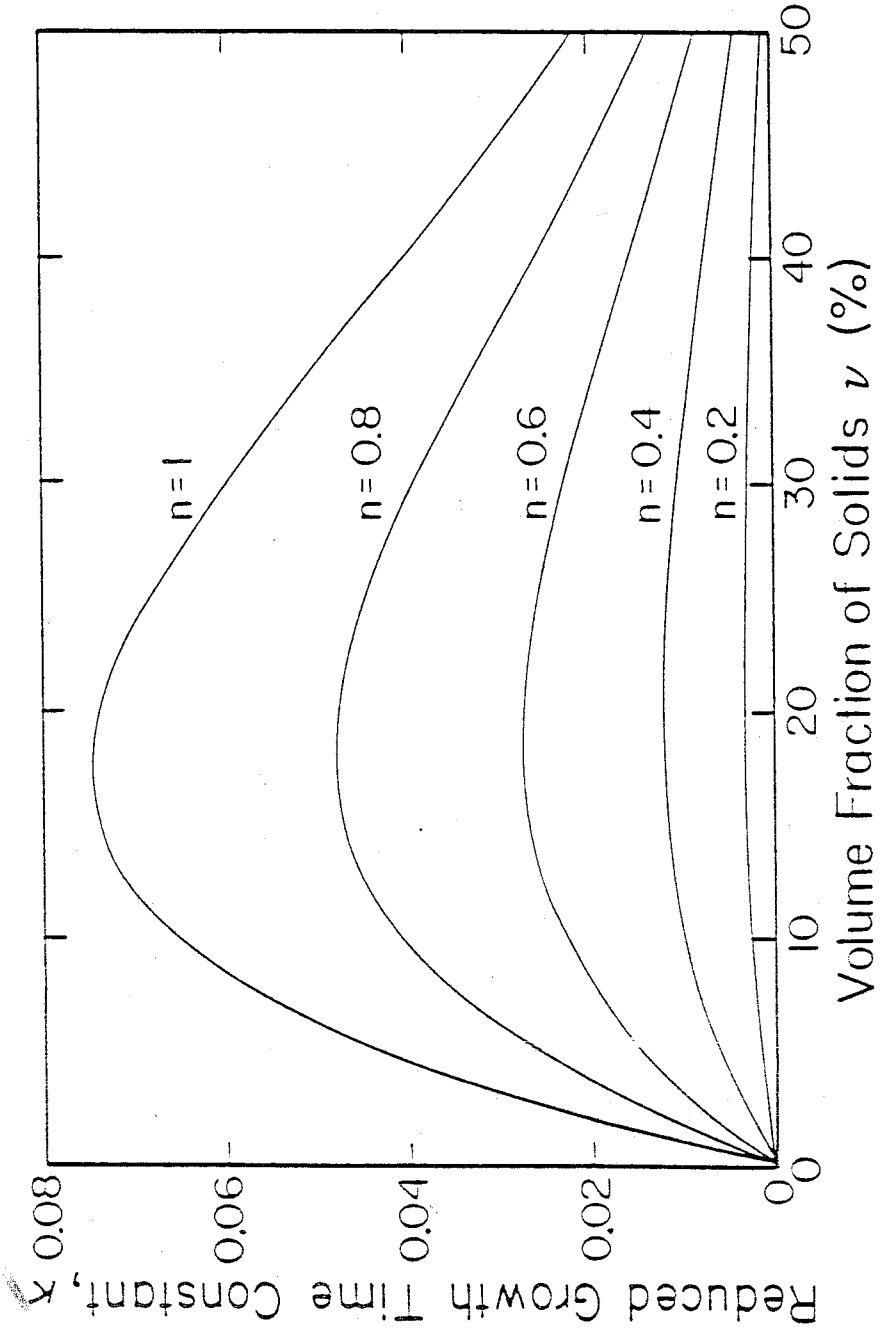

Figure (5.1) Calculated reduced time constant κ of kinematic waves based on the two-component continuity and momentum equations including inertial effects with no viscous terms. This plot indicates that the larger wave numbers are more unstable and that there is a preferred, least stable, volume fraction of $\sim 20\%$.

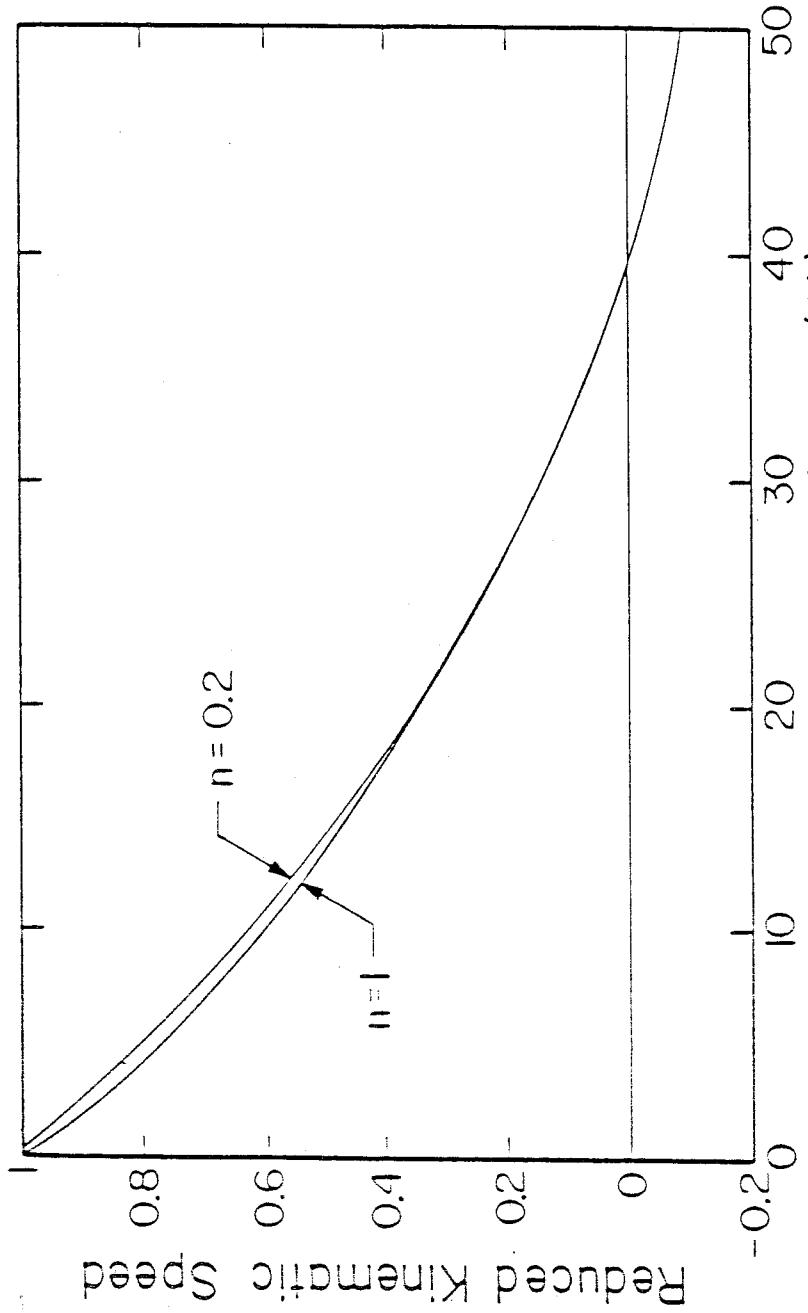

Figure (5.2) Calculated dimensionless infinitesimal kinematic wave speed based on the two-component continuity and momentum equations including inertial effects with no viscous terms.

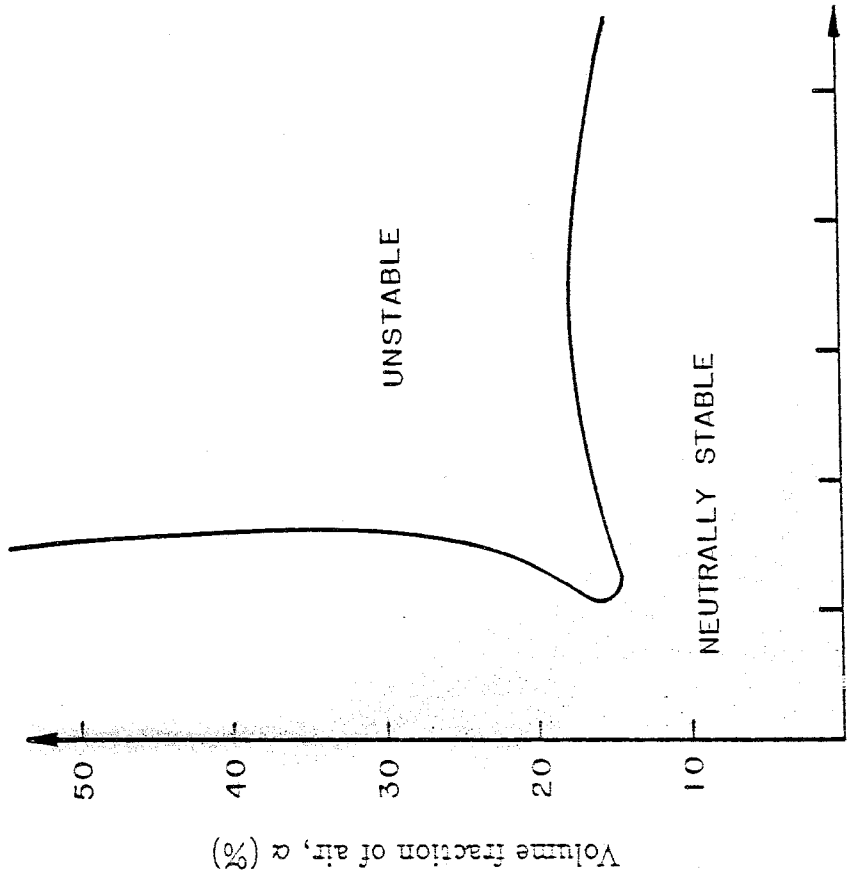

Figure (5.3) Stability boundary of gas-solid-liquid bi-disperse flows (mean particle diameter 3 mm, density 1429 Kg/m^3, and mean bubble diameter 4 mm, density 1.43 Kg/m^3) based on the bi-disperse flow model.

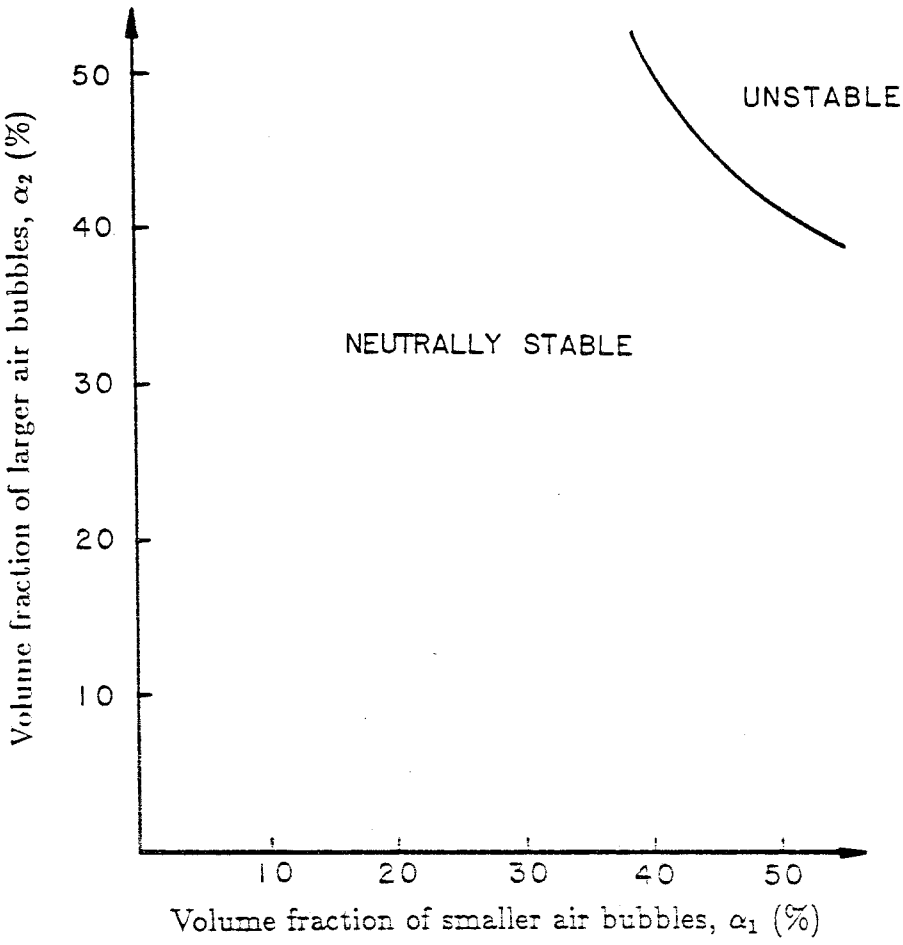

Figure (5.4) Stability boundary of size distributed bubbly flows based on the bi-dispersed flow model assuming the size distribution can be represented by two distinct size groups. The size difference between groups is taken as 1.34σ, the size distribution standard deviation.

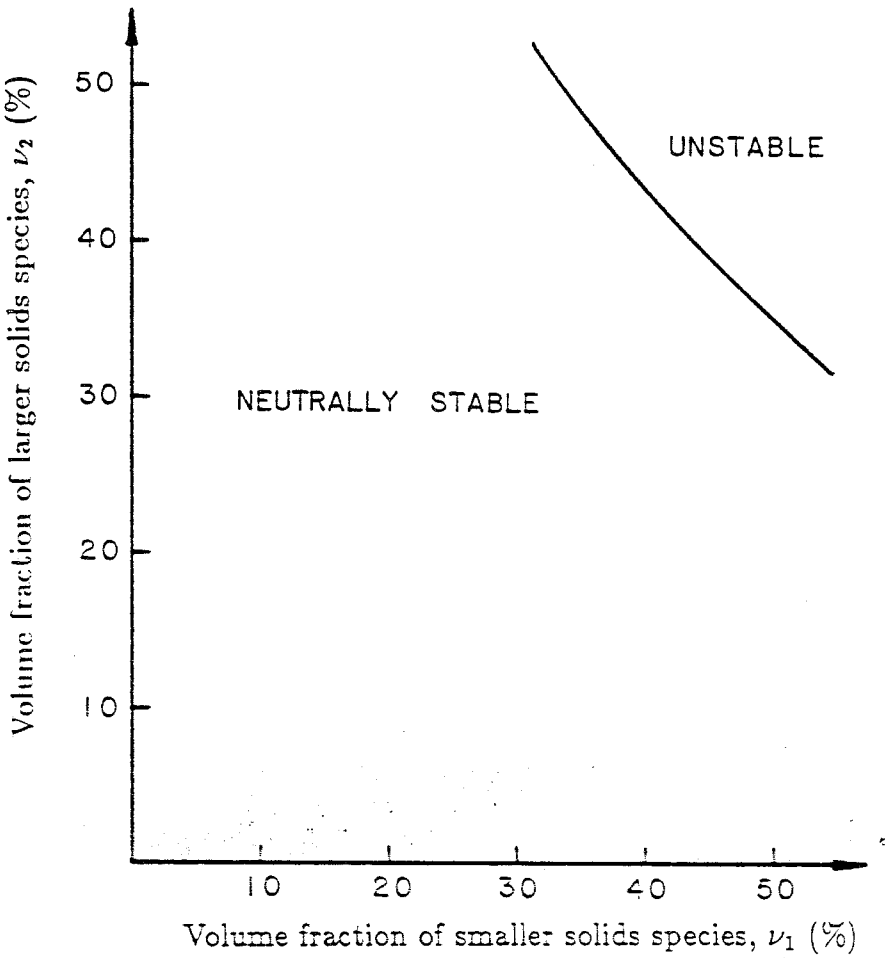

Figure (5.5) Stability boundary of size distributed solid-liquid flows based on the bi-dispersed flow model assuming the size distribution can be represented by two distinct size groups. The size difference between groups is taken as 1.34σ, the size distribution standard deviation.

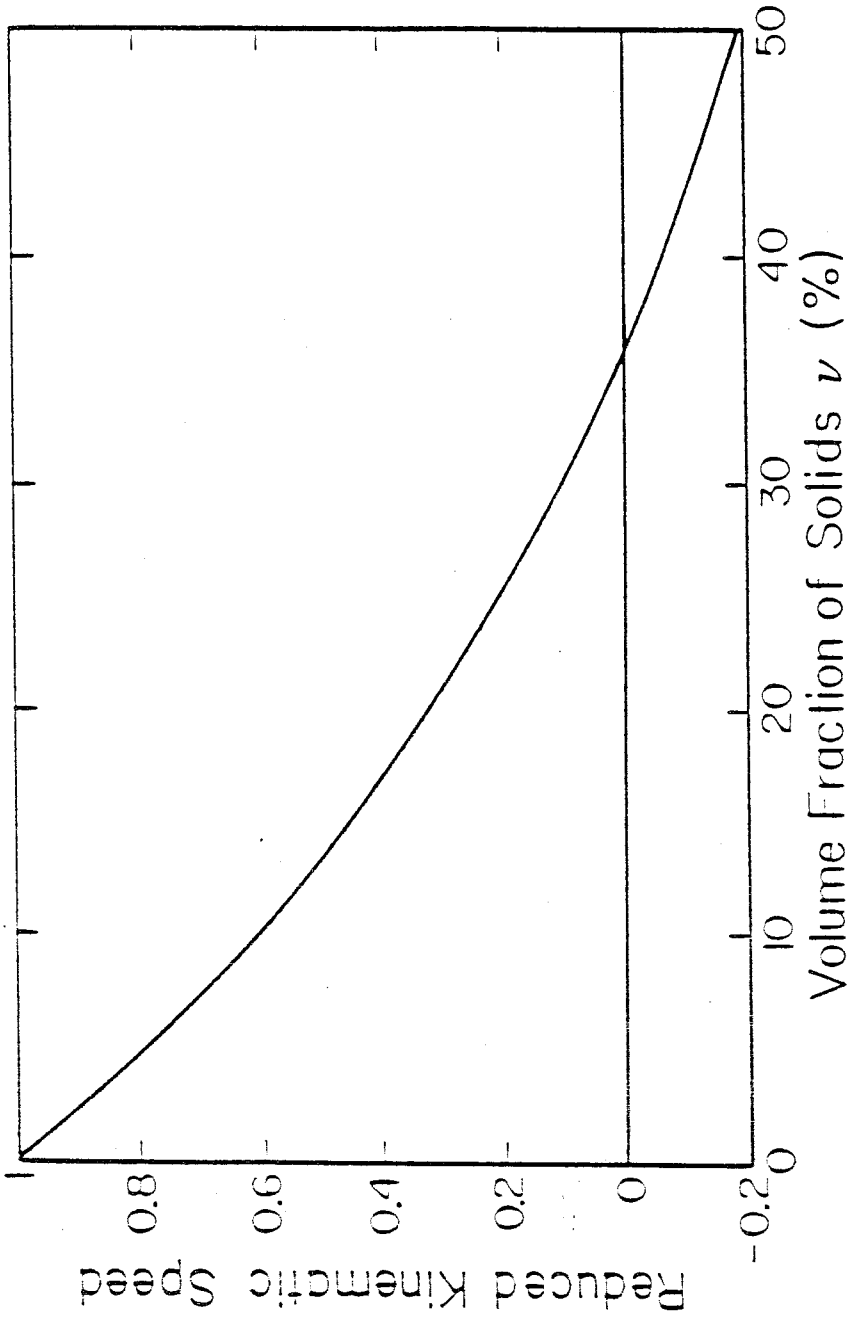

Figure (5.6) Reduced infinitesimal kinematic wave speed in narrowly distributed bi-disperse flow with equal concentrations of the two components.

Chapter 6. EXPERIMENTAL ANALYSIS OF SMALL AMPLITUDE KINEMATIC WAVES.

6.1 Introduction.

The aim in this chapter is to measure the propagation speed and growth rate of small amplitude kinematic waves in steady state vertical bubbly and particulate flows.

This can be done by imposing a perturbation of known size in volume fraction at a known location and following its evolution in time. Such an approach is limited by the difficulty involved in accurately throttling the disperse medium to create an small amplitude perturbation. Alternatively, naturally occurring random fluctuations in volume fraction can be used as the perturbations of which the speed and growth rate are sought. This is the method used in our study . For this, the "noise" in the volume fraction signals at two closely spaced locations is statistically manipulated to yield the travelling speed and attenuation of coherent volume fraction fluctuations.

6.2 The Cross Correlation Function and its Interpretation.

In Chapter 4, we established that the spatial resolution of the IVFM is of the order of 1 cm in the axial direction, and that the influence volume of the measurement remains unchanged for volume fractions and flow rates considered. These properties make the IVFM suitable for the study of volume fraction perturbations over a broad range of wave lengths. The shielded electrode configuration eliminates the problem of cross-talk when two IVFM's are used close to one another. Measurements of the fluctuations in the volume fraction signal were made simultaneously at two closely spaced locations (h=.0735 m) under steady flow and volume fraction conditions for both bubbly and particulate flows. The fluctuating components of the signal pair were cross-correlated to yield the residence time of coherent signal between the two concentration transducers. The residence time is obtained from the location in time of the peak in cross-correlograms. Knowing the time taken by the coherent signal to travel from one IVFM to the other, and the distance between the electrode pairs, we calculate the speed of propagation of information in the two component flows in question.

The cross-correlation ($R_{\tilde{V}_1\tilde{V}_2}$) of the fluctuating components of the two IVFM signals is defined as

$$R_{\tilde{V}_1\tilde{V}_2}(\tau) = \lim_{T\to\infty} \frac{1}{T} \int_0^T \tilde{V}_1(t)\tilde{V}_2(t+\tau)\, dt, \tag{6.1}$$

where $\tilde{V}_1$ and $\tilde{V}_2$ are the fluctuations of the IVFM outputs under steady state conditions. Since the separation h of the IVFM's is known, we obtain the speed of propagation of this information:

$$v_{Xcorr} = \frac{h}{\tau_{max}}, \tag{6.2}$$

There exists some ambiguity in the interpretation of the transport speed This propagation velocity is shown below to be the infinitesimal kinematic speed

by comparing it with the disperse medium velocities (of bubbles and particles) and the infinitesimal kinematic wave velocities as obtained using the Drift Flux Model.

The IVFM fluctuating component was obtained by passing the IVFM output signal through a high pass filter with a $3dB$ cut off frequency of $.032Hz$ and a fall off slope of $10dB$ per octave. The filter output was recorded on magnetic tape for reduction. The record length used was $1\,minute$. Cross-correlations of simultaneously recorded data from the two IVFM's were obtained on an $HP\,3562a$ signal processor. 50 ensemble averages of the cross-correlation, each of length of $1\,second$, proved to be adequate to give repeatable results. Typical cross-correlations are shown in Figure (6.1).

Bernier (1981), who used an unshielded IVFM electrode configuration showed that the velocity obtained through cross-correlation was the kinematic wave speed, not the speed of bubbles. As the other extreme, it has been shown that the cross-correlation peaks from the signals of two point volume fraction measuring devices such as hot film anemometers or fiber optic probes separated by a small distance (of the order of the diameter of the dispersed medium) correspond to the dispersed medium transport time. To verify that the speeds measured here are indeed kinematic wave speeds and not that of the disperse medium, we compare cross-correlation speeds to actual bubble and particle speeds and kinematic wave speeds as predicted by the Drift Flux Model.

The bubble speed relative to the liquid is obtained from the measured air and water fluxes (j_{air} and j_{water}) and ν the volume fraction using

$$v_{air} = \frac{j_{air}}{A\nu} - \frac{j_{water}}{A(1-\nu)}. \tag{6.3}$$

The kinematic wave speed relative to the liquid is derived using the Drift Flux Model outlined in Chapter 5. It is directly dependent on the relative velocity-volume fraction function obtained experimentally. The bubble velocity, the Drift

Flux infinitesimal kinematic wave speed and the transport velocity obtained using the outlined cross-correlation technique are compared in Figure (6.2). The results eliminate the ambiguity in interpretation of our measurement and conclude that cross-correlation of IVFM fluctuations yields the speed of infinitesimal kinematic waves for bubbly flows.

In polyester particle-water flows we are unable to directly measure the particle speed. The particle velocity relative to water as a function of volume fraction was obtained indirectly by measuring the propagation speed of finite kinematic shocks. This method which is outlined in more detail in Chapter 7 gives us the particle velocity as the third order function of volume fraction which best fits the kinematic shock speed results. The particle velocity, the infinitesimal kinematic wave speed obtained from it and the transport velocity deduced from cross-correlation measurements are compared in Figure (6.3). These velocities are presented relative to the liquid. The results allow us to conclude, as for bubbles, that peaks in the cross-correlation of the IVFM fluctuations for steady polyester particle-water flows correspond to the residence time of infinitesimal kinematic waves between the IVFM's.

6.3 The Non-dispersive Nature of Infinitesimal Kinematic Waves

The IVFM fluctuations are shown by the cross-correlations to be transported in the flow as infinitesimal kinematic waves. For the stable steady two-component flows observed, we model the continuous reordering of the disperse species from one measuring location to the other as an attenuation of coherent signal from one IVFM to the other and a generation of uncorrelated noise. The amplitude of the uncorrelated signal equals the amount removed from the coherent signal through the attenuation, such that the power spectra of the fluctuations of the two IVFM's are the same, as measured experimentally, and shown in Figure (6.4) for both bubbly and particulate flows. In general both the

attenuation of the kinematic waves and their residence time between the IVFM's depend on the wave number. For this reason, the above model is best described in the frequency domain in terms of the wave number of the perturbations. The wave number and the frequency are linearly related by the following expression:

$$N = \frac{\omega}{v_{Xcorr}}. \tag{6.4}$$

For kinematic waves travelling from IVFM1 to IVFM2, the Fourier-transform of the measured fluctuations can therefore be written as

$$\tilde{\mathbf{V}}_1(N) = \frac{1}{2\pi}\int_{-\infty}^{\infty} e^{-int}\tilde{V}_1(t)dt, \tag{6.5}$$

$$\tilde{\mathbf{V}}_2(N) = \varsigma(N)e^{-iNT(N)}\tilde{\mathbf{V}}_1(N) + \tilde{\mathbf{V}}_{2\,uncorr.}, \tag{6.6}$$

where $\varsigma(N)$ is the attenuation and $T(N)$ the transit time of the perturbation of wave number N between the two detector positions. The $e^{-iNT(N)}$ factor is the characteristic "time delay exponential" which arises when taking the Fourier-transform of a signal with a time lag. $\tilde{\mathbf{V}}_{2\,uncorr.}$ is a fluctuation term which is uncorrelated to $\tilde{\mathbf{V}}_1$.

The well defined cross-correlation peaks obtained indicate that signal structure propagates at a fixed speed for each record. If the waves were strongly dispersive, the peaks would be much broader. By analysing the problem in the frequency domain we can find the frequency dependence of the delay time. This is best done by studying the phase of the cross-power spectrum of the fluctuations of IVFM1 and IVFM2. This is defined as

$$S_{\tilde{V}_1\tilde{V}_2} = \tilde{\mathbf{V}}_1^*(N)\tilde{\mathbf{V}}_2(N), \tag{6.7}$$

where * denotes the complex conjugate of the function to which it is applied. Substituting (6.6) into (6.7) we obtain

$$S_{\tilde{V}_1\tilde{V}_2} = \varsigma(N)e^{-iNT(N)}S_{\tilde{V}_1\tilde{V}_1}, \tag{6.8}$$

where $S_{\tilde{V}_1\tilde{V}_1}$ is the power spectrum of the fluctuations of IVFM1, and is defined as

$$S_{\tilde{V}_1\tilde{V}_1} = \tilde{\mathbf{V}}_1^*(N)\tilde{\mathbf{V}}_1(N). \tag{6.9}$$

Power spectra are real functions, therefore the phase $\phi(N)$ of the cross-power spectrum in (6.8) is

$$\phi(N) = -NT(N). \tag{6.10}$$

The cross-power spectrum phase was evaluated on the signal processor for the recorded data used for the cross-correlation measurements; typical results are shown in Figure (6.5). The phase was found to be linear in N in the region where the cross-power spectrum amplitude is significant for both bubbly and particulate flows; in other words, $T(N)$ is independent of the wave number. This confirms our earlier statement that the kinematic waves are non-dispersive. Therefore the slope of the phase is the time lag of the signal between the two detectors. This was compared to the time lag obtained using the cross-correlation technique. The two were found to be consistent.

6.4 The Attenuation of Infinitesimal Kinematic Waves.

The main motivation behind shielding the electrodes of the IVFM was to improve the spatial resolution of the device thereby allowing us to study the properties of short wave length infinitesimal kinematic waves ($< .1m$), which have eluded many authors due to the large geometry of their measuring devices. This was successfully accomplished as indicated by the power spectra in Figure (6.6) which contain reduced wave numbers up to 0.5 or wave lengths down to $.08\,m$.

We seek the attenuation of infinitesimal kinematic waves as a function of the reduced wave number. This is readily obtained from the coherence $\gamma(N)$

which is defined as

$$\gamma(N) = \frac{\left|S_{\tilde{V}_1\tilde{V}_2}\right|}{S_{\tilde{V}_1\tilde{V}_1}}. \tag{6.11}$$

$\gamma(N)$ can only assume values between 0 and 1. Substituting for $S_{\tilde{V}_1\tilde{V}_2}$ from (6.7) we get

$$\gamma(N) = \varsigma(N). \tag{6.12}$$

The attenuation of the correlated signal is identically equal to the coherence of the fluctuating signals $\tilde{V}_1$ and $\tilde{V}_2$. Assuming that the attenuation is exponential in form, we write

$$\gamma(N) = e^{-k(N)T}, \tag{6.13}$$

where k is the attenuation time constant of infinitesimal kinematic waves. This form is valid for small fluctuations in the volume fraction signal, which is the case as long as the fluctuations are stable and die away, i.e. $k > 0$. Taking the natural logarithm of (6.13) yields

$$k(N) = -\frac{1}{T} ln\left[\gamma(N)\right]. \tag{6.14}$$

$k(N)$ is always positive since $\gamma(N)$ is always found to be less than 1, as expected since the flows considered here were all stable. Our assumption is thus justified.

The coherence as a function of wave number was obtained from the recordings of IVFM voltage fluctuations on the signal processor. Amplitude resolution of the coherence was enhanced by chosing a relatively broad filter band width (band width: $\Delta n < .0015$) in the frequency domain computation, but narrow enough not to "flatten out" meaningful coherence fluctuations. The coherence displays a "global" maximum at the least stable wave number which can be seen in Figure (6.6) for air-water flows and Figure (6.8) for solid-liquid flows. The attenuation time constant was then deduced using (6.14) and is shown in Figures (6.7) and (6.9)) in reduced form against reduced wave number for bubbles and

solids respectively. The reduced attenuation time constant and wave number are defined as

$$\kappa = \frac{kD}{V_0}, \quad n = ND. \tag{6.15}$$

where D is the disperse medium diameter and V_0 is its terminal velocity relative to the continuous medium at zero volume fraction.

6.5 Error analysis.

For all volume fraction of both bubbly and particulate flows, the coherence exhibits a peak which corresponds to the least stable wave number. All experimental coherence traces contain some error about the unknown "true value". This exhibits itself as parasitic non-repeatable fluctuations in the coherence obtained value. This error is proportional to the root of the reciprocal of the length of the record used. Intuitively, the ideal record length should be very large. Unfortunately, there often are record length constraints in experimental situations. This is the case with the batch type particle flows studied due to the finite volume of particulate material available for each run. The larger the total flow rate or the solids volume fraction, the shorter the duration of the flow. The shortest flow duration was of one minute for solids flows, and twenty minutes for bubbly flows. The error in coherence is largest in large flow rate, high volume fraction particle flows. However, if the coherence is large then the relative size of the error is decreased. Fortunately, large coherences were obtained for large volume fraction bubbly and solids flows. We are most interested in the values of the time constant corresponding to the peak in coherence, therefore, the least significant data obtained (low coherence away from the peak) is of little interest to us. The error in the time constant which is algebraically derived from the coherence is

$$\frac{\epsilon\{k\}}{k} = \frac{\epsilon\{\gamma\}}{\gamma ln(\gamma)} + \frac{\epsilon\{T\}}{T}. \tag{6.16}$$

Typical values of the error terms are :

$$\epsilon\{\gamma\} = .1, \tag{6.17}$$

and

$$\frac{\epsilon\{T\}}{T} = .2\,. \tag{6.18}$$

Using the above, we obtain the error in the time constant is

$$\frac{\epsilon\{k\}}{k}\Big|_{\gamma=.25} = .49, \tag{6.19}$$

$$\frac{\epsilon\{k\}}{k}\Big|_{\gamma=.5} = .49, \tag{6.20}$$

$$\frac{\epsilon\{k\}}{k}\Big|_{\gamma=.75} = .66. \tag{6.21}$$

The contribution to the error from inaccuracies in the delay time and coherence are of equal order of importance.

6.6 Results and discussion.

6.6.1 Transition from bubbly to churn-turbulent flows.

The coordinates of the minimum reduced attenuation time constant, κ and the corresponding n_{min} in Figures (6.7) and (6.9) were noted and plotted against air and solid volume fraction respectively. A sharp decrease in magnitude of the minimum attenuation constant was measured prior to the change in regime of the air-liquid flow. The minimum reduced attenuation constant κ is shown in Figure (6.10) versus air volume fraction for bubbly flows. At a volume fraction of 40%, κ decreases from a value of .03 to less than .003. This sudden fall in κ is accompanied by a shift in the least stable reduced wave number n_{min} from .07 to .03. These values correspond to kinematic perturbation wavelengths of .3m and .8m respectively. These are very large in relation to the pipe diameter which is .1016m. This result is shown in Figure (6.11). Upon further increase of the air flux the flow becomes churn turbulent.

Churn-turbulent flows consist of a broad size distribution of bubbles formed by the agglomeration of the original small bubbles. For this to happen, the surface tension forces which keep the spherical shape of the bubble must be overcome. At a volume fraction of 40%, the bubble-bubble forces must be sufficient to cause this break up. The natural extension of these experiments is to vary the size of the bubbles created, and to measure the volume fraction at which churn-turbulence onset occurs. The force required to overcome the surface tension of a bubble can be calculated (it is proportional to the ratio of the surface tension to the bubble diameter). We would thus obtain a measure of the bubble-bubble forces as a function of volume fraction (the onset volume fractions). Unfortunately, accurate control of the bubble diameter is a difficult practical problem, one that the author hopes will be tackled in the near future.

6.6.2 Solid-liquid flows.

For the solid-liquid flows, the minimum value of the reduced attenuation constant κ of each experiment is plotted against the solid volume fraction in Figure (6.12) for three groups of total flux. The points describe a curve which has a maximum at $\nu \approx 15\%$. The medium loses its structure faster at this volume fraction. The low volume fraction part of this curve is very different from the corresponding air-water results. However, the small number of low volume fraction air-liquid flows explored prevents us from drawing any conclusions on this matter. At higher volume fractions $> 15\%$, the attenuation constant κ for solid-liquid flows gradually decreases from a maximum of .025 to .0015 at $\nu = 55\%$. The monotonic decrease of the minimum attenuation constant for volume fractions $> 15\%$ differs from the sudden fall off experienced with the bubbly flows, and it seems to asymptote to a low value. As the extreme case consider a plug flow in which there is no relative motion between particles. For such a flow, the IVFM signals at the two monitoring locations would be identical

and the exhibit a time delay. Consequently, the attenuation constant would be zero for all wave numbers. The flows considered were not completely plug flows, however low values ($< .003$) of κ were obtained for flows 40% and above. Also, at high volume fractions, the attenuation constant is found to drop to lower values for all wave numbers. This explains the sharp increase in the wave number of lowest κ value displayed in Figure (6.13) for $\nu > 40\%$. n_{min} assumes values of $.04 \pm .02$ for solid fractions up to 40%. The corresponding most persistent wave length in the solid-liquid flows is .05m, which is approximately five times the pipe diameter. At higher volume fractions the closely packed medium preserves its structure over a broad band of wave lengths. The ability of the particles to withstand particle-particle forces allows the medium to maintain its structure at high volume fractions unlike the bubbly flows and no distinct change in flow regime takes place.

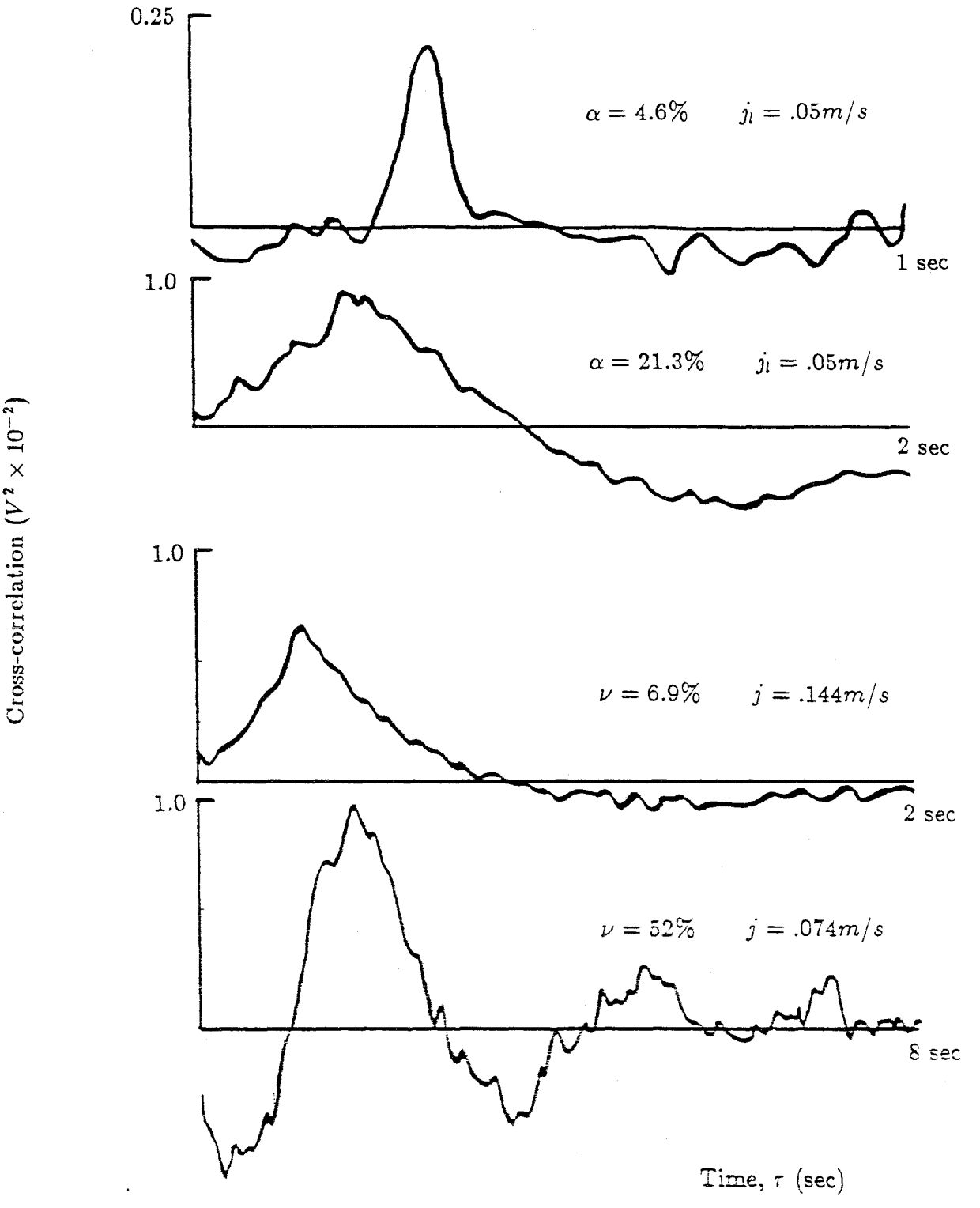

Figure (6.1) Typical cross-correlations of the IVFM output fluctuating voltage in bubbly and particulate flows.

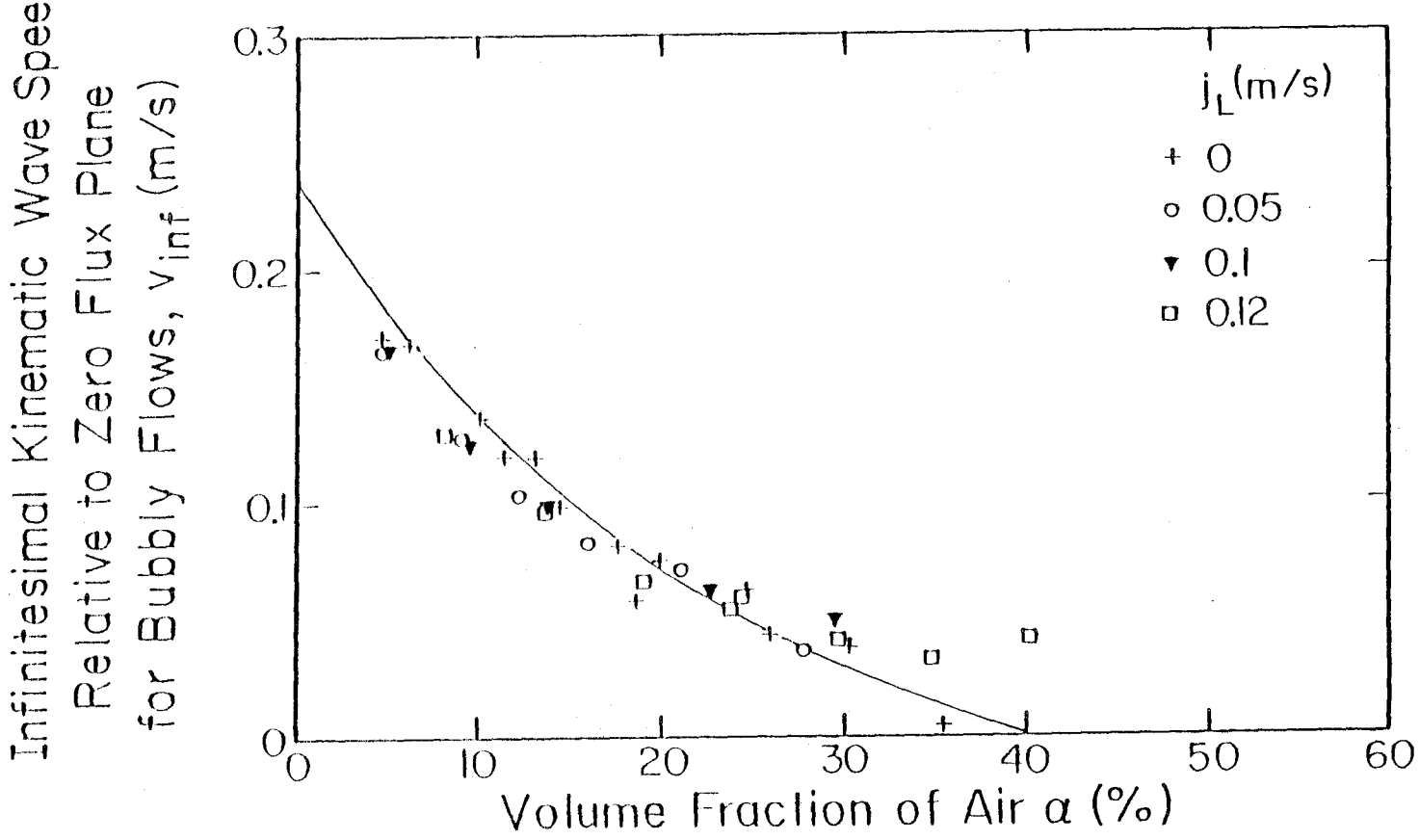

Figure (6.2) Infinitesimal kinematic wave speed values obtained by the cross-correlation technique for bubbly flows. The solid curve is the infinitesimal kinematic wave speed based on the Drift Flux Model and measurements of the air drift flux.

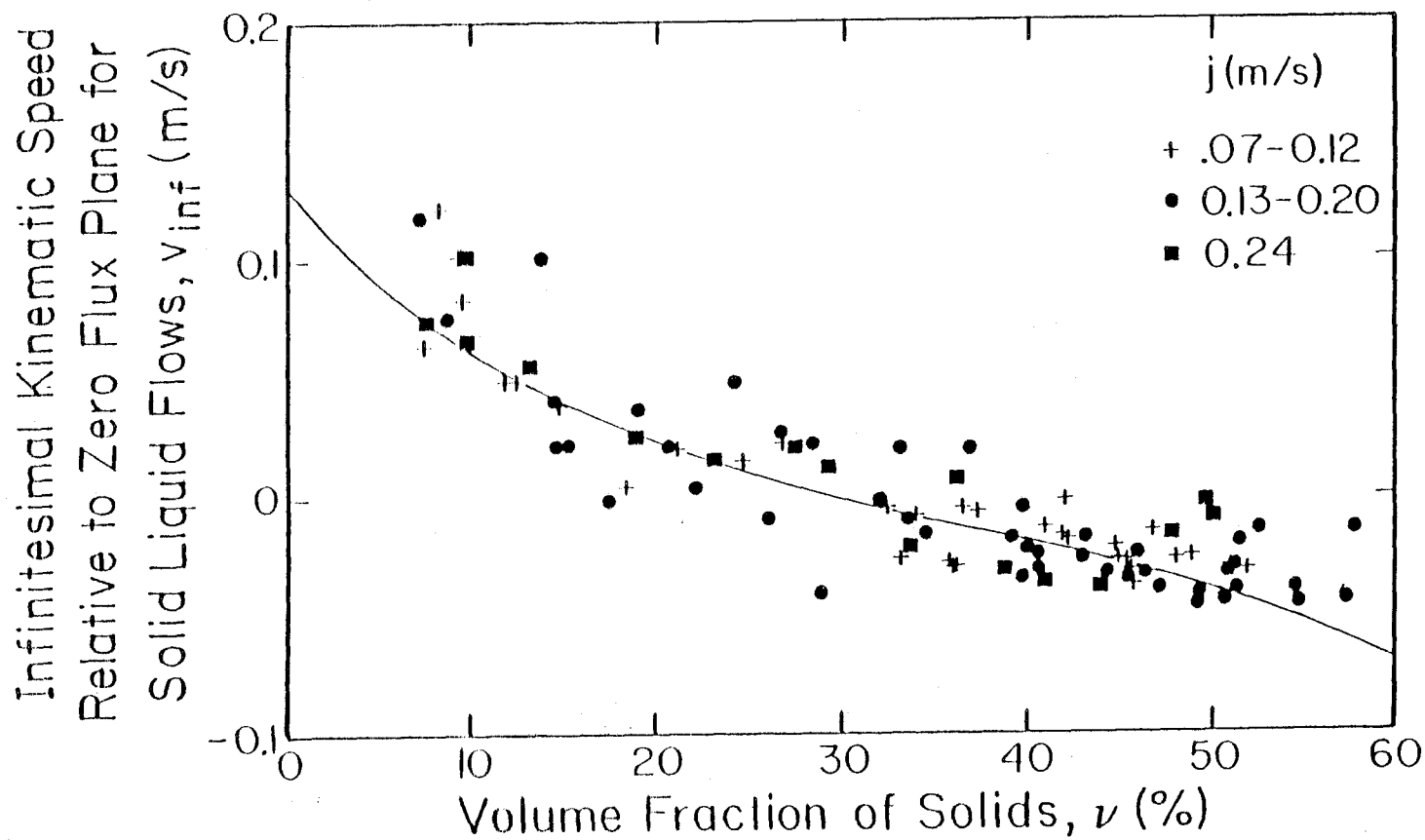

Figure (6.3) Infinitesimal kinematic wave speed values obtained by the cross-correlation technique for particulate flows. The solid curve is obtained using the Drift Flux Model and the drift flux curve determined in Chapter 7.

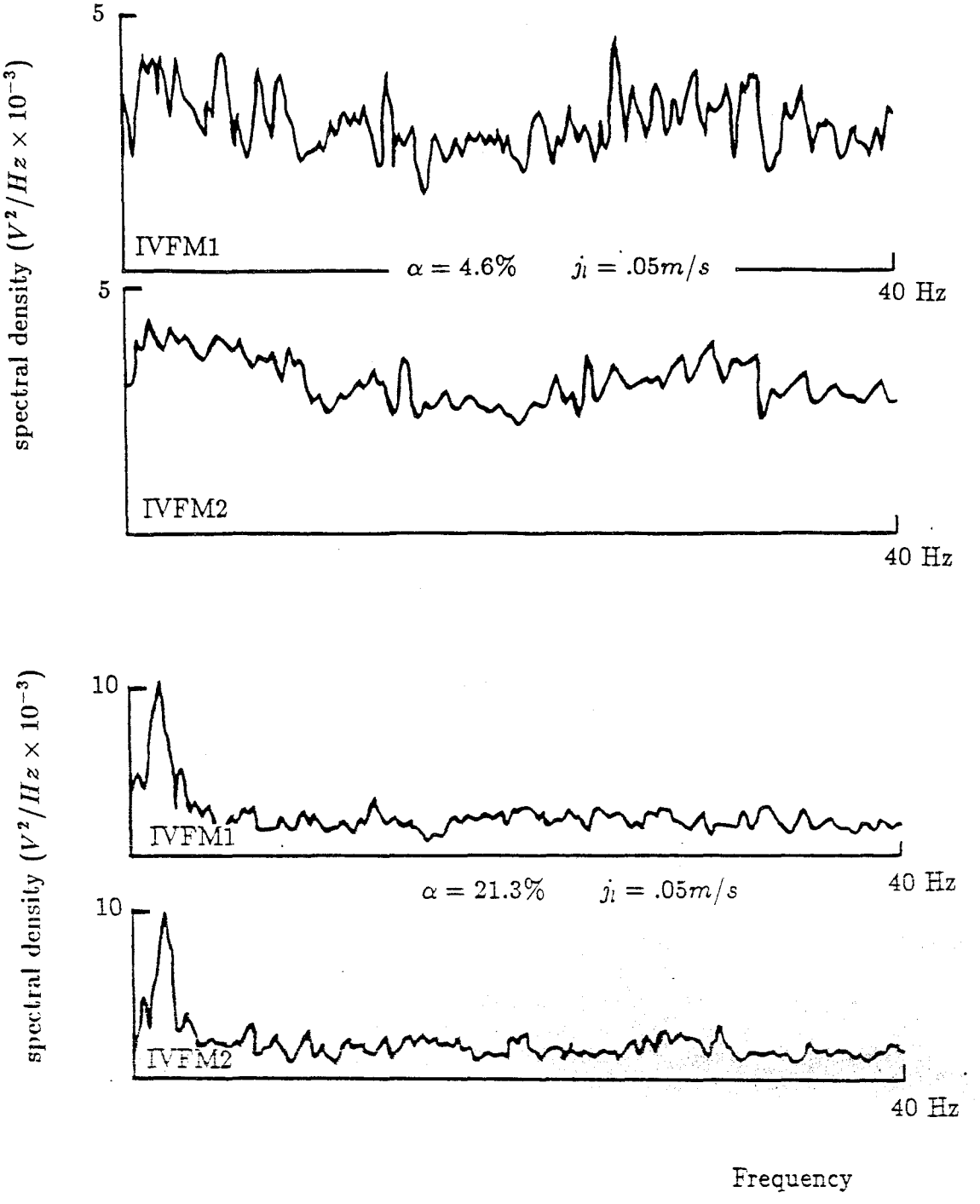

Figure (6.4) Power spectra of the IVFM output fluctuating voltage measured simultaneously at two locations separated by .0735 m, for bubbly flows.

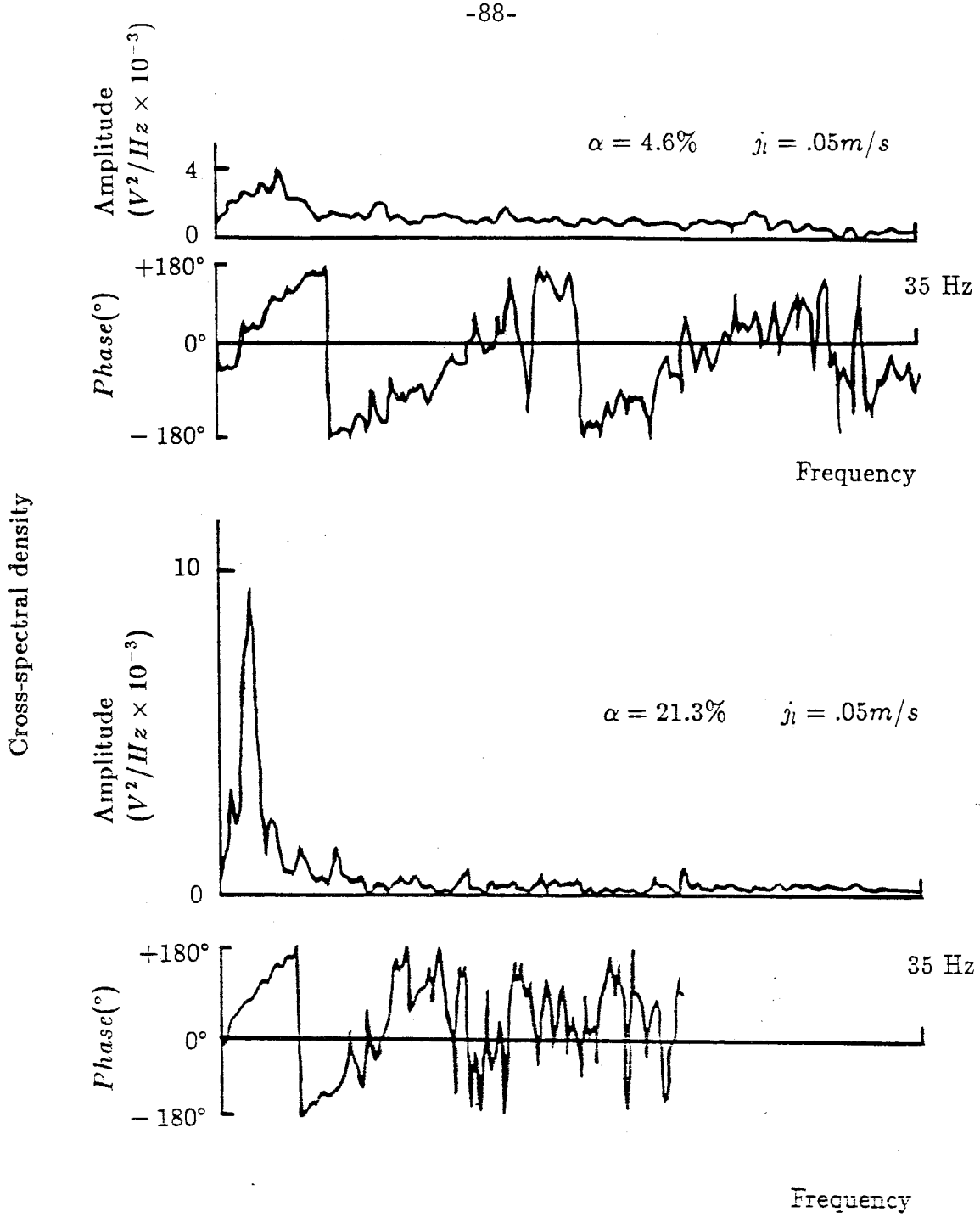

Figure (6.5) Cross-power spectrum of the IVFM output fluctuating voltage at two locations separated by .0735 m, for bubbly flow showing the linear relation between phase and wave number.

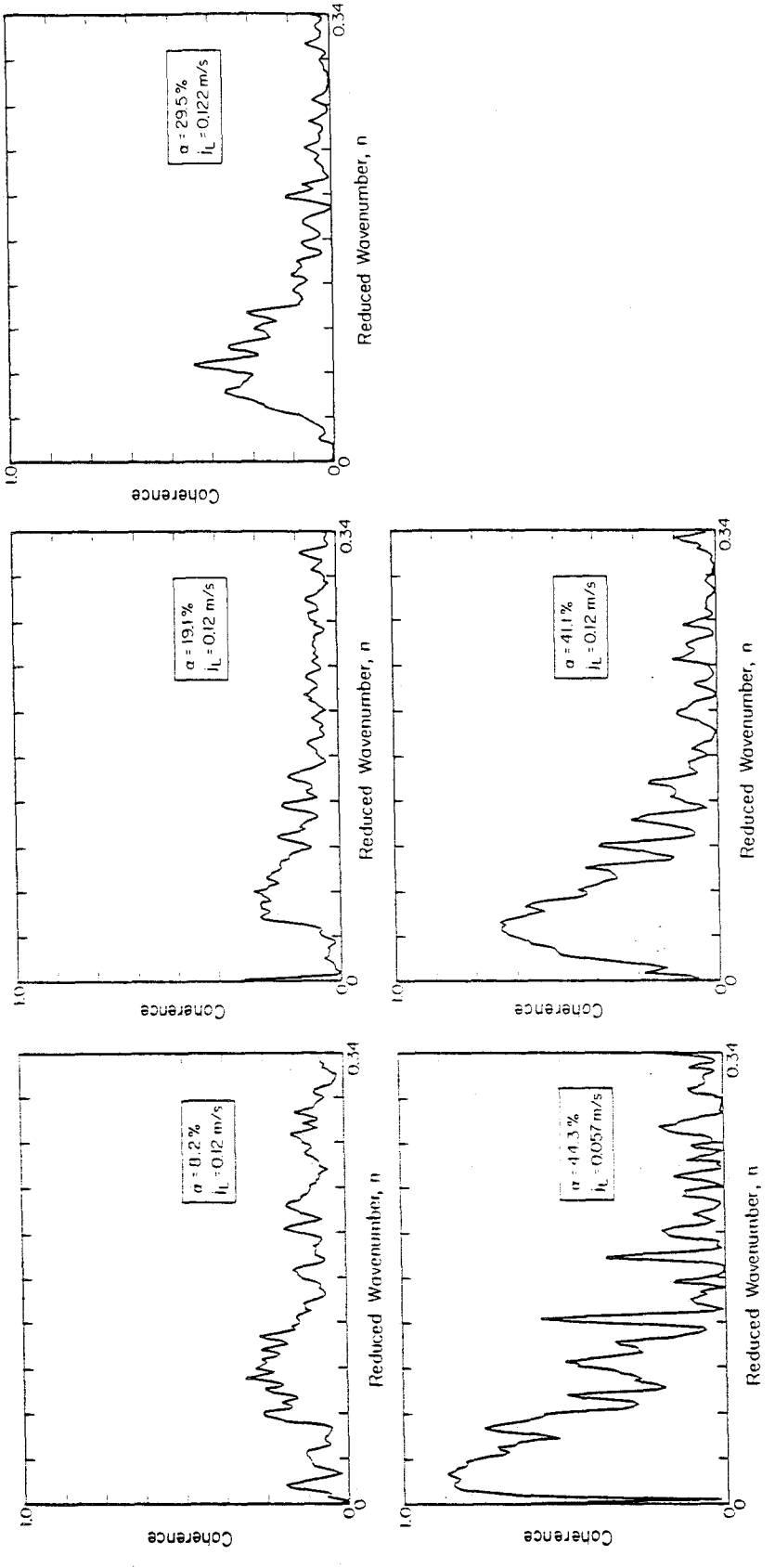

Figure (6.6) Coherence of the two IVFM fluctuating output signals (separation of IVFM's = .0735 m) in bubbly flows plotted against reduced wave number.

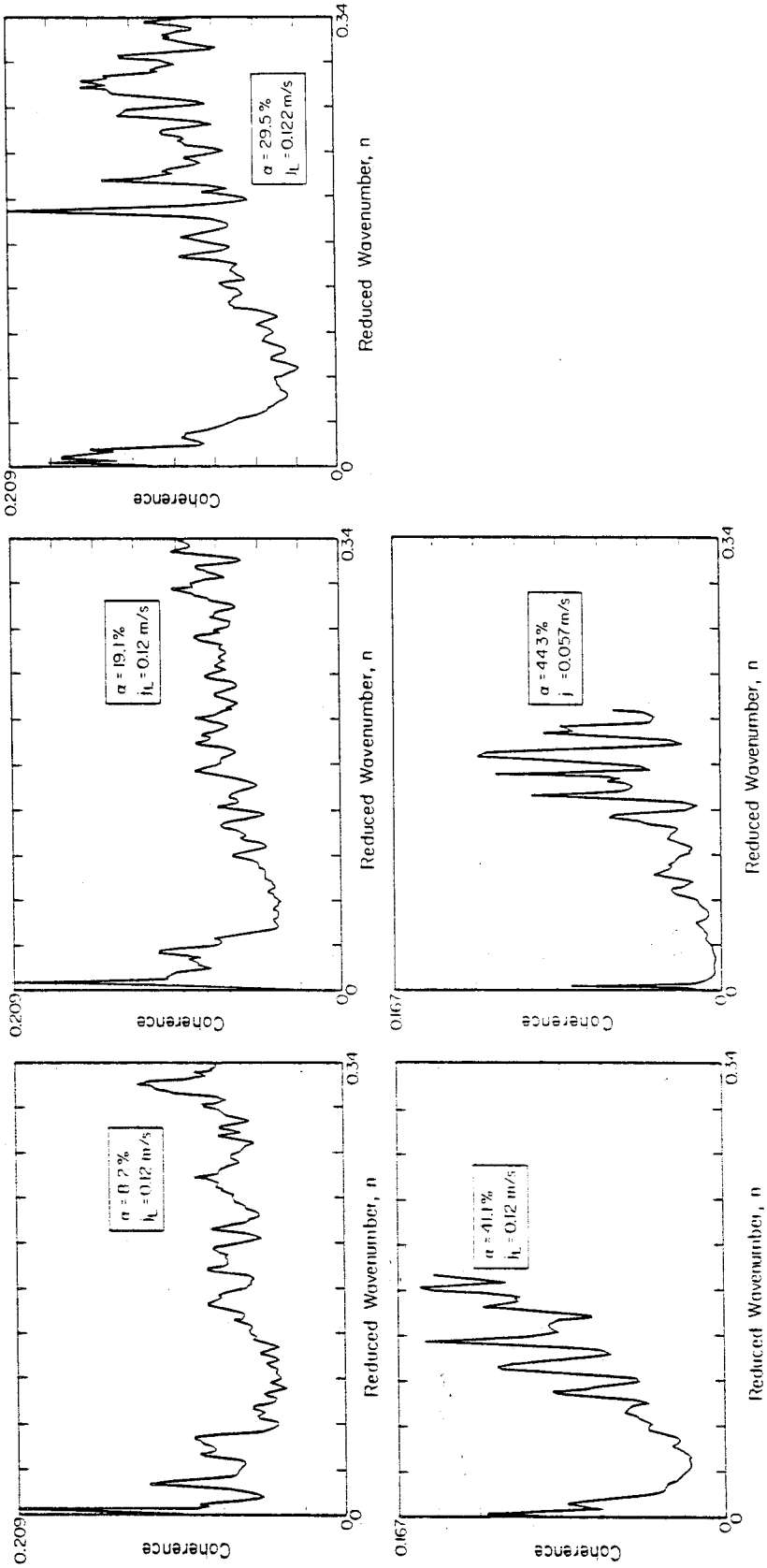

Figure (0.7) Reduced attenuation time constant calculated from the coherence for bubbly flows, showing a characteristic minimum representative of the least stable wave number. Note the decrease in the minimum value at high volume fraction ($\sim$ 40%) prior to the onset of churn turbulence.

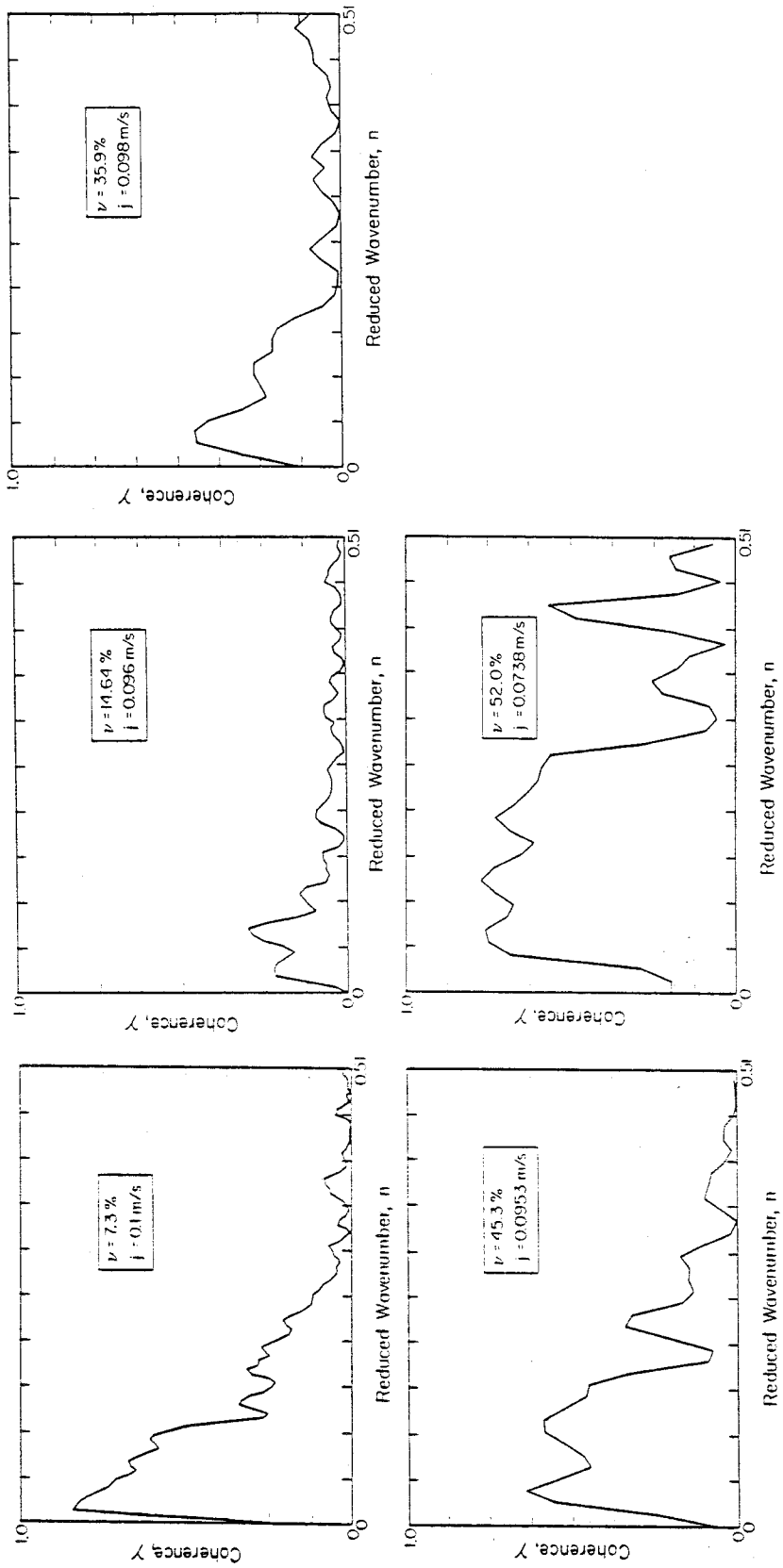

Figure (6.8) Coherence of the two IVFM fluctuating output signals (separation of IVFM's = .0735 m) in particulate flows.

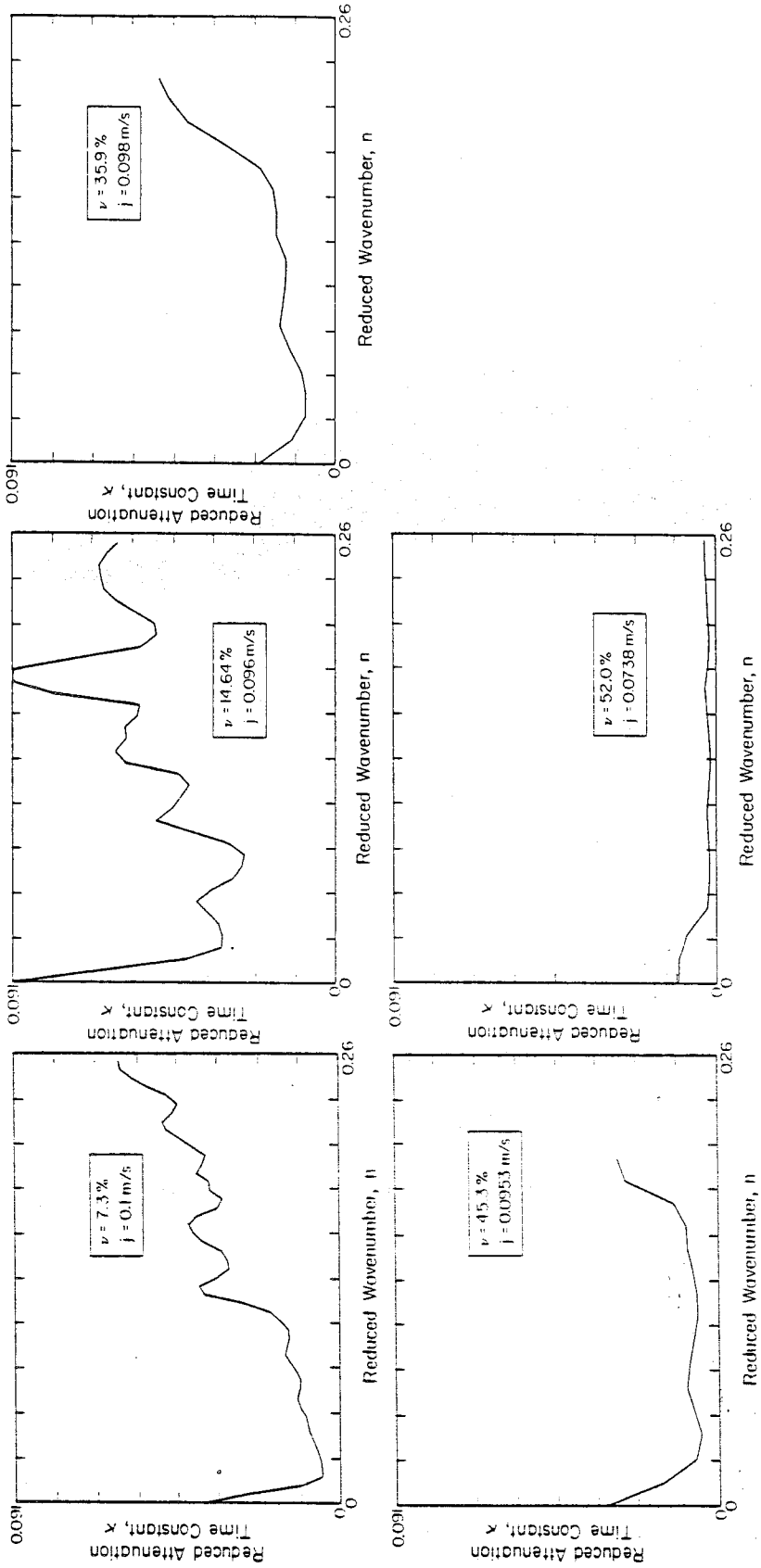

Figure (6.9) Reduced attenuation time constant calculated from the coherence for particulate flows, showing a characteristic minimum representative of the least stable wave number. Note the broad band decrease in the attenuation time constant at high volume fractions, indicative of the tendency of the medium to conserve its structure.

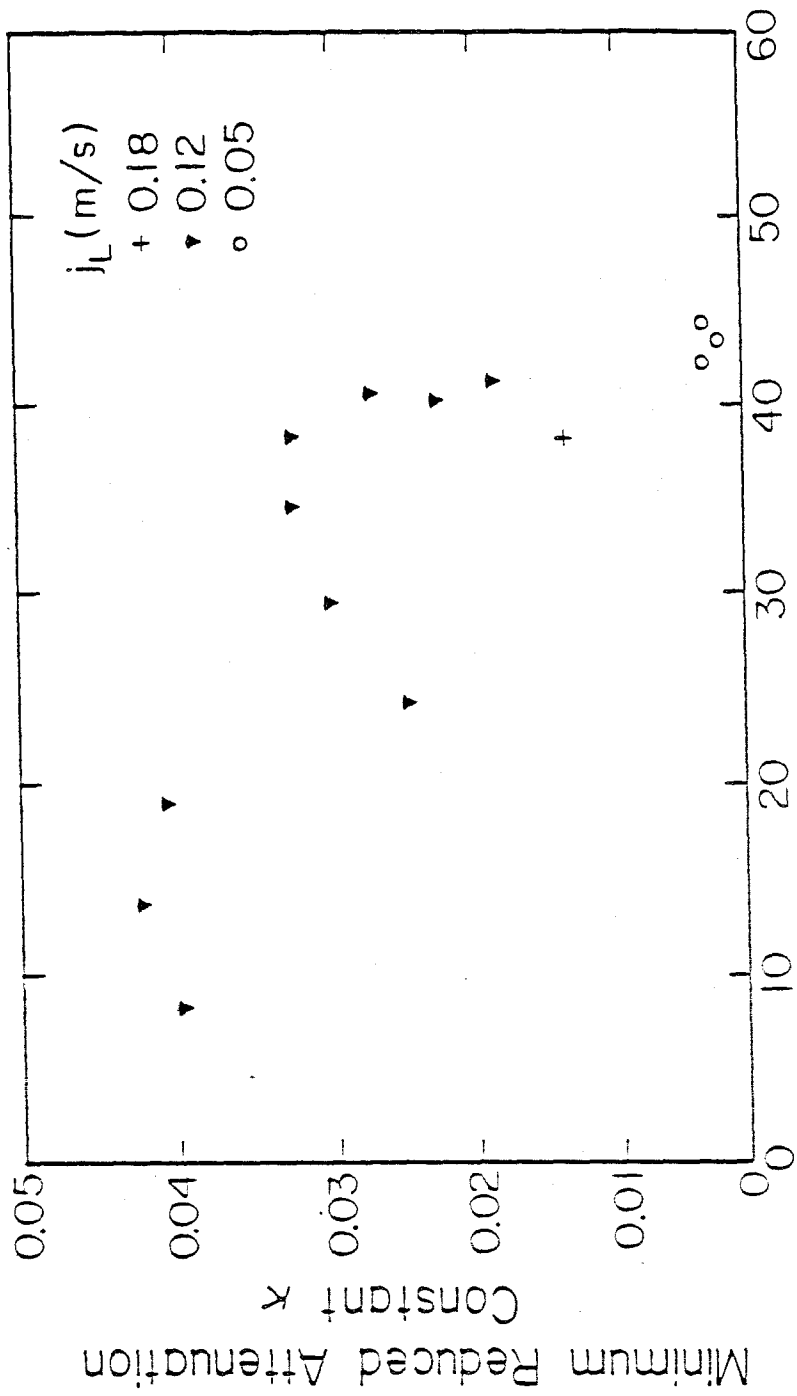

Figure (6.10) Minimum attenuation constant of bubbly flows of various volume fraction and flow rate conditions presented versus volume fraction. Note the sudden decrease in this variable at $\alpha = 40\%$ prior to the onset of churn-turbulence.

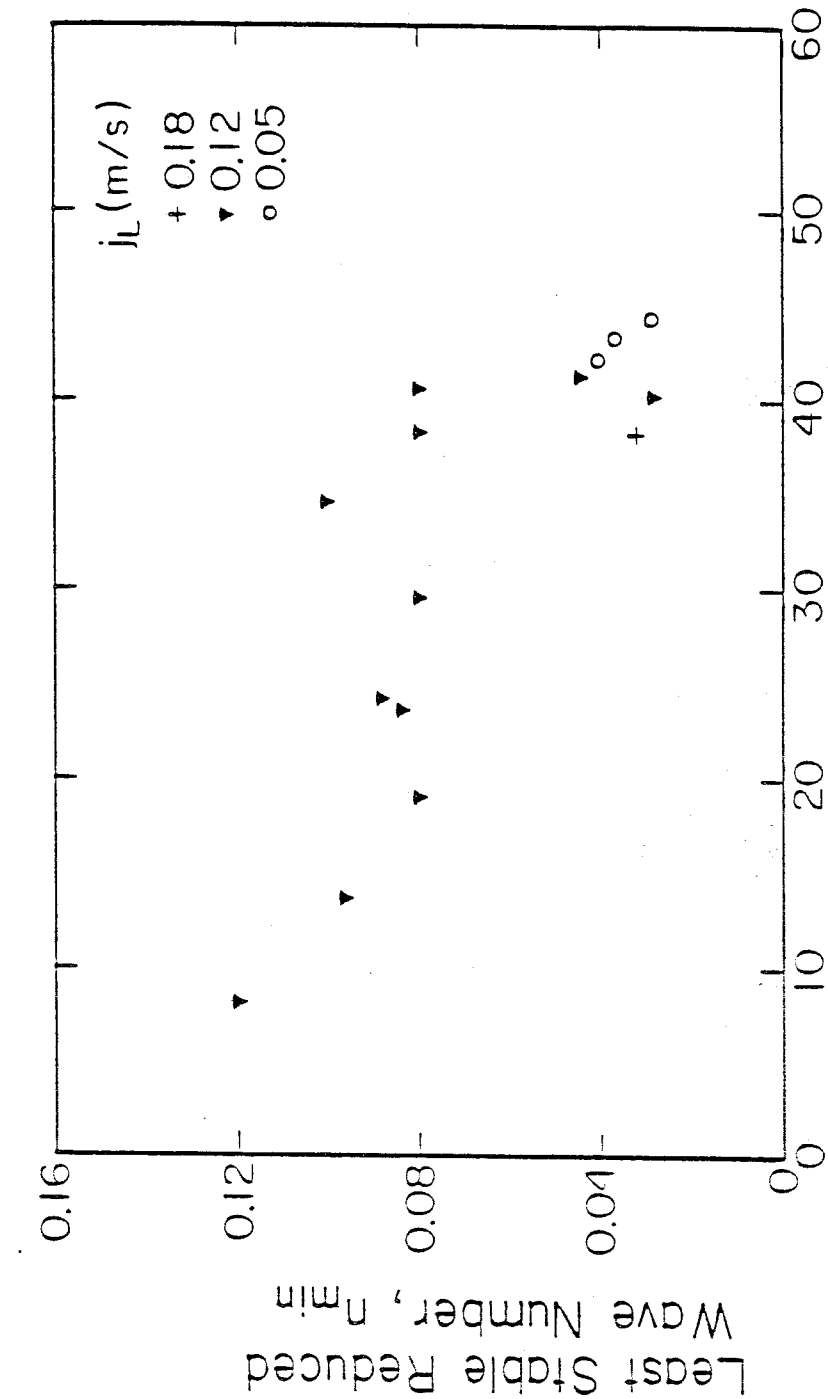

Figure (6.11) Most coherent wave number in bubbly flows of various volume fractions and flow rates.

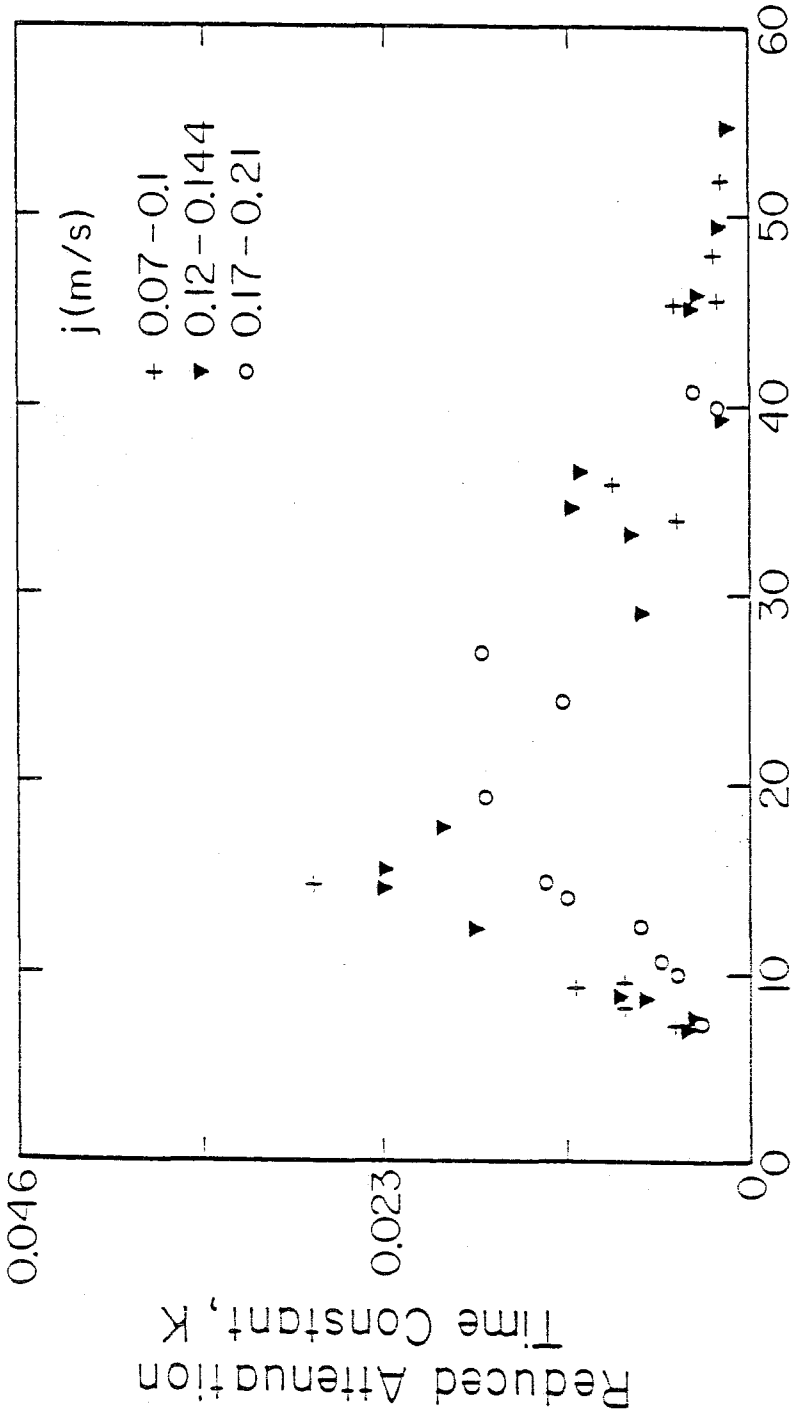

Figure (6.12) Minimum attenuation constant of particulate flows of various volume fractions and flow rates. The gradually decreasing attenuation constant displays the increased persistence of structure in the flow.

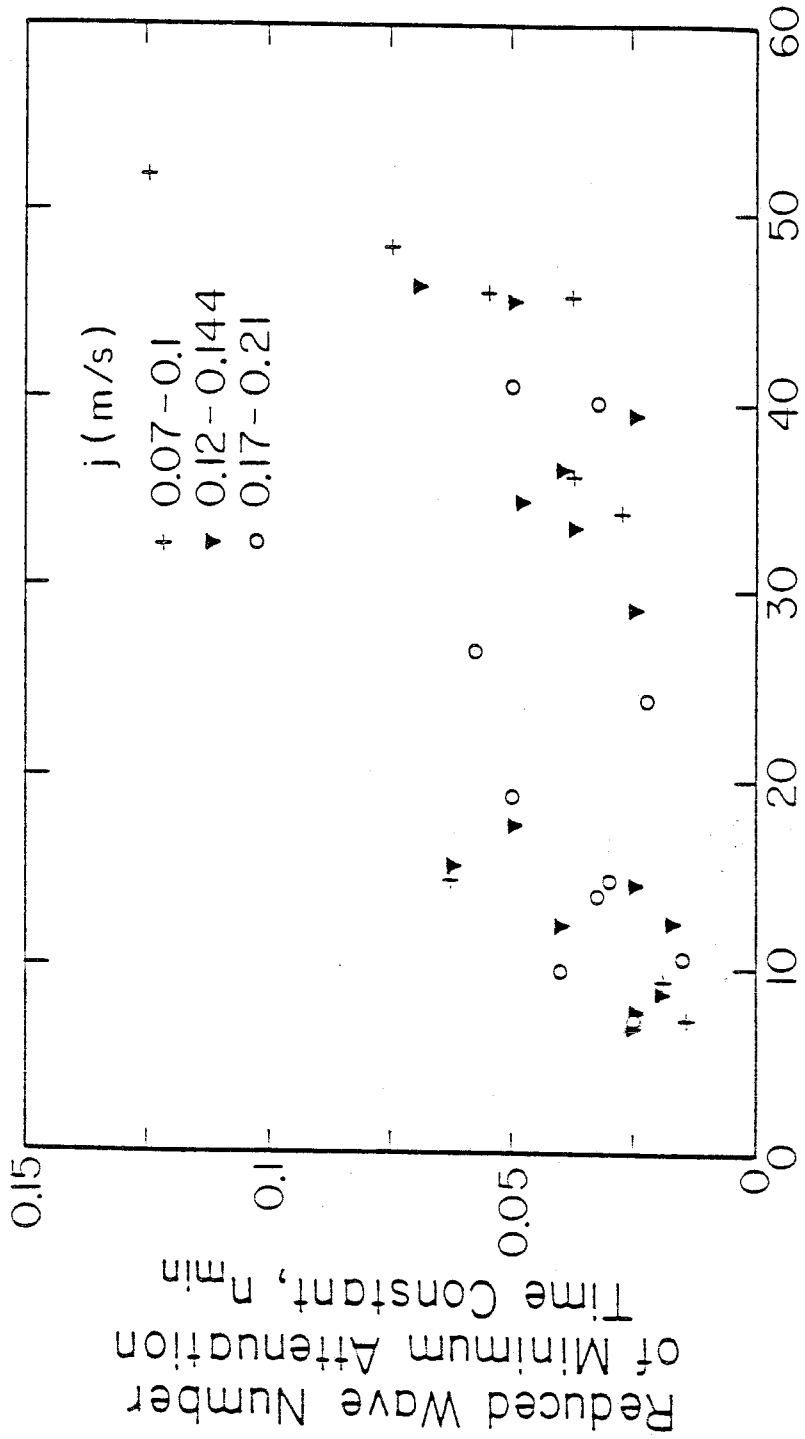

Figure (6.13) Most coherent wave number in particulate flows of various volume fractions and flow rates.

Chapter 7. MEASUREMENTS OF FINITE WAVES IN BUBBLY AND SOLID-LIQUID FLOWS.

7.1 Introduction.

The quasi-linear homogeneous continuity equation for a two-phase flow exhibits wave front steepening which leads to the formation of stable kinematic shocks (Wallis (1962)). The continuity equation based on the Drift Flux Model was shown to accurately predict the propagation velocity of the concentration discontinuities by Bernier (1981). In the present study similar experiments were carried out at low total flow rates to test the shielded electrode IVFM's and to verify the above result. The agreement between measured and predicted speeds proved to be very good. The Drift Flux Model assumes that the relative velocity between species is a function of volume fraction. In bubbly flows the average air-liquid relative velocity is directly determined by monitoring air mass flow rate and the volume fraction. However, direct measurement of the solid-liquid relative velocity is not possible with our present facility. The good agreement obtained for bubbly flow shocks led us to a simple method of determining the particle-water drift flux in terms of volume fraction from particle shock speed measurements at zero total flow rate. The drift flux function obtained was used to calculate infinitesimal wave speeds in solid-liquid flows for comparison with speeds obtained using the cross-correlation technique in Chapter 6.

In downward flows of large initial solid particle volume fractions ($> 50\%$) and total flux between .1 and .4 m/s the obstruction caused by the air injector tube array causes a finite amplitude kinematic wave to travel up the test section below which the medium behaves as a solid and above which the medium is fluidized. Solidification shocks of this form are also encountered in batch sedimentation (Kynch (1952), Smith (1966), Wallis (1969)) and in the solidification of liquefied saturated sands (Scott (1986), Gibson (1958), Terzaghi (1943)).

The consolidation or compaction process of the solidified portion was observed to exhibit relaxation under its own increasing weight and the downward body like force from the liquid flowing through the packed solids. The occurrence of solidification waves caused by obstructions in the pipe flow is not only particular to vertical flows; it is argued that such waves can exist in horizontal and inclined flows also. The force imparted by the packed column on the obstruction is found to be very large and potentially destructive.

7.2 Kinematic Shock Velocity in Bubbly Flows.

In this section we study the propagation speed of stable concentration or kinematic shocks in bubbly flows. Experimental measurements were made and compared to predictions based on the Drift Flux Model.

The continuity equation for the disperse component can be written in the form of a quasi-linear homogeneous first order partial differential equation assuming that inertial terms are negligible.

$$\frac{\partial \nu}{\partial t} + C_i(\nu)\frac{\partial \nu}{\partial y} = 0. \tag{7.1}$$

The derivation of (7.1) which is based on the Drift Flux Model is outlined in detail in Chapter 5. Due to the dependence of C_i on ν, the solution to the initial value problem with this type of equation displays wave front steepening that can lead to the formation of a kinematic shock which is best described as a propagating step in volume fraction. In general, as with infinitesimal kinematic waves, the propagation speed of such a shock differs from the speed of either constituent. Under the action of gravity, shocks are found to be stable only when the bulk density is lower above the step than below it. This is a direct consequence of the monotonically decreasing trend of the relative velocity as a function of volume fraction. The reverse situation is unstable and was observed to display finger-like flow patterns characteristic of the Rayleigh-Taylor instability. In this section, we only concern ourselves with the propagation of stable

shocks. The shock speed is calculated by ensuring continuity of both species across the shock, and was shown in Chapter 5 to be

$$V_S = j + \left\{ \frac{j_{dj_2} - j_{dj_1}}{\nu_2 - \nu_1} \right\}. \tag{7.2}$$

where j is the total flux, j_{dj} is the drift flux and subscripts $_1$ and $_2$ represent upstream and downstream conditions respectively.

The Drift Flux Model was shown to accurately predict shock speeds in bubbly flows at zero liquid velocities by Bernier (1981). We verified this result using two shielded IVFM's separated by a distance of .0735 m for bubbly flows. The drift flux was measured for different volume fractions steady flows and the fourth order least squares fit to this data was calculated. The data and the resulting curve are shown in Figure (7.1). This curve was then used to predict bubbly shock velocities for comparison with experimental measurements. Shocks were created by suddenly turning off one of two parallel air flow valves supplying the air manifold. The output of the two IVFM's was displayed on a strip chart recorder and the time lag in the drop in volume fraction caused by the passage of the shock by each IVFM was directly read off the chart. Figure (7.2) shows the experimentally obtained shock velocities (relative to the zero flow rate plane) as individual points. These fall close to the Drift Flux predictions which are shown as lines of constant upstream volume fraction (the lower value of the two). The good agreement between the measurements and the Drift Flux Model results suggests that if the Drift Flux curve were not known but shock velocities could be measured, these could be used to deduce the former.

7.3 Particle Drift Flux from Measured Kinematic Shock Velocities.

The Drift Flux Model proved to be accurate in both predicting infinitesimal and finite kinematic wave speeds for bubbly flows. With no direct means of determining or measuring the average Drift Flux between the solids and the

liquid, we turn to kinematic shock speed measurements in solid-liquid flows to indirectly derive the Drift Flux as a function of solid fraction.

7.3.1 Experimental Technique.

Particle kinematic shocks were created by suddenly throttling down the solids species flow rate by altering the position of the particle flow control gate. This was done manually; the technique was perfected after much practice. This method was successful for kinematic waves which propagate downward. However, in the case of upward propagating finite kinematic waves, which occur at large volume fractions, the effect of throttling at the top of the test section is never seen downstream. This difficulty was overcome by imposing a net downward flow to force the created shock to travel downward. The downward flow is then turned off just after the shock passes the lower IVFM, to be recaptured as it travels back up past the two IVFM's. For each created and monitored kinematic shock, the upstream and downstream volume fractions and the shock speed were recorded. The results of measured shock speeds which are a function of two independent variables are shown in the following section against shock speed values based on the drift flux function of best fit .

7.3.2 Least Squares Fit of Drift Flux Model to Shock Speeds.

As shown in Chapter 5, the velocity of a kinematic shock relative to the zero net flow plane is a function of both the upstream and the downstream volume fractions and is given by

$$V_s = V_s(\nu_1, \nu_2) = \frac{j_{dj}(\nu_2) - j_{dj}(\nu_1)}{\nu_2 - \nu_1}. \tag{7.1}$$

j_{dj} is the drift flux at the volume fraction denoted by the argument. The subscripts $_1$ and $_2$ denote upstream and downstream conditions respectively. We assume the drift flux to be a fourth order function in ν, the volume fraction, with four undetermined coefficients.

$$j_{dj}(\nu) = K\nu + L\nu^2 + M\nu^3 + N\nu^4. \tag{7.2}$$

The "error" ϵ in the measured kinematic shock speed which is taken to be the difference between the measured and the predicted wave speed based on the two volume fractions, multiplied by the shock strength for convenience is

$$\epsilon = (\nu_2 - \nu_1)V_s - (j_{dj}(\nu_2) - j_{dj}(\nu_1)) . \tag{7.3}$$

A measure of the total error of our fit is the sum of the squares of the error over all points measured. For the best fit, we want this to be a minimum with respect to each undetermined coefficient. We impose this condition by setting the derivative of the sum of the squares of ϵ with respect to each of the four undetermined coefficients to zero. This results in a matrix equation of the form

$$[A]\{x\} = \{b\}, \tag{7.4}$$

where $\{x\}$ is the vector of undetermined coefficients

$$\{x\} = \begin{pmatrix} K \\ L \\ M \\ N \end{pmatrix}, \tag{7.5}$$

$\{b\}$ is the vector

$$\{b\} = \begin{pmatrix} \Sigma[(\nu_2 - \nu_1)(\nu_2 - \nu_1)v_s] \\ \Sigma[(\nu_2 - \nu_1)(\nu_2^2 - \nu_1^2)v_s] \\ \Sigma[(\nu_2 - \nu_1)(\nu_2^3 - \nu_1^3)v_s] \\ \Sigma[(\nu_2 - \nu_1)(\nu_2^4 - \nu_1^4)v_s] \end{pmatrix} . \tag{7.6}$$

Σ denotes summation over all the experimental points. The j'th term in the i'th row of the symmetric four by four matrix $[A]$ is

$$a_{ij} = \Sigma[(\nu_2^i - \nu_1^i)(\nu_2^j - \nu_1^j)]. \tag{7.7}$$

Equation (7.4) is solved by inverting $[A]$. Sixty four shock speed measurements were made, for which the best fitting drift flux function was found to be

$$j_{dj} = .1317\nu - .412\nu^2 + .571\nu^3 - .376\nu^4. \tag{7.8}$$

The correlation coefficient between the measured and the expected shock velocities serves as an indicator of the quality of the fit. This is defined as

$$r = \frac{R_{me}}{\sqrt{R_{mm}R_{ee}}}, \tag{7.9}$$

where R_{me} is the cross-correlation and R_{mm} and R_{ee} are the auto-correlations of the measured and expected shock velocities respectively. The measured shock velocities are plotted against the corresponding expected values in Figure (7.3). A correlation coefficient of .993 demonstrates that the assumed model satisfactorily describes kinematic shock speeds for solid-liquid flows of low total flow rate. The drift flux curve is shown in Figure (7.4) with values of drift flux determined from shocks of zero upstream volume fraction to indicate the degree of scatter.

7.4 Solidification Shocks in Solid-Liquid Flows.

It was found that when creating a high concentration flow ($\nu \sim 50\%$) with a downward net flowrate ($.1 < j < .4\, m/s$), a compression shock was initiated at the array of tubes at the very bottom of the test section when the initial particle rich front reached it, while still maintaining a net downward flow of particles through the array of tubes. This type of behavior is analogous to the "backing up" of a traffic jam caused by some obstruction on the road.

The array of brass tubes in the pipe section acts as the obstruction in our case. This shock which travelled up the test section (against the direction of flow) at speeds much larger than previously observed shocks (up to $.5\, m/s$) relative to the zero flux plane compared with $.03\, m/s$ for the fastest previous upward moving shock) was found to be a "solidification wave" with the medium

being fluidized above the shock and solidified below. Solidified is used in the sense that the disperse species is able to sustain (compressive) stresses.

In batch sedimentation, the interface of settled material also propagates up as a continuity shock (Kynch (1952)). This same phenomenon also occurs in post liquefaction solidification of water-saturated sands (Scott (1986)), where liquefaction of the soil can be caused by the violent shaking inherent to earthquakes. This phenomenon of sand liquefaction can be destructive, and cause large earth masses to flow.

The solidified column formed in our experiments is supported by the grid unlike the fluidized case in which the particles are supported by the liquid. The downward liquid flow relative to the packed bed imparts a body type force on the solids which dramatically increases the total force on the grid, to the point of being potentially destructive. This phenomenon can be induced just as readily in horizontal two-component flow by any form of obstruction to the flow of the disperse species and may lead to failure of the obstruction.

7.4.1 Experimental Technique.

The solidification waves were created not by throttling the feed of particles into the test section, but by the naturally occurring process of compaction caused by the obstruction presented to the high volume fraction particle flow by the array of 21 1/8" (3.2 mm) OD brass tubes. The tubes lay inside the 4" (101.6 mm) pipe across the flow in horizontal groups of three, with a vertical separation of 1" (25.4 mm) and an angle of rotation of 30° between groups.

The liquid static pressure difference was monitored between two points separated by .776 m with the lower pressure tapping located .2 m above the tube array. The two IVFM's were set 73.5 mm apart while the distance between the upper pressure tapping and the lower IVFM was 42.5 mm. The total flow rate was continuously monitored during experiments with an electromagnetic flow

meter located in the pure water part of the loop. Figure (7.5) shows the instrumented test section. The instrument outputs were recorded simultaneously in real time for each experiment on a multi-channel cathode ray tube strip chart recorder to avoid inaccuracies caused by pen inertia.

The total flow rate was kept constant for each experimental run. After initiation by opening the particle flow control gate to deliver the desired particle volume fraction, the test section becomes filled with a fluidized high volume fraction solid-liquid mixture. The solidification wave forms as the particle rich front reaches the tube array. The upward travelling wave is first detected as it passes the lower pressure tapping which causes a decrease and subsequent sign reversal in the differential pressure as the wave resides between the tappings and passes them. No time discontinuity is observed in the rate of change of the differential pressure as the wave passes the upper pressure tapping. Moreover, the pressure trace displays marked relaxation before reaching a steady value. This occurs shortly after the wave has passed the IVFM's, but before the wave reaches the mouth of the hopper, and above all before running out of particles. The identification of the last two criteria is important for critical interpretation of the results. Finally the hopper runs out, and as the end shock travels down it is detected at all four monitoring locations. The differential pressure and volume fraction traces are shown in Figure (7.6) for a total volume flux of $1.5\,m/s$.

7.4.2 Solidification Shock Velocity.

The solidification waves travel upward in a net downward flow at speeds much larger than the kinematic shocks in a fluidized medium. By continuity, Equation (7.2) still holds for the solidification wave speed, with a correction to the downstream (solidified medium) drift flux which is no longer given by the drift flux function derived in Section (7.3). In the fluidized case the solids flow down relative to the liquid whereas the situation is reversed in the moving

packed bed flow. The downstream drift flux is determined from the known total flux, the particle velocity which is directly obtained from the speed of the end-of-batch-shock and the measured volume fraction. The packed bed drift flux is given by

$$j_{dj}|_{packedbed} = \nu(v_p - j). \tag{7.10}$$

The values of drift flux thus derived are shown on Figure (7.7) with the drift flux curve obtained in Section (7.3) for comparison. The packed bed values of drift flux are large and of the opposite sign compared with the fluidized counterpart. The known upstream and downstream drift fluxes were then substituted into (7.2) to determine the shock speed according to continuity. The results are plotted against the measured solidification shock speeds in Figure (7.8). These fall on a the same line with little scatter. The correlation coefficient of the linear best fit is .996 with a slope of one and zero intercept.

7.4.3 Choking of Particle Flow.

The change in flow regime from the fluidized state to solidified plug flow has a dramatic effect on the flow rate of the particulate material. This is caused by the force imposed by the tube array on the disperse medium and it oppposes the flow of particles. We plot the particle flux versus volume fraction in Figure (7.9) to demonstrate the choking of the solids flow. The solid lines are for fluidized flows which can exist up to concentrations as large as 60% as long as there are no obstructions in the flow. The points shown are the results of our experimental measurements of solid flux under the choked condition.

7.4.4 Forces on the Obstruction.

The force oppposing the particle flow supplied by the tube array required to sustain the solidified or choked flows consists of two body forces, namely the buoyant weight of the solidified column and the force imparted on the packed bed by the downward flowing liquid. The latter can be determined indirectly

from the measured friction pressure drop in the packed bed. The packed bed friction factor f and Reynolds number Re are defined by

$$f = \frac{\Delta p}{1/2\rho_l(v_l - v_s)^2}\frac{D_{particle}}{L}. \tag{7.11}$$

$$Re = \frac{|v_l - v_s|D_{particle}\,\mu_l}{\rho_l}. \tag{7.12}$$

The friction factor is shown in Figure (7.10) against the Reynolds number. The force caused by this friction pressure drop was calculated and compared to the weight of the solid column. The ratio of friction forces to the weight for equal height packed beds is shown in Figure (7.11). At a Reynolds number of 100, the frictional forces and the bed weight are of the same order of magnitude. At higher relative velocities the frictional forces dominate and are up to ten times the weight at a Reynolds number of 500. A plot of ratio of the two forces indicates that the frictional forces dominate for most of the experiments carried out. Therefore, the force generating mechanism on an obstruction can also exist in a horizontal flow. At the slow relative velocities considered (up to $.16\,m/s$) body forces of up to $30\,KN/m^3$ were generated. For a bed height of $2\,m$ and a cross-sectional area of $.081\,m^2$, the corresponding force is $\sim 500\,N$, the weight of an average man. Very large forces can be generated by obstructions that cause solidification, which can lead to the ultimate failure of the obstruction.

7.5 Consolidation of moving packed bed.

In the described experiments, after the solidification shock has passed the upper pressure tapping such that the liquid pressure gradient in a moving packed bed is now monitored, the pressure gradient is found to increase further until a steady value is reached. A typical pressure transducer trace is shown in Figure (7.6). This gradual change in the pressure gradient is indicative of relaxation in the compaction process of the packed bed under its own weight and the forces imparted by the fluid flowing through it. This phenomenon has been identified

in batch sedimentation (Wallis (1969)) and soil solidification (Scott (1986)). Our case differs from these in the total flowrate. The batch sedimentation process typically takes place at zero net flowrate, with an almost zero relative flowrate between species in the solidified column. In our experiments on the propagation of solidification waves, both the total flowrate and the slip velocity between components are non-zero. The typical relaxation time for the measured pressure difference to reach the mean value of the starting and finishing states was of the order of 10 seconds. The corresponding characteristic relaxation zone thickness was evaluated as the ratio of the half-life of the pressure signal to the solidification wave velocity. Little scatter was found in the results and the relaxation zone thickness measured to be .57m $\pm$ .05m; this thickness was found to be relatively independent of the shock velocity over the range of solidification shock velocities covered (.058-.093 m/s).

7.6 Conclusion.

The Drift Flux Model is found to accurately predict the finite kinematic shock velocities in bubbly air-water flows. This good agreement was used to derive indirectly the Drift Flux curve for solid-liquid flows by carrying out solid-liquid kinematic shock speed measurements and extracting the Drift Flux function from the results. A non-linear regression scheme with two independent variables was used to derive the unknown parameters in the assumed form for the Drift Flux function. A regression coefficient of .993 indicates the validity of the assumed model. The result of this analysis is used to calculate infinitesimal wave speeds in solid-liquid flows for comparison with speeds obtained experimentally using the cross-correlation techniqued in Chapter 6.

In downward flows of large initial solid particle volume fraction ($> 50\%$) and total flux between .1 and .4 m/s, the obstruction in the form of the air-injector at the bottom of the test section is found to cause a finite amplitude

kinematic wave to travel up the test section. The wave is unlike the others studied in that the medium is fluidized above it and in the form of a packed bed below. The solidification wave propagation speed is found to conform with the Drift Flux Model predictions, based on the drift flux of liquid flow through the packed bed. The packed bed has the property of transmitting (compressive stresses) from particle to particle, unlike the fluidized state in which the fluid entirely supports each particle. The forces generated on the obstruction by the process of solidification were shown to be very high and potentially destructive. This force originates predominantly from the body force the liquid imparts on the flowing packed bed. This phenomenon can therefore occur in horizontal flows of high concentration slurries just as readily in the presence of an obstruction. The process of solidification combined with the corrosive environment in a large volume fraction solid-liquid medium reduces the life expectancy of slurry handling equipment. Clearly obstructions of this type of flow should be avoided.

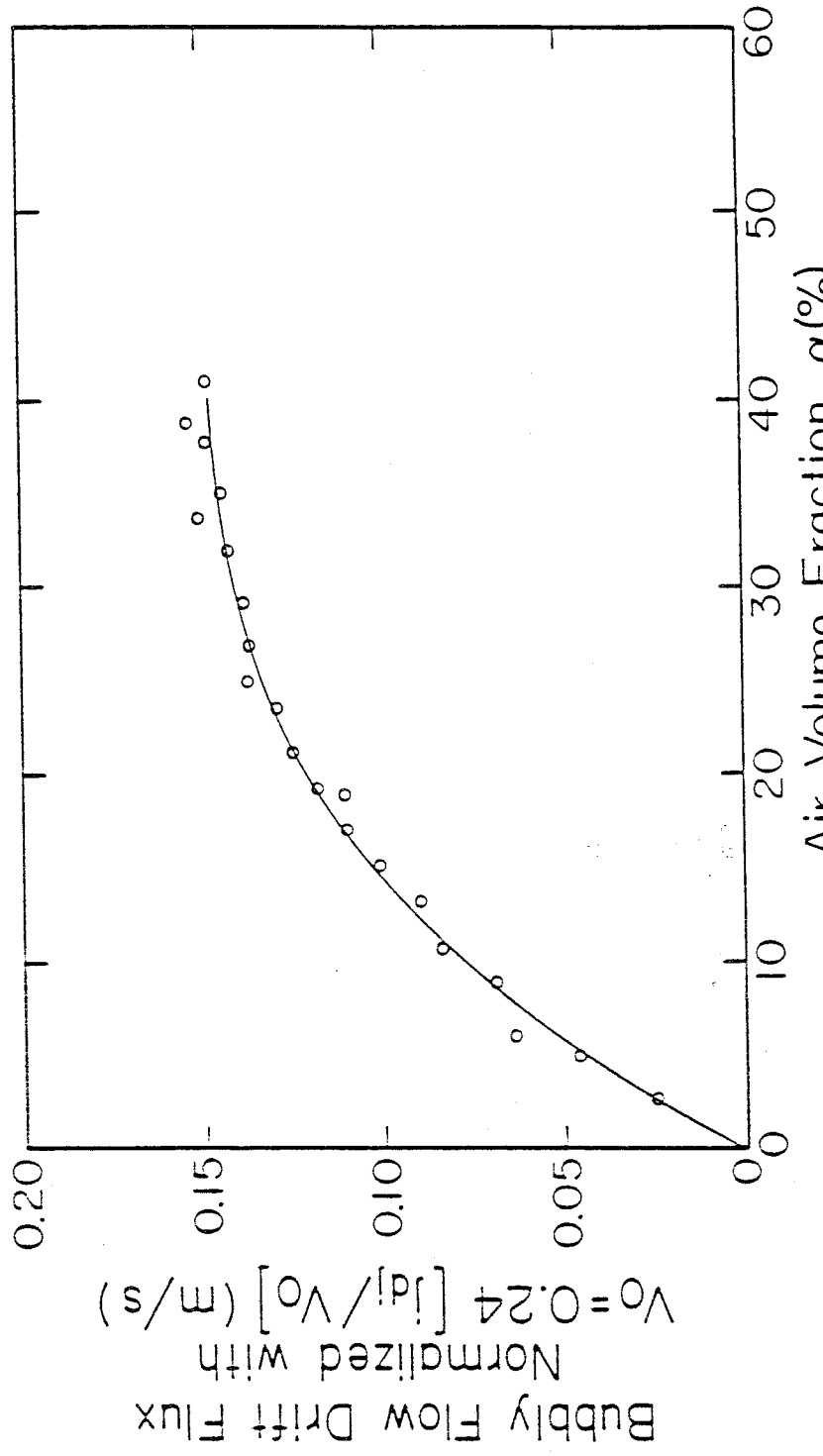

Figure (7.1) Measured drift flux in steady state bubbly flows with least squares fit of the shown points.

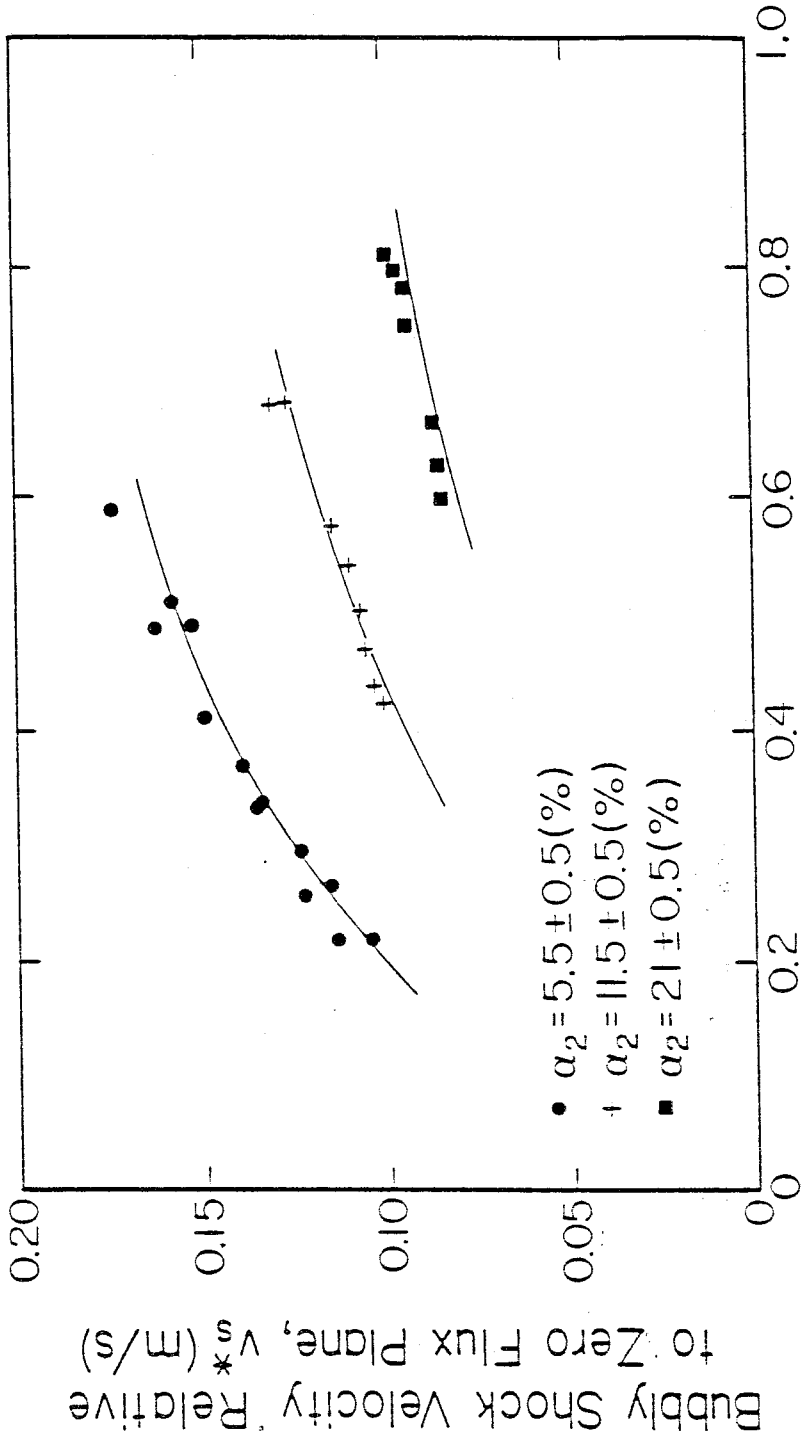

Figure (7.2) Measured bubbly flow kinematic shock velocities relative to the zero flux plane compared to Drift Flux Model predictions based on the curve Figure (7.1).

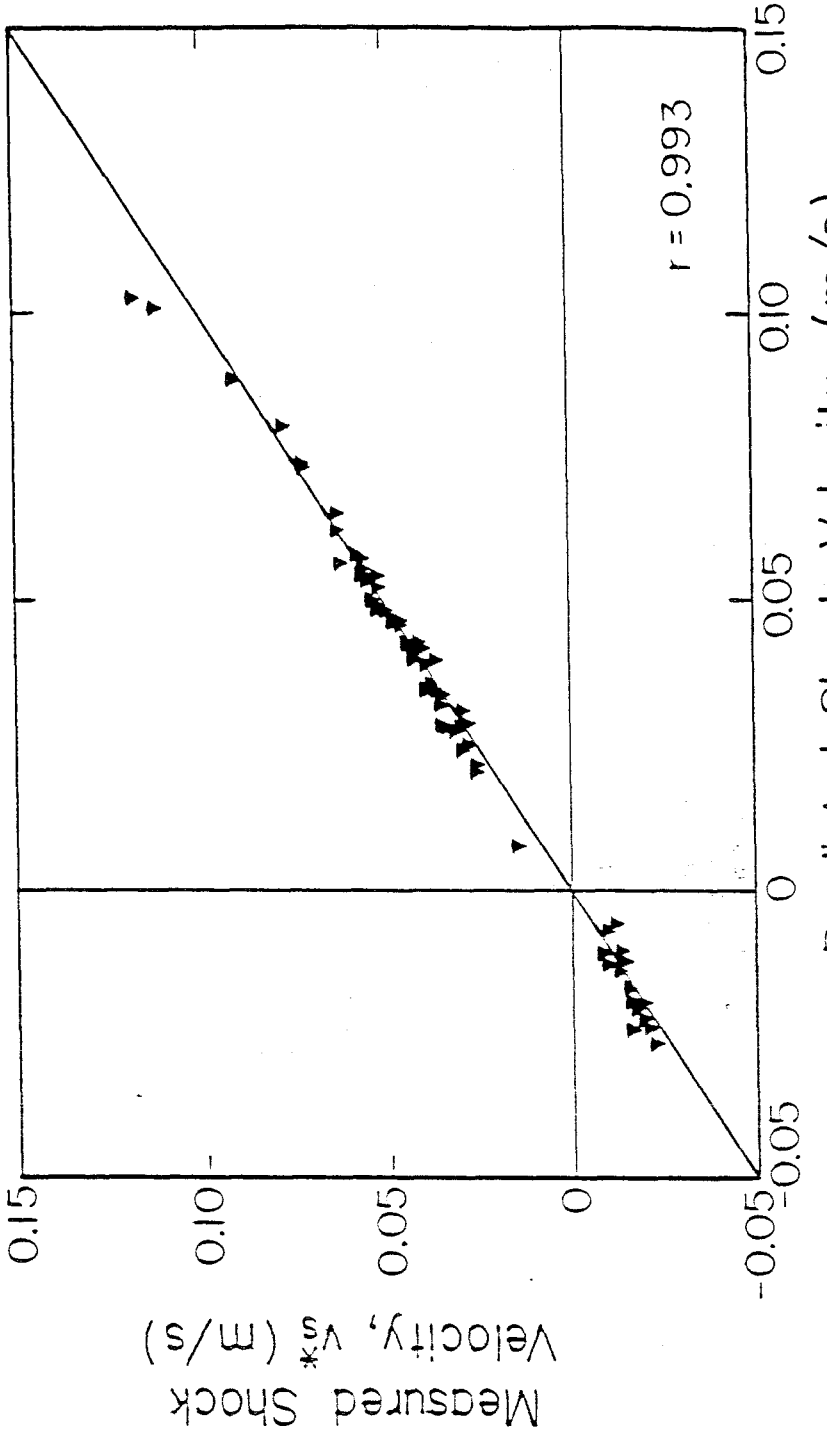

Figure (7.3) Measured particle flow shock velocities relative to the zero flux plane compared to values predicted by the Drift Flux Model based on the best fit drift flux curve.

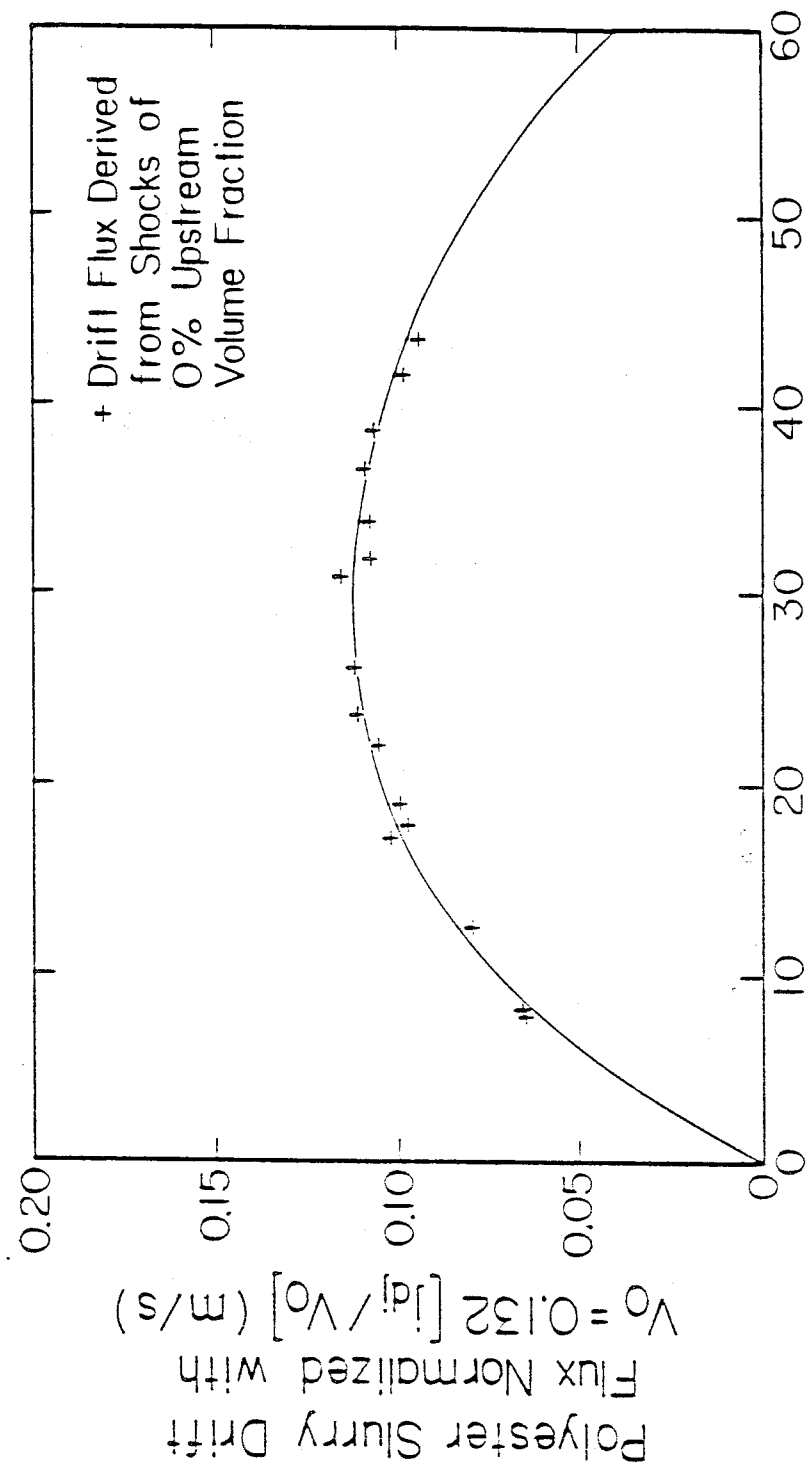

Figure (7.4) Best fit drift flux curve of particle-water flows based on measured shock speed measurements, with values of drift flux determined from shocks of zero upstream volume fraction.

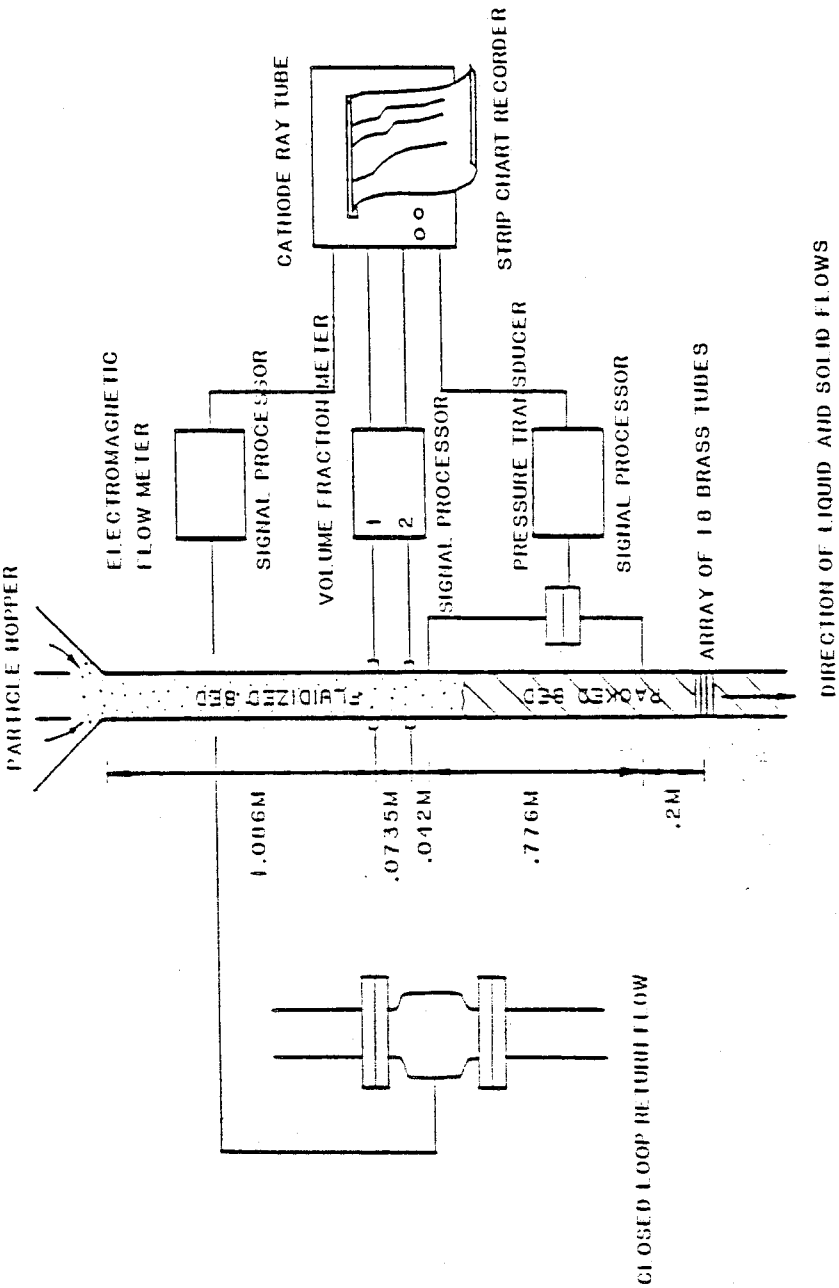

Figure (7.5) Schematic of the instrumented test section set up for the capture of solidification waves in high concentration solid-liquid flows.

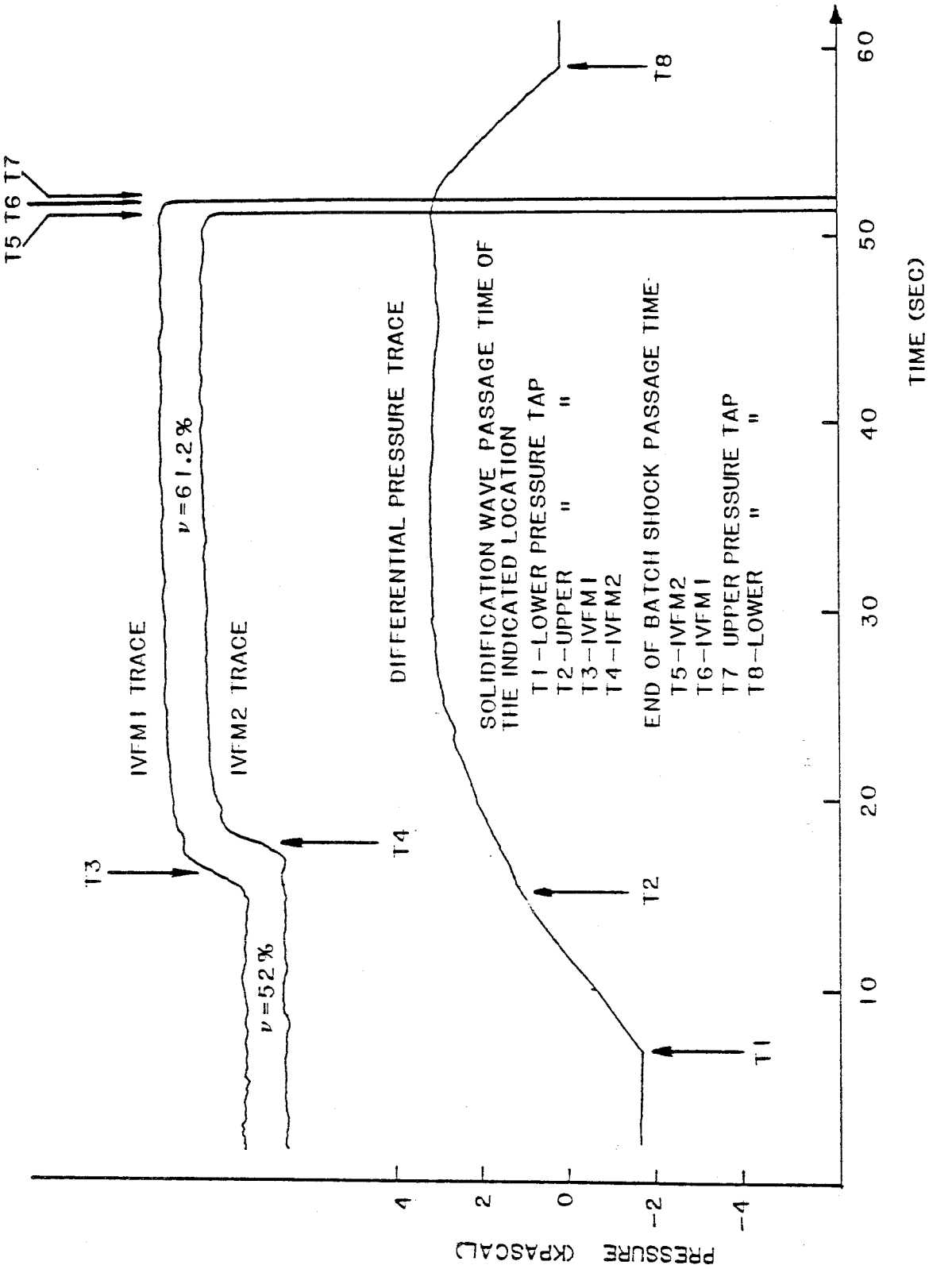

Figure (7.6) Typical volume fraction and differential pressure traces obtained in solidification wave experiments.

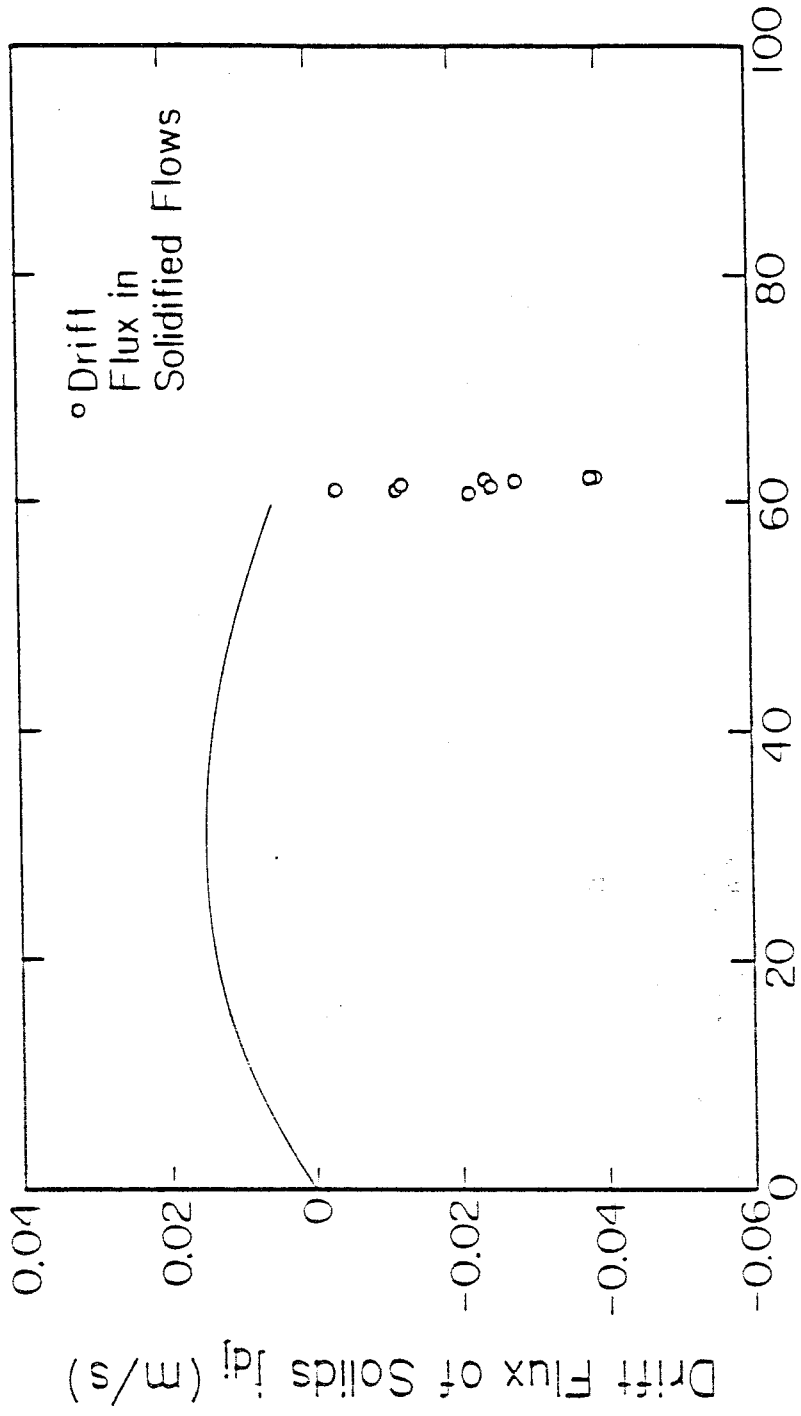

Figure (7.7) Measured solidified flow drift flux (circles) with the fluidized flow drift flux curve (solid line), showing a sign reversal in the drift flux upon solidification.

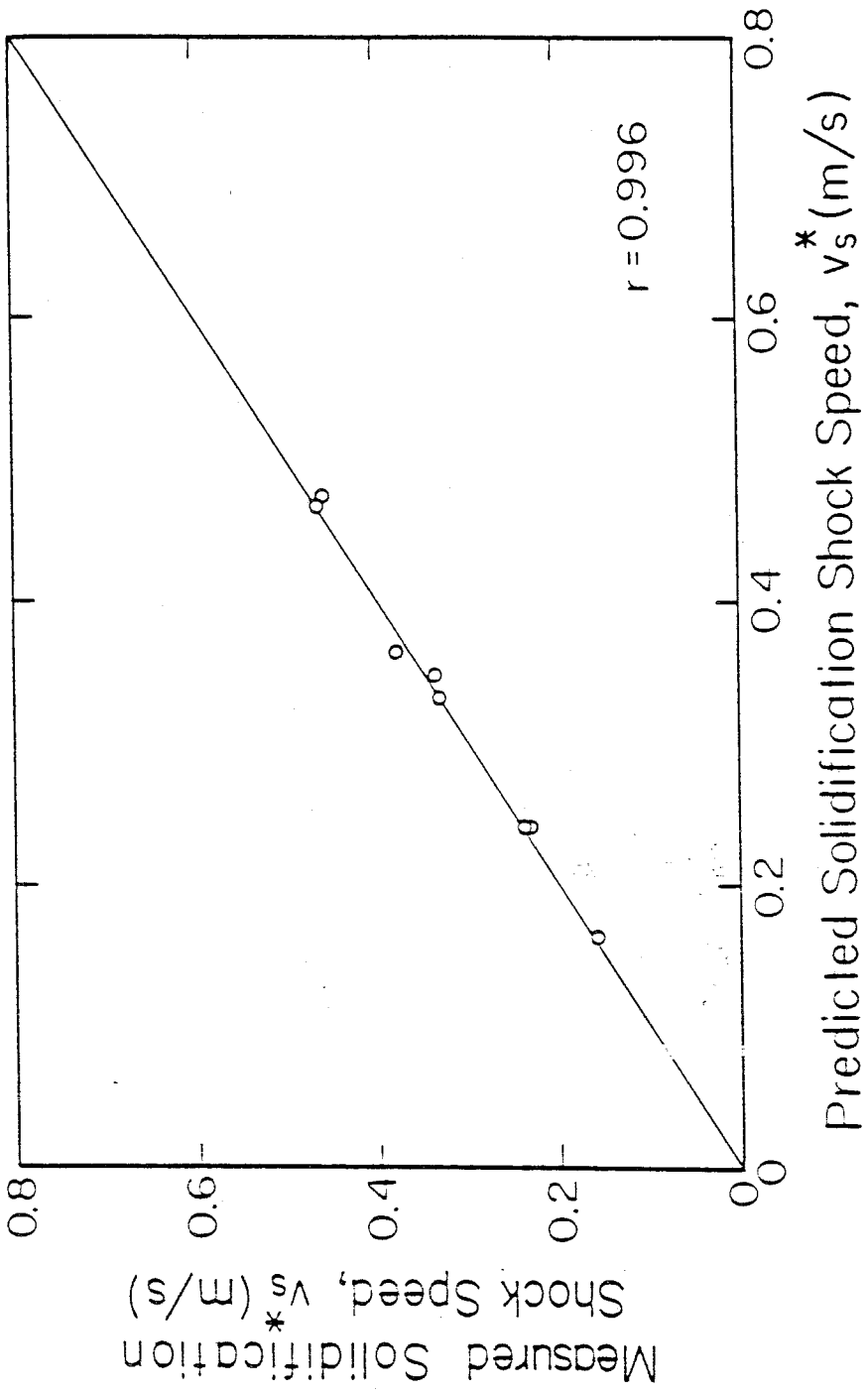

Figure (7.8) Measured solidification shock speeds compared to values based on the drift flux jump across the shock.

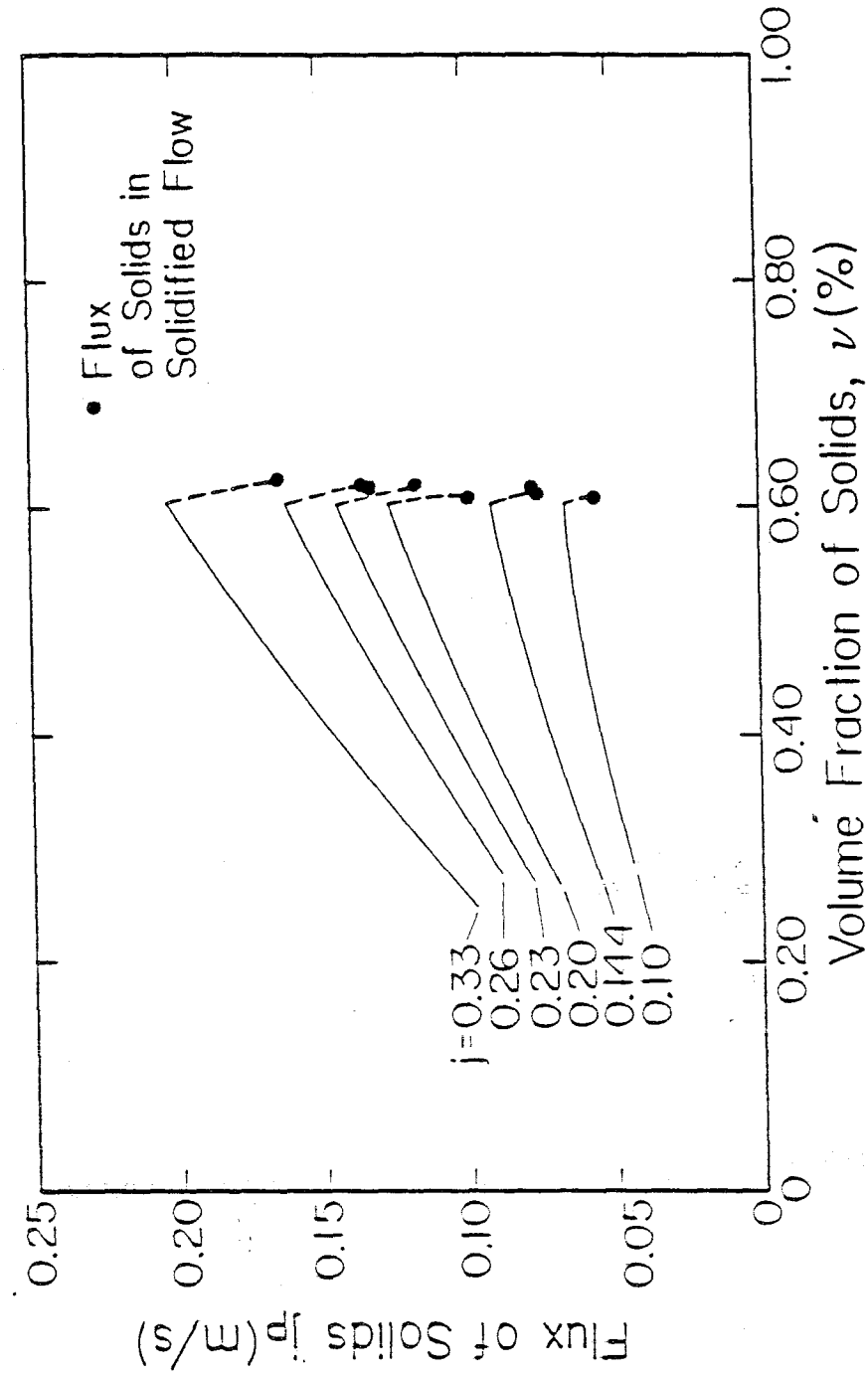

Figure (7.9) Particle flux shown as a function of the volume fraction for different values of the total flux j (m/s), exhibiting "choking" upon solidification.

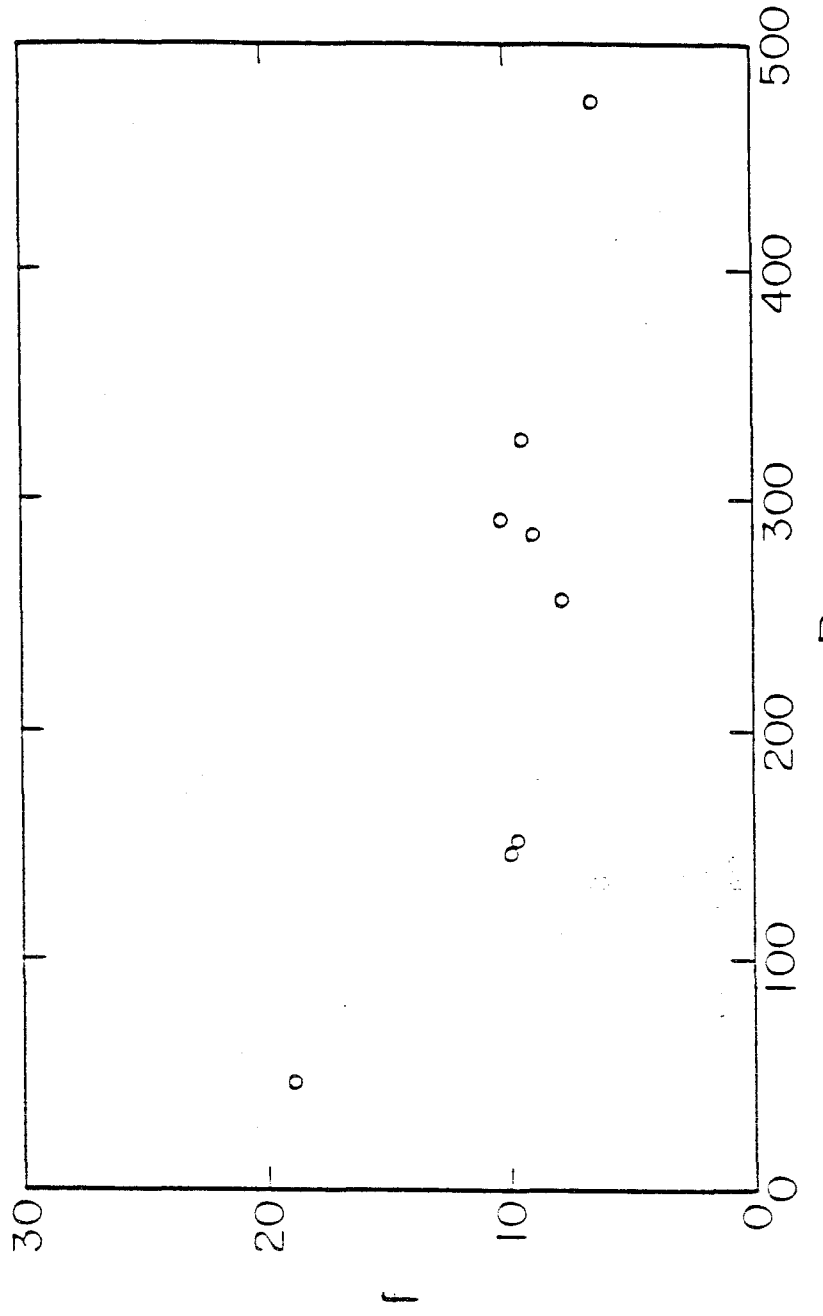

Figure (7.10) Packed bed friction factor based on the liquid density and the slip velocity versus Reynolds number based on the liquid viscosity.

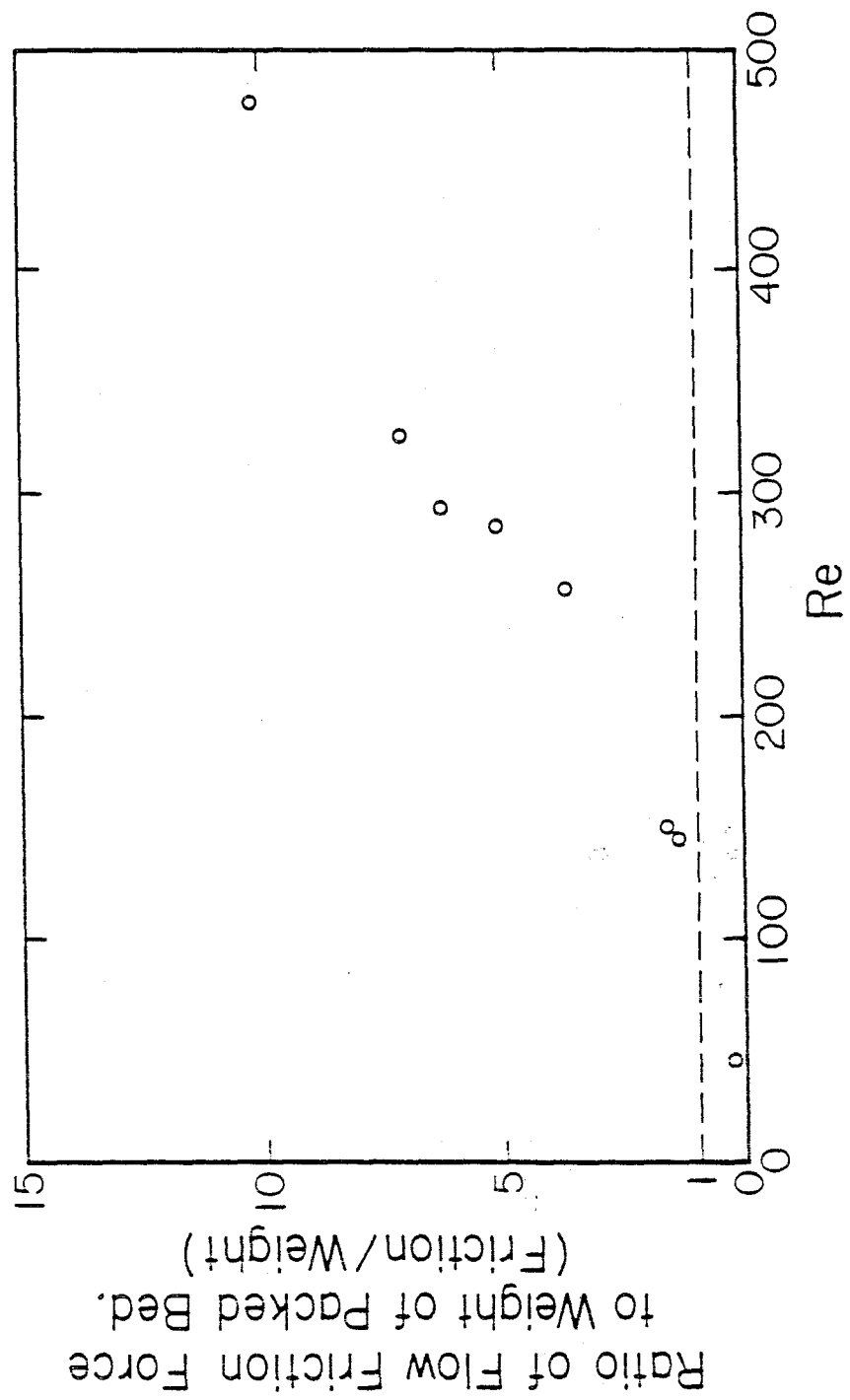

Figure (7.11) (Flow friction / buoyant weight) ratio of body forces acting on the solidified medium versus Reynolds number based on the slip velocity and the particle diameter. The two body forces are equal at Re=100.

Chapter 8. STATISTICAL PROPERTIES OF STEADY STATE TWO- AND THREE-COMPONENT FLOW VOLUME FRACTION SIGNALS.

8.1 Introduction.

It has been shown by a number of investigators (Ishagai (1965), Jones & Zuber (1975), Bernier (1981)) and in the present work that the fluctuations in measured multi-component flow quantities contain valuable information on the mean properties of the flow. In Chapter 4 the perturbations of the IVFM output signal about the mean were used in the dynamic calibration of the volume fraction measuring device. There, we used the characteristic decay time of the auto-correlation function of the fluctuations to deduce the spatial penetration of the influence volume and showed it to remain approximately constant. In the same chapter we also showed that the mean square value of the fluctuations in the form of the IVFM Signal To Noise Ratio could also be used as a measure of the mean volume fraction for both bubbly and particulate disperse flows. Furthermore, the noise in the volume fraction signal at two closely spaced locations was used in Chapter 6 as the starting point of our analysis of propagation and attenuation of infinitesimal kinematic waves in both bubbly and solid-liquid flows.

In this chapter we exploit the noise further to study the nature of both two and three-component flows as they undergo a transition from the disperse to the agitated fow regime, and we demonstrate that it can be used to measure flow quantities. The noise is characterized by two properties of its auto-correlation function, its amplitude and "width" (coherent time scale). These two quantities are easily measured and are useful characterizations of the flows. The visual observations of the transition of air-water flows from bubbly to churn-turbulent are related to the amplitude and characteristic decay rate of the auto-correlation

of the fluctuations. Based on the results, an entirely non-intrusive method of measuring all disperse flow quantities for both bubbly and churn-turbulent air-water flows is suggested.

In the fourth section of this chapter, three component air-solids-water flows in a vertical pipe are investigated. Visual observations of the flow patterns show that the three component flow can exhibit strong unsteady vortical motion. A flow regime map is presented showing both disperse and agitated three-component flows; this is is compared to the results of the bi-disperse stability analysis described in Chapter 5. The statistical properties of the fluctuations of volume fraction signals are compared to flow quantity measurements and regime observations.

8.2 Bubbly and churn-turbulent flows.

In Chapter 4, the statistical properties of the IVFM signal noise were used in the dynamic calibration of the IVFM for bubbly flows of narrow bubble size distribution. The two statistical criteria studied were based on the auto-correlation function of the IVFM signal noise. These were the Signal To Noise Ratio, which is a measure of the noise level relative to the mean signal amplitude, and the time constant, ξ, which is a measure of the coherent time scale in the noise. The quantity , ξ, is determined from the time, $\tau_{1/2}$, at which the auto-correlation function has decayed to half of its peak value. For dynamic calibration purposes ξ was defined as

$$\xi = 1.6783/\tau_{1/2}. \tag{8.1}$$

This quantity ξ is also used in this section.

In churn turbulent flows, the bubble size distribution is very broad and so is the rise velocity distribution relative to the fluid. Evidently, analysis of this problem is far from being simple and is beyond the scope of this thesis. However,

we present results of measurements of global flow quantities and relate these to the statistical properties of the IVFM noise.

The STNR was measured for churn turbulent flows in which the terminal velocity difference between bubble size groups creates a very agitated flow. The nature of bubbly and churn-turbulent flows is illustrated in Figures (8.1) and (8.2) respectively. Large fluctuations are experienced in the churn-turbulent volume fraction signal and lead to a dramatic drop in the STNR as shown in Figure (8.3). At large air concentrations, just prior to transition, the STNR exhibits a maximum value and it rapidly decreases upon onset of churn-turbulence. Therefore, this quantity can be used as a flow regime indicator.

For a bubbly flow of narrow size distribution the time constant of the IVFM signal noise was shown in Figure (3.6) to be linearly related to the average bubble velocity. This is a consequence of the constant influence volume of the IVFM. In general, ξ is a function of both the size and the speed of the travelling flow structure. In Figure (8.4) we present the time constant versus the mean air velocity showing the marked decrease in ξ at the onset of churn-turbulence.

The results are shown for different liquid flux values. Constant liquid flux curves assume a "C" shape. Low volume fraction bubbly flows fall on the top right hand tip of the "C". As the air volume flow rate is increased, the measured point proceeds counter-clockwise on the curve. The onset of churn-turbulence at high volume fraction ($\sim 40\%$) is manifested as a sharp fall in the time constant away from the bubbly flow line. Small values of ξ are indicative of the presence of large structure in the agitated flow regime. Transitional flows fall on the vertical part of the curve and "fully developed" churn-turbulent flows on the monotonically increasing lower branch of the curve. The average gas velocity is found to assume a minimum during transition.

In engineering two component flows, one is interested in knowing the global

flow quantities such as the flow rates. The air flow rate was directly measured in our experiments. In Figure (8.5) we show ξ versus the air flux for fully developed churn-turbulent flows. All points fall on the same monotonically increase curve with little scatter. Unlike bubbly flows, these results show that we can directly monitor the total churn-turbulent air flow rate with a single measurement of the time constant of the IVFM signal noise. The churn-turbulent flows are found to be self limiting in volume fraction. In the flows considered, all measured volume fractions fall between 35 and 45%. Consequently, the air flux, j_{air}, which is the product of the volume fraction and the average air velocity, was found to behave like the mean gas velocity by displaying a monotonic rise in value when presented versus ξ. Furthermore, the ξ-j_{air} curve is found to contain less scatter than the churn-turbulent part of the ξ-v_g plot.

In conclusion, both the Signal To Noise Ratio and the time constant, ξ, measured for air-liquid flows were found to undergo a sharp decrease in value upon onset of churn-turbulence. This behavior can serve as an indicator of the nature of the flow. It was also shown that the time constant, ξ, is well correlated with the total air flux in churn-turbulent flows. This finding shows that the IVFM noise auto-correlation function can be used to monitor the air flow rate non-intrusively.

8.3 Solid-liquid flows.

The solid-liquid flows studied consist of polyester particles of an average diameter of 3 mm. These flows do not display any distinct change in flow regime and remain disperse for the range of total volume flux considered (0-.24 m/s) and volume fractions of up to 60%. Figure (8.6) shows a disperse solids-water flow of 12% volume fraction. At large volume fractions, the solids flow as a plug. Such a flow is shown in Figure (8.7). We take advantage of the absence of instabilities in solids-water flows to investigate whether the useful results for

disperse bubbly flows hold for particulate flows. Namely that the STNR can be used as a measure of total volume fraction and that the time constant ξ is linearly proportional to the average disperse medium velocity. Measured values of ξ are presented versus volume fraction for different total fluxes in Figure (8.8). In the solid-liquid flows, ξ behaves as one would expect the particle velocity v_p to behave. It gradually decreases with ν for constant total flux (the settling velocity decreases with increased volume fraction) and for a given value of ν, the higher the total flux the larger the resulting ξ.

In the present experimental facility, we have no direct means of evaluating the particle flow rate or speed. In Chapter 7, we indirectly determined the particle flow drift flux curve from shock speed measurements. We use this result as the basis for a comparison. The estimate of the solids average velocity is given by

$$v_p = \frac{j_{pj}}{\nu} + j, \tag{8.2}$$

which is derived directly from the definition of the drift flux. The velocity given by (8.2) is not an exact measure since $j_{pj}(\nu)$ was derived for zero total flux, and it is now applied to non-zero flowrates. For the maximum total flux considered (.25 m/s which corresponds to Re=25×10^3) it is used as an indicator of the disperse medium velocity. Experiments were carried out for volume fractions ranging from 6 to 55%. The results presented in Figure (8.9) show that indeed, the suggested method based on the determination of the characteristic coherent time scale of the IVFM "noise" can be used as a non-intrusive measurement of the disperse medium velocity with an expected error within $\pm 25\%$ of the measurement.

8.4 Air-solid-liquid three component flows.

Three component flows consisting of polyester particles (3 mm diameter) and air bubbles (uncoalesced diameter of 4 mm) in a continuous medium of

water were investigated for low total fluxes ($j < .06\,m/s$), and total volume fractions up to 50%. The results are described in the following sections.

8.4.1 Measurement of the individual volume fraction in a three-component flow.

At the flow rates considered, the pressure gradient in the vertical test section is predominantly hydrostatic. Thus, neglecting the wall effect at these low flow rates, the pressure gradient is linearly proportional to the flow bulk density which is a function of the volume fraction of the individual constituents. We measure the pressure gradient in the medium using a differential inductance transducer between two taps located 1.694 m apart. The lines leading to the device are filled with water; therefore the measurement is relative to the hydrostatic pressure difference in water over the same height. Hence, the device output pressure can be presented as a linear combination of the disperse medium volume fractions:

$$\Delta p = \rho_l L \left[\nu(\rho_p - \rho_l) - \alpha(\rho_l - \rho_g)\right]. \tag{8.3}$$

The mean IVFM output gives the sum of the air and solid volume fractions. Since the material constants in (8.3) are known, the two volume fractions can therefore be computed from the two measurements.

We also monitor the total and air flow rates with an electromagnetic flow meter in the pure liquid branch of the flow loop, and an orifice flow meter respectively.

The fluctuations in the IVFM output were recorded on analog magnetic tape and a detailed study of their statistical properties are described in Section (8.4.4).

8.4.2 Flow pattern observations.

One of the distinctive characteristics of three component flows is the dramatic increase in the level of audible noise caused by particle impact against one

another and the pipe wall. This was found to be true for all volume fractions of air and solids. It is interpreted as a consequence of the increase in the disperse medium pressure caused by bubble-particle interactions. This effect demonstrates the enhanced erosive property of three component flows. The dominant feature of the flows considered is the appearance of large vortical structures above a total volume fraction of 30%. These vortices have a typical dimension of the same order as the pipe diameter (Figure (8.11)). At high solid volume fractions the air flow is hardly visible, indicating that the bubbles tend to flow in the central region of the pipe. At larger air flow rates, air slugs do however become visible. Below the total volume fraction threshold, the flow is well behaved; both components flow in a dispersed fashion and both are visible. A long time exposure of this type of flow shows small streak-like structure in the flow (Figure (8.10)).

The visual observations for the three component flows studied are compiled into a flow regime map which is shown in Figure (8.12). There are two flow regimes, the disperse well behaved flows, and the agitated vortical flows. The agitated vortical flows are represented by solid points. The three component flow stability boundary, which we calculated in Chapter 5, is superposed on the figure for comparison. It must be noted that at the onset of vortical flows the air volume fraction typically decreases. This is a consequence of a larger average gas velocity for the same air volume flow rate caused by bubble coalescence. In practice, this means that once a flow turns unstable, it may fall back into the stable side of the stability boundary according to the component volume fractions. Therefore, only the "stable" experimental points can be compared to the results of the linear stability model. Figure (8.12) shows reasonable agreement between observations and the bi-disperse flow model. Some flows were observed to be stable while the model predicts them to be unstable. It

must be noted that the subjective method of determining the nature of the flow inherently introduces inaccuracy into this comparison.

8.4.3 Average air velocity in a three component flow.

The average air velocity in the three component flows studied was computed from the total air flux j_g and the calculated air volume fraction α.

$$v_g = \frac{j_g}{\alpha}. \tag{8.4}$$

In Figure (8.13), we present the average air velocity relative to the combined flux of liquid and solids, $v_{g(pl)}$.

$$v_{g(pl)} = v_g - j_p - j_l. \tag{8.5}$$

The velocity $v_{g(pl)}$ indicates the extent of flow interference between the bubbles and the liquid-solid medium. This quantity is shown versus the total volume fraction of the medium $(\alpha + \nu)$. In this plot we find that for flows which do not exhibit large vortical structure the relative gas velocity is small and falls below .05 m/s, at total volume fractions between 15% and 30%. Upon onset of the agitated flows, the relative velocity rises sharply up to .35 m/s. This sudden rise in the relative velocity is characteristic of a change in regime as seen with air-water flows. In their low Reynolds number work on suspensions, Fessas & Weiland (1981) observed similar behavior in the settling velocity of heavy particles in a bi-disperse medium. They present the settling velocity of one species as a function of the concentration of the other, with the concentration of the first as a parameter. The curves display the same initial decrease that we find followed by a sharp increase after a minimum value is reached. Visual observation of their sedimenting flows revealed segregation of species into vertical fingers subsequent to the regime change, unlike the flows studied at present, which manifest large vortical structure subsequent to the loss of stability of the disperse regime.

All the present relative velocity data falls on the same general curve when presented as a function of the total volume fraction of the disperse medium. This is also true for Fessas & Weiland's data though they do not make note of this fact. This property was assumed in a low Reynolds number bi-disperse model by Lockett & Al-Habbooby (1974) and proved to give good agreement with experimental data. It therefore appears that this property holds not only for flows of small Reynolds number but also for the higher disperse medium Reynolds numbers of about 1000 which pertain to this study.

8.4.4 Statistical properties of volume fraction signals in three component flows.

In this subsection, we study the statistical properties of the fluctuations in the measured volume fraction signals of three-component flows. In Sections (8.2) and (8.3) we showed that the amplitude of the fluctuations presented in the form of the Signal To Noise Ratio and the coherent time scale presented in the form of a time constant ξ both contained valuable information on the nature of the flow allowing distinction of bubbly from churn turbulent flows. The statistical measurements were shown to be correlated to the volume fraction and the disperse phase velocity for bubbly flows, and the churn-turbulent flow air flux.

The STNR of the IVFM signal was calculated by dividing the mean IVFM output by the root of the mean square value of the fluctuating component of the signal. For the three component flows studied, the STNR shown in Figure (8.14) displays a nearly linear dependence on total volume fraction, with a scatter of $\pm$ 5%. The STNR of well behaved disperse flows coincide with the disperse flow curve which was obtained in Chapter 4 for both disperse bubbly and disperse solid flows. The flows which exhibit large vortical structure assume STNR values below this curve. The narrow scatter of the results indicates that this type of

measurement has potential as a means of monitoring the total volume fraction. On the other hand, we saw in Section (8.2) that the STNR takes a dramatic plunge for churn-turbulent flows thus assuming a large range of values for a small range of volume fractions. This parameter would therefore be a poor indicator of the total volume fraction in churn-turbulent flows. The validity of the STNR as a measure of total volume fraction is therefore questionable for very low solids volume fraction agitated three-component flows resembling churn-turbulent flows. In general, the deviation of the STNR from the disperse flow curve is found to be related to the level of unsteadiness in the flow.

The coherent time scale of the noise in three-component flows is presented in the form of the time constant ξ versus the average air velocity in Figure (8.15). Surprisingly, all points fall on one common curve with a maximum which coincides with the onset of vortical motion in the flow. The maximum value of ξ is 75 with a corresponding average gas velocity of .14 m/s. The behavior of the time constant with churn-turbulent two component flows (Section (8.2), Figure (8.4)) is markedly different from the presently described results. In common to both sets of results is a decrease in the time constant upon onset of unsteadiness in the flow.

8.5 Conclusion.

In this chapter air-liquid and air-liquid-solid mixtures were found to undergo a change in flow regime from a disperse to an agitated nature, whereas solid-liquid flows were found to be stable for all conditions studied. A simple method of measuring the volume fraction of the two disperse components in a three-component mixture allowed us to produce a regime map for bi-disperse flows of low total flow rate. The observation were found to be in reasonable agreement with the flow stability analysis of bi-disperse media developed in Chapter 5. We showed that the auto-correlation of IVFM noise can be used as an indicator of

flow regime and a measure of disperse two- and three-component flow quantities. The noise time constant ξ was found to be well correlated to the air flow rate in churn-turbulent air-liquid flows.

The size and propagation speed of small and large scale structure in churn-turbulent and unsteady three-component flows remains unexplored. Future efforts should be concentrated on applying a combination of auto-correlation and cross-correlation measuring techniques to help us better understand the mechanics and statistics of these complicated flows.

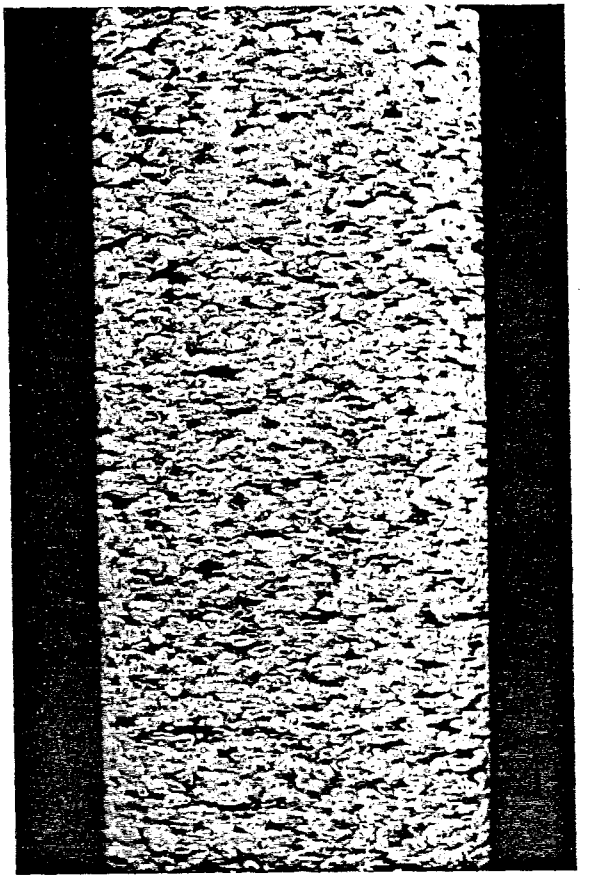

Figure (8.1) Bubbly air-water flow of 8% volume fraction.

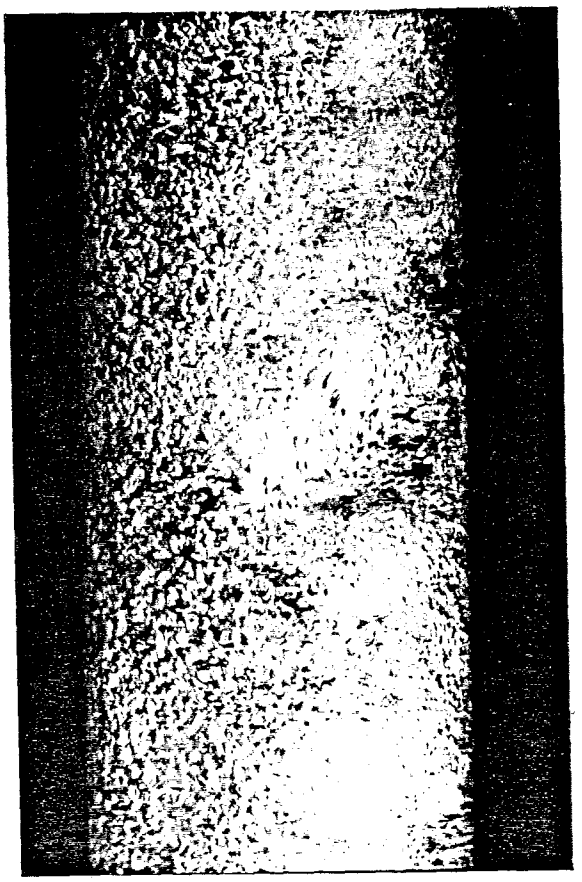

Figure (8.2) Churn-turbulent air-water flow of 37% volume fraction.

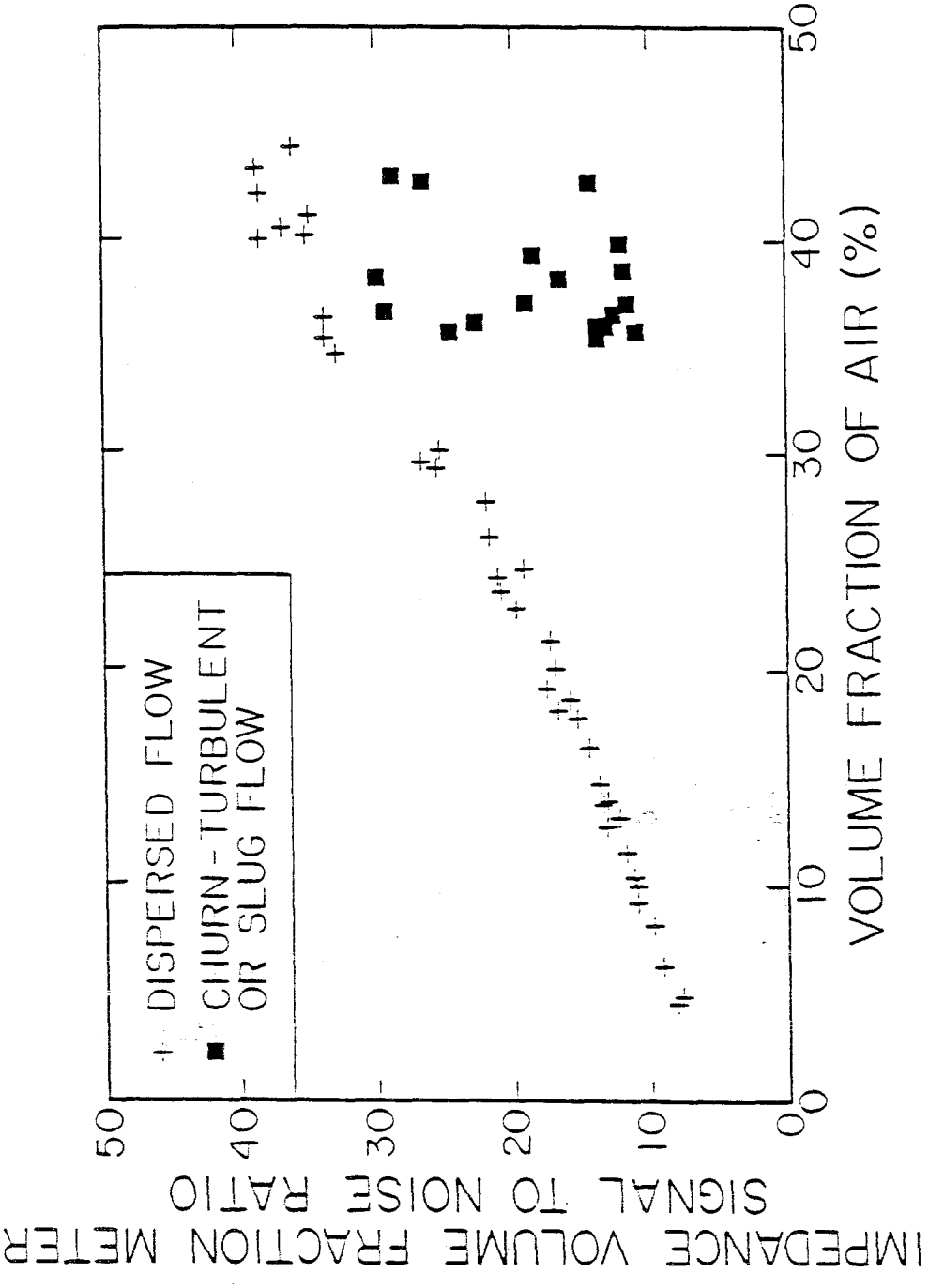

Figure (8.3) Signal To Noise Ratio of the Impedance Volume Fraction Meter output for bubbly and churn-turbulent flows.

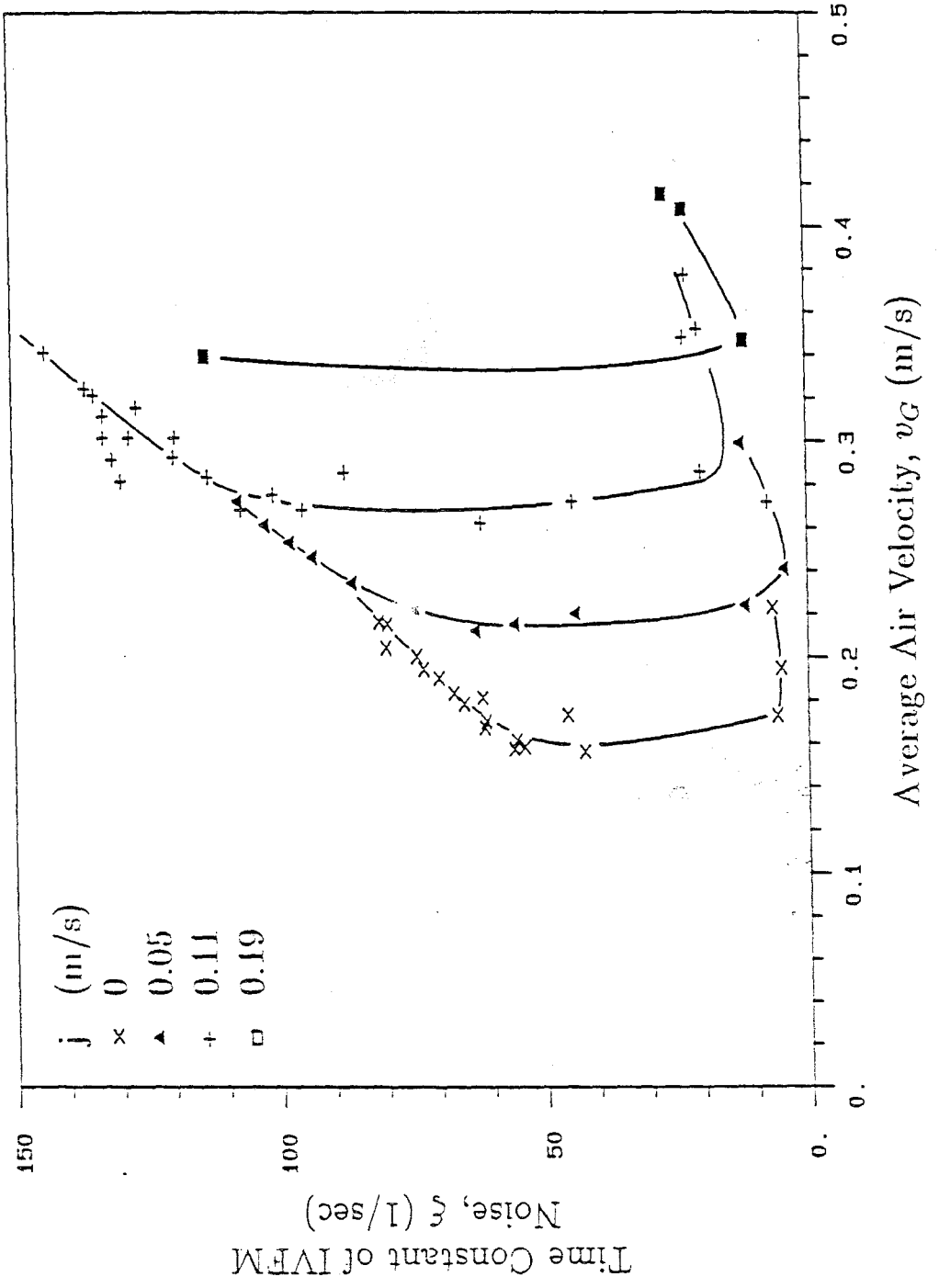

Figure (8.4) Time constant ξ (reciprocal of the coherent time scale) of the fluctuating IVFM output signal in bubbly and churn-turbulent flows versus the average air velocity. Note the dramatic drop in ξ on onset of churn-turbulence.

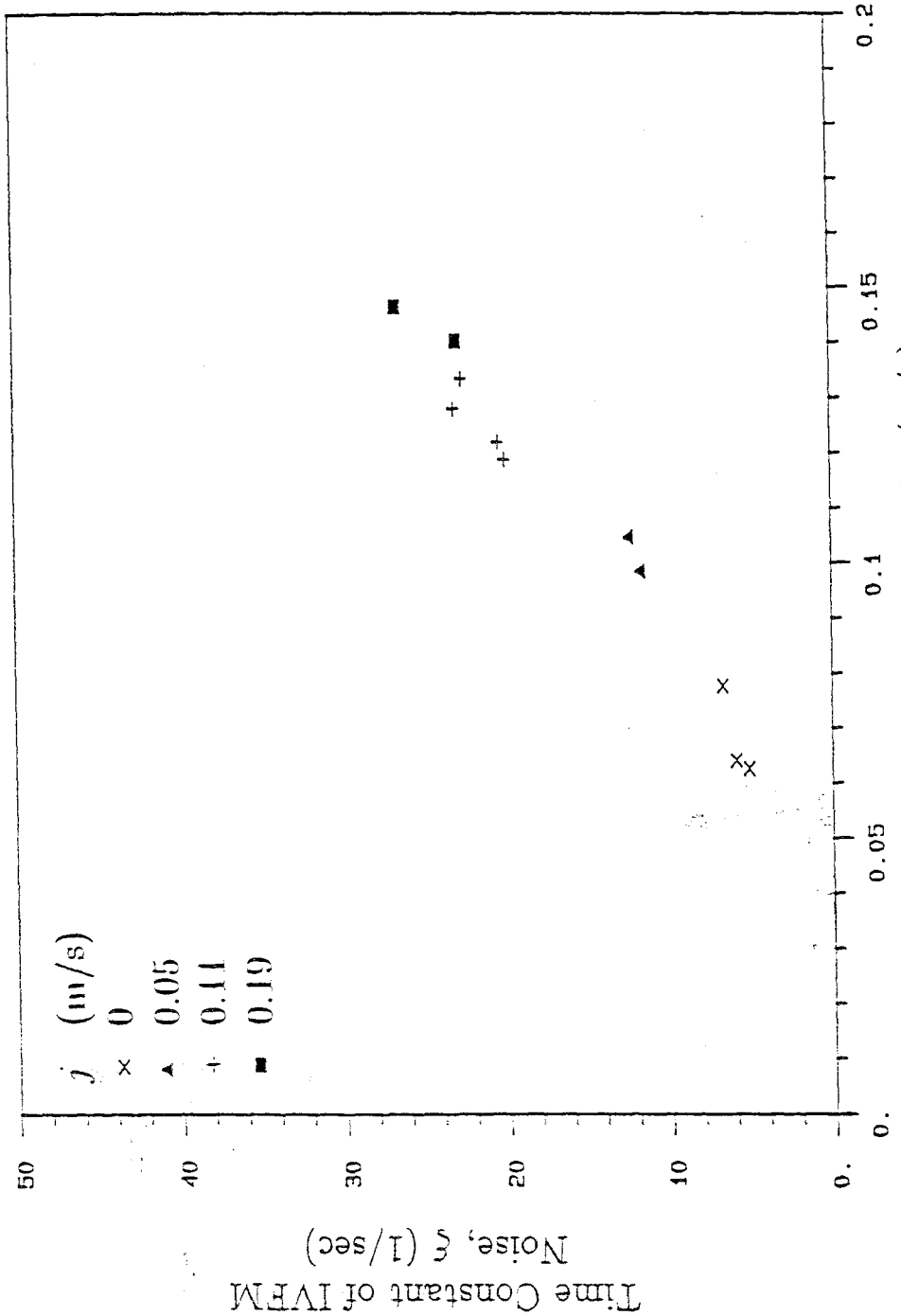

Figure (8.5) Time constant ξ of the fluctuating IVFM signal in fully developed churn-turbulent flows versus the air volumetric flux, showing all points on the one curve with little scatter.

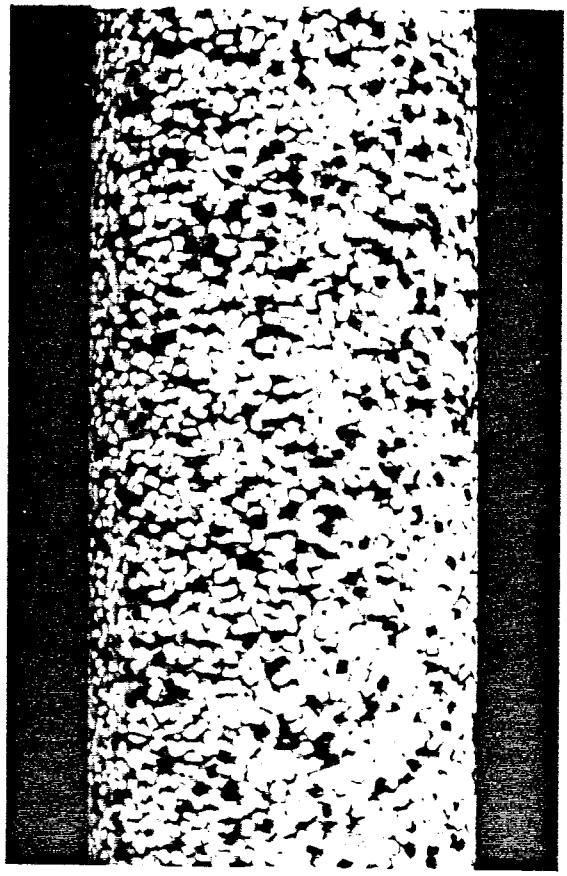

Figure (8.6) Dispersed Solids-water flow of 12% volume fraction.

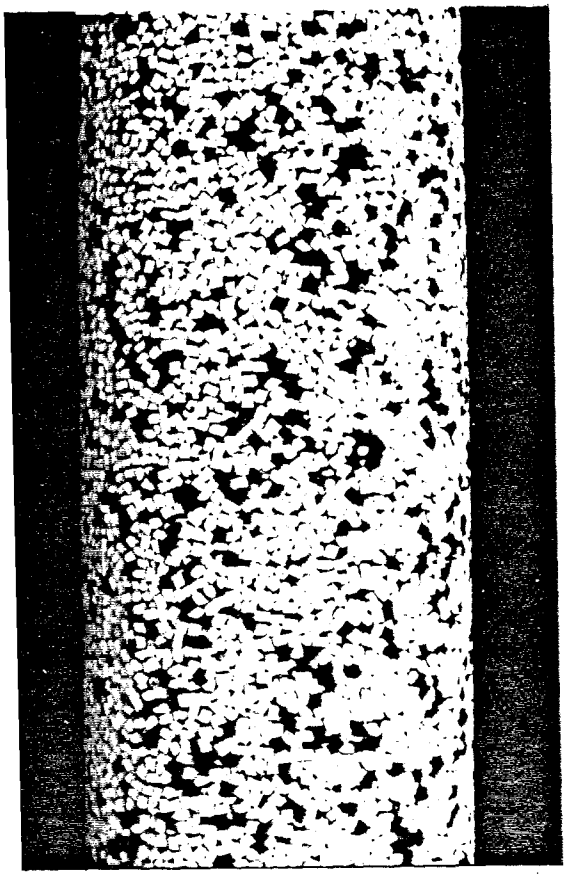

Figure (8.7) Solids-water plug flow of 55% volume fraction.

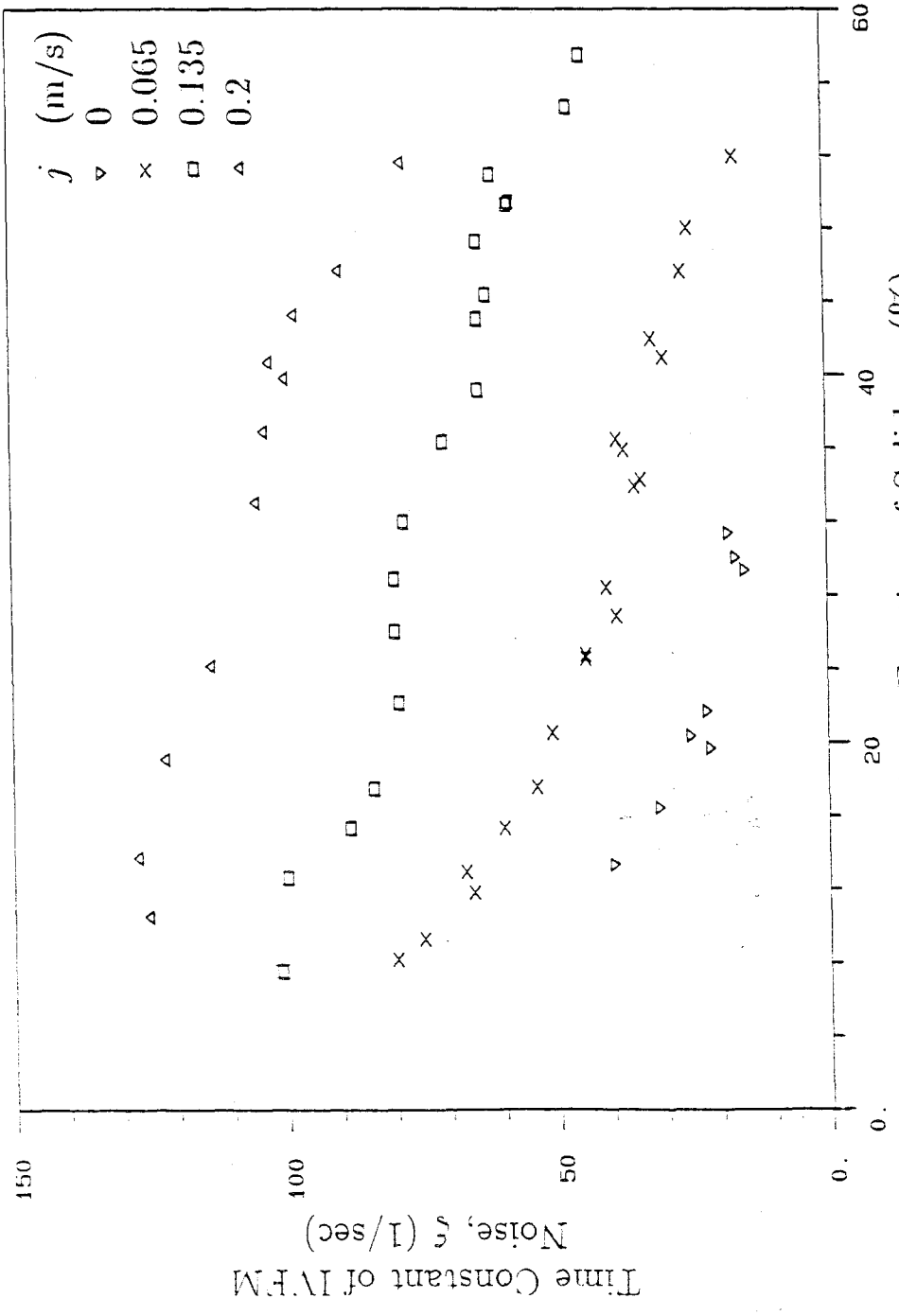

Figure (8.8) Time constant ξ of the fluctuating IVFM signal in particle flows versus the volume fraction with the total flux j as a parameter.

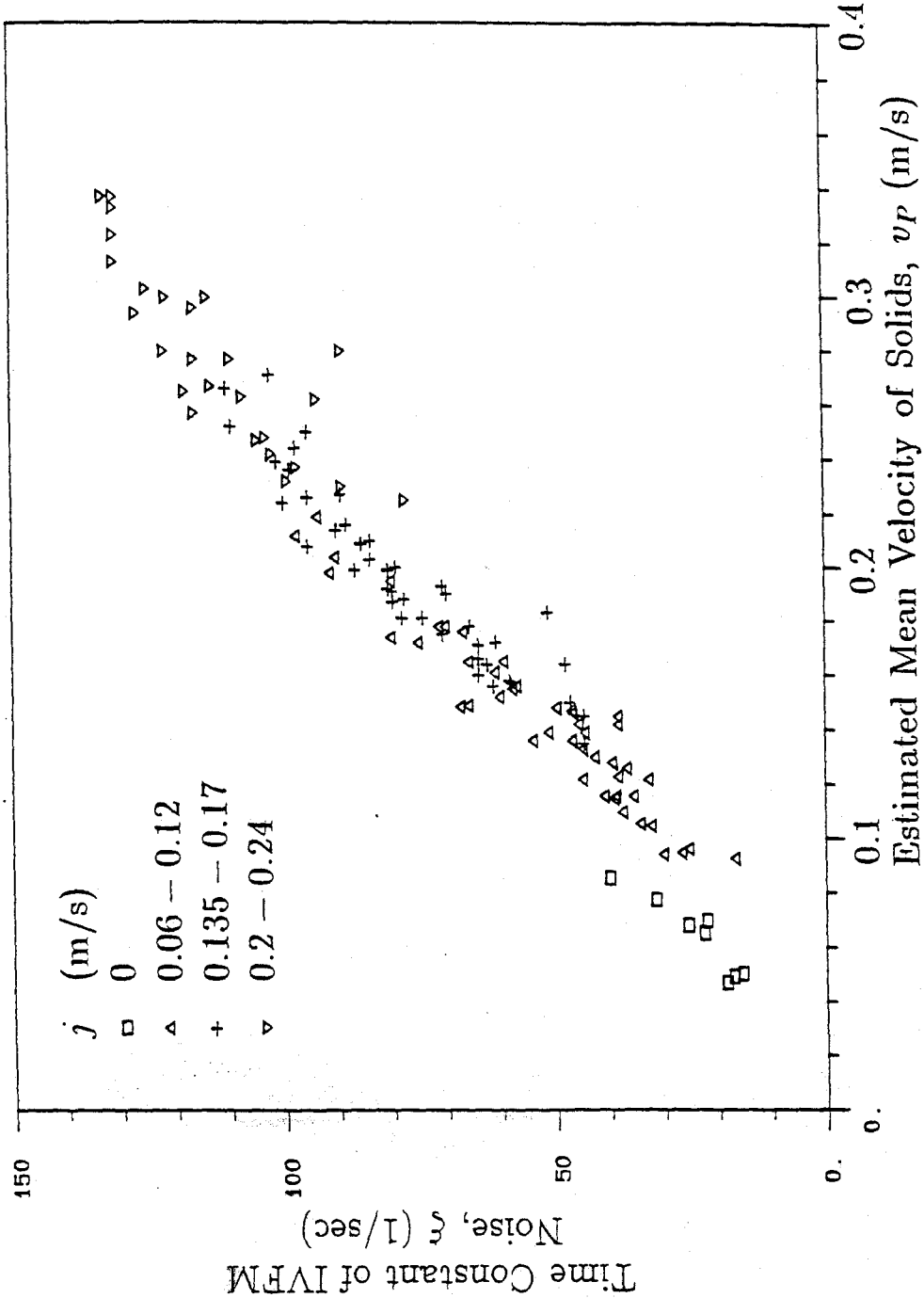

Figure (8.9) Time constant ξ of the fluctuating IVFM signal in solids-water flows versus an estimate of the average particle velocity based on the drift flux function derived in Chapter 7.

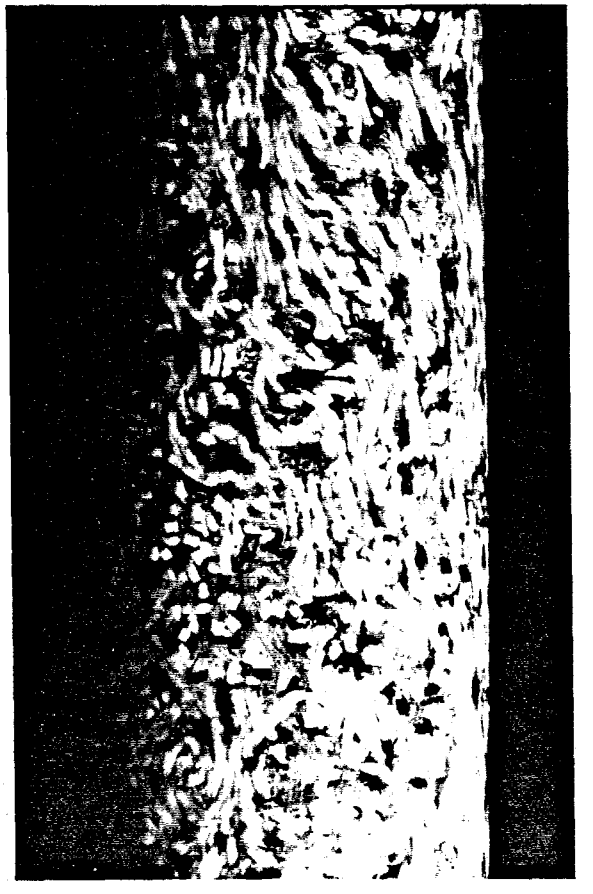

Figure (8.10) Three component flow of 12% solids volume fraction and 15% air volume fraction, showing the small scale structure of disperse flow. 1/30 second exposure was used.

Figure (8.11) Three component flow of 30% solids volume fraction and 15% air volume fraction, showing large vortex structure. 1/30 second exposure was used.

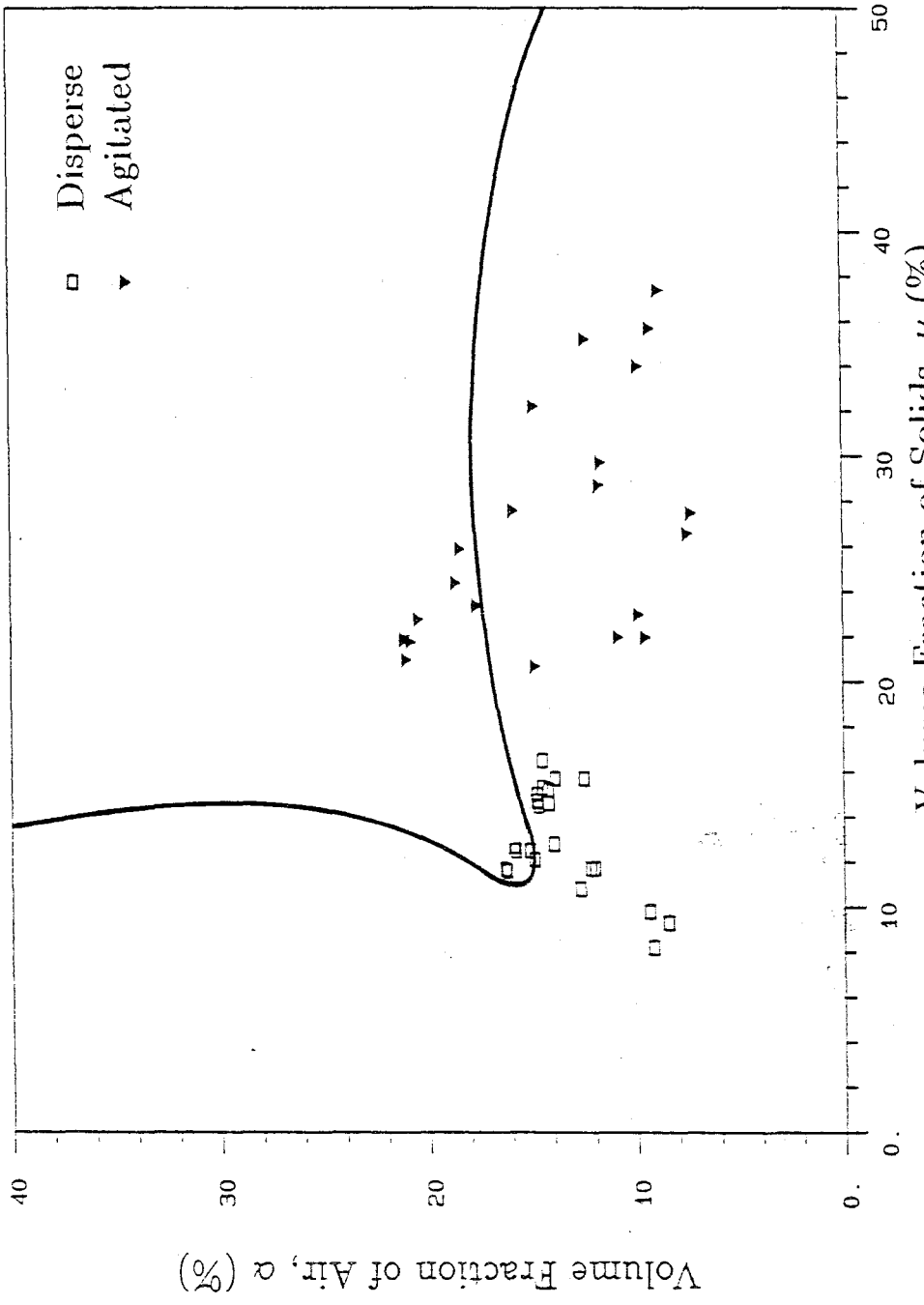

Figure (8.12) Flow regime map of three component flows based on visual observation. The solid curve is the stability boundary determined using the bi-disperse model.

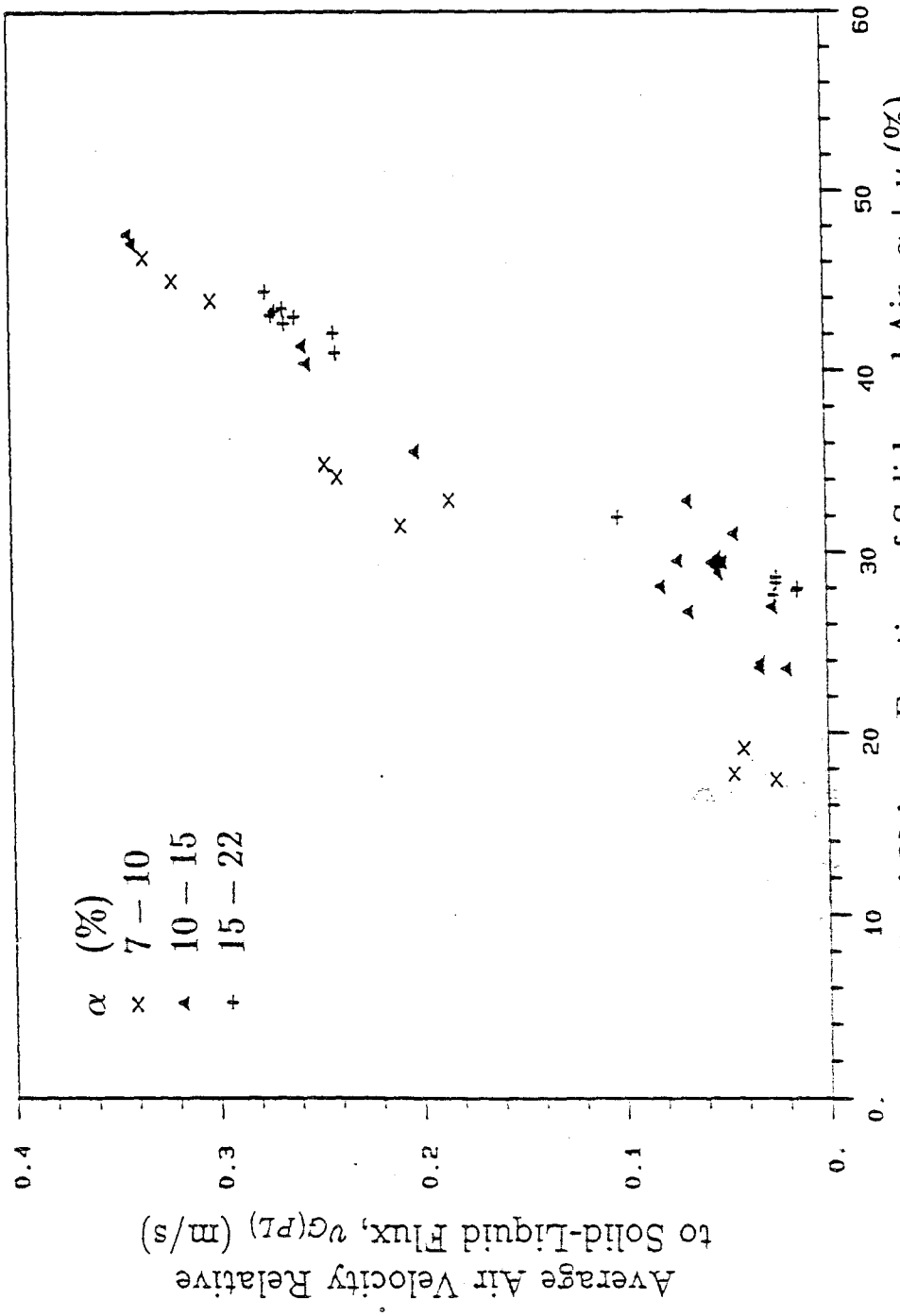

Figure (8.13) Average velocity of air relative to the combined flux of liquid and solids versus total volume fraction of disperse material.

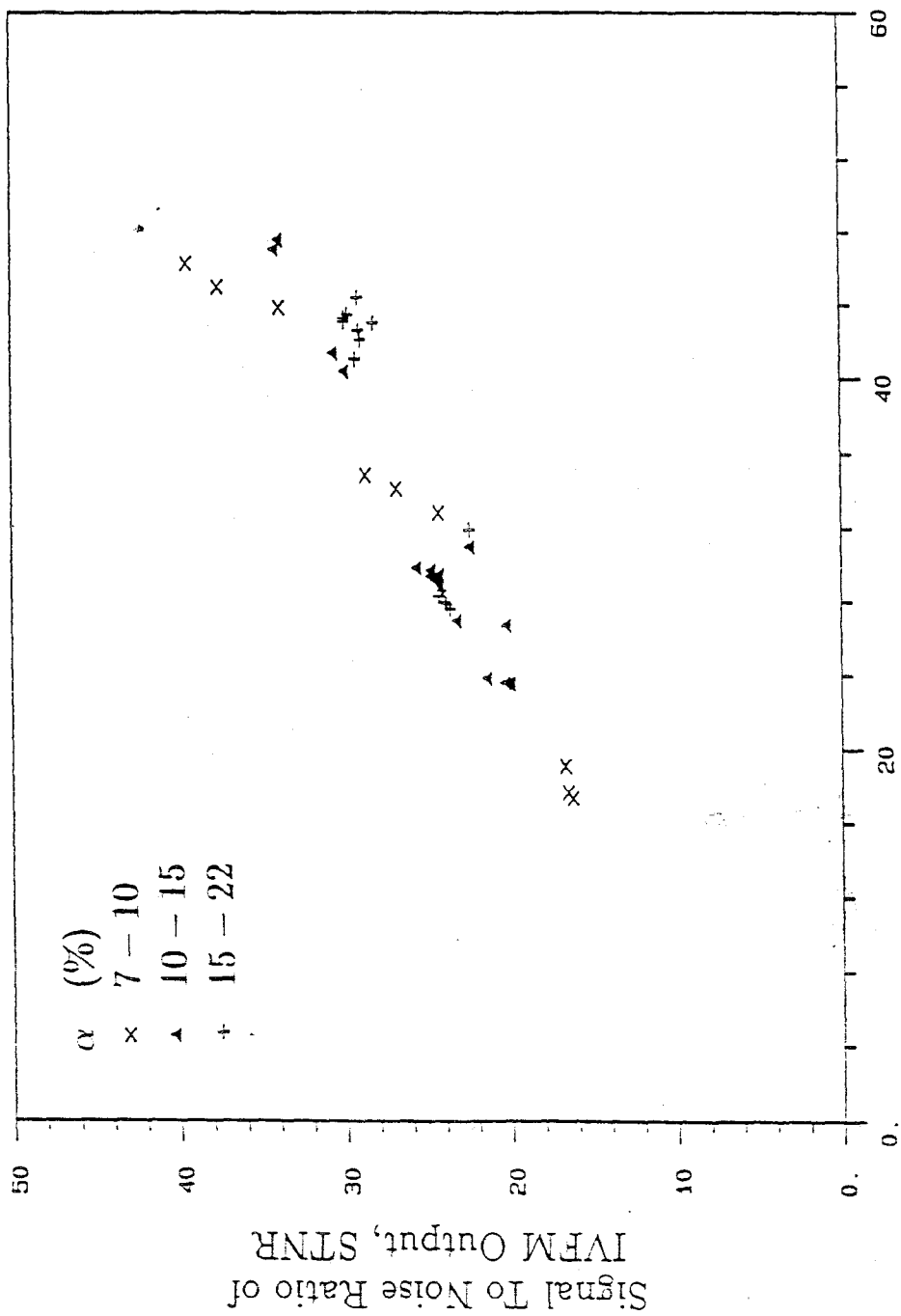

Figure (8.14) Signal To Noise Ratio of the IVFM output in three component flows versus total disperse material volume fraction.

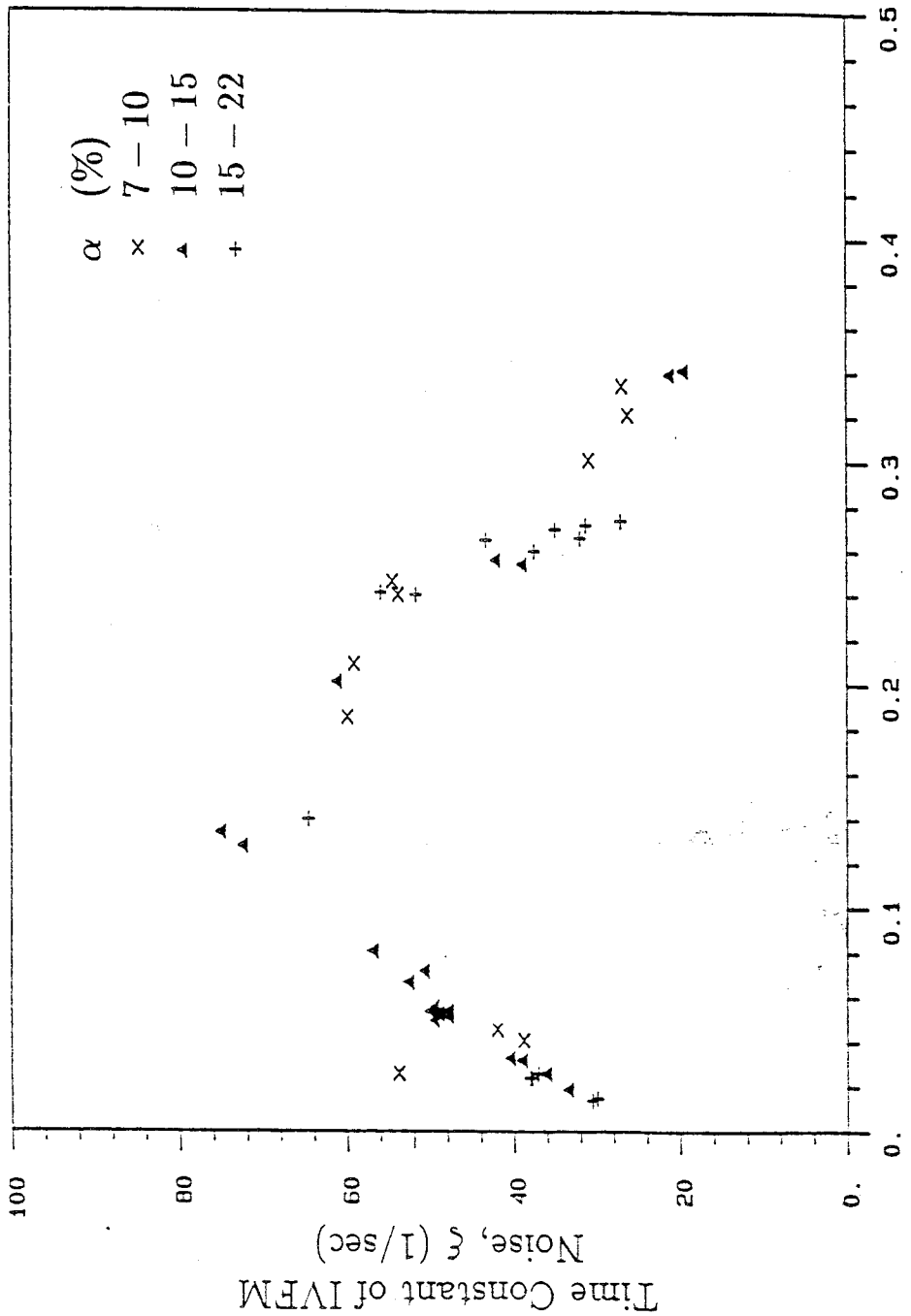

Figure (8.15) Time constant ξ of IVFM output fluctuations in three component flows versus the average air velocity.

Chapter 9. SUMMMARY AND DISCUSSION.

For the purpose of experimental analysis of two- and three-component flow phenomena, a versatile Three Component Flow Facility was built capable of accommodating a variety of media consisting of air, liquid and solids with the liquid as the continuous component. The facility was designed with a vertical test section, but this can be readily changed to any new configuration of interest to the investigator. The flow loop was fully instrumented with both existing and newly developed flow measuring devices such as electromagnetic flow meters and volume fraction meters.

Friction pressure drop measurements were made in bubbly and particulate two-component flows. Very high values of friction pressure drop were revealed with marked departure from previously accepted correlations. The values obtained in solid-liquid flows were up to an order of magnitude higher than the pure liquid values. These behaved monotonically with volume fraction and total flow rate. The higher the volume fraction, the higher the friction pressure drop for constant total flow rate. Bubbly flow results were of the same order of magnitude and were shown to be up to 15 times larger than was accepted according to commonly used models (Lockhart & Martinelli (1949), Armand (1950)). Furthermore, the measured values were found to fall upon the onset of unsteadiness in the flow. This phenomenon is as yet poorly understood and has only been documented in two other studies (Aoki & Inoue (1965), Nakoryakov et al. (1981)) which were carried out for different pipe diameters, making quantitative comparison difficult. Nakoryakov et al. measured volume fraction peaks in the vicinity of the wall. This finding supports the speculation that the increased wall shear stresses are due to enhanced mixing close to the wall caused by the large concentration of bubbles. A semi-empirical mixing length theory based on this observation was developed by N. Clarke (1983), who predicts the sharp rise

of friction multiplier with respect to the air volume quality. The method used in the present work to determine the friction pressure drop resulted in rather large uncertainties due to the required subtraction of the hydrostatic contribution from the measured pressure difference. This uncertainty was particularly large in flows that exhibited unsteadiness, nevertheless by careful analysis of the error, useful data on the frictional properties of these two-component flows could be obtained.

One of the aims of the present work was to improve the performance of the Impedance Volume Fraction Meter (IVFM). The improved IVFM with shielding electrodes and temperature compensation was demonstrated to have good spatial resolution and better temporal response than was needed (the highest measured frequency was 100 Hz, and the ouput is limited by its 500 Hz low pass filter) for the present investigation of unsteadiness in the flow. The output of this non-intrusive device varied linearly with the volume fraction of the non-conducting disperse material. The inherent fluctuations in the output were found to contain valuable information on the flow quantities and regime. The fluctuations were quantitatively represented by the amplitude and half life of the auto-correlation function, in the form of the Signal To Noise Ratio (STNR) and the time constant ξ respectively. These simple quantities characterize the auto-correlation function and the hardware needed to carry out such measurements can be built easily and cheaply. For mono-disperse flows, the relationship between the STNR and the volume fraction is shown to be independent of the IVFM output gain on the condition that the calibration remains linear. Furthermore, the two curves obtained for bubbly and particulate flows were found to overlap almost exactly despite the 25% difference in the bubble and particle sizes. This property eliminates the need for constant recalibration and therefore makes this measuring technique ideal for remote monitoring of volume fraction

in locations where recalibration is difficult (for example in an oil well). The time constant ξ was approximately linearly proportional to the speed of individual particles or bubbles in mono-disperse flows. This result shows that the coherent time scale of the IVFM output fluctuations can be used as a direct measure of the average speed of the disperse material.

Statistical measurements were also carried out in churn-turbulent air-liquid flows and three-component flows. In churn-turbulent air-water flows, the STNR exhibited a marked drop due to the onset of large structure in the flow. The time constant ξ was also found to exhibit much lower values than found in disperse flows. These were well enough correlated to the air flux for ξ to be used as a non-intrusive measure of the total air flow rate. In three-component flows, the STNR was shown to provide a measure of the total volume fraction, and agitated three-component flows were shown to yield lesser values of STNR than the well behaved disperse flows. All the time constant measurements were found to fall on the same curve when plotted versus the average air velocity. This curve (Figure (8.14)) has a maximum which coincides with the change in flow regime from disperse to agitated flows. All disperse flows fall on the rising part of the curve and the agitated flows on the falling part. This result was surprising, but found to be quite consistent under the conditions studied. In conclusion, the IVFM which was originally developed for the purpose of measuring volume fraction was demonstrated to be capable of measuring other disperse flow quantities, though it can only yield weighted averages over the pipe cross-section. There is a need for non-intrusive instrumentation capable of measuring variations in the desired flow quantities over the cross-section. Tomographic ray attenuation techniques could be implemeted for this purpose though they have the disadvantages of being bulky and costly and needing safety precautions. Future work should concentrate on implementing tomographic methods in the present volume fraction

measuring technique, which has the advantages of simplicity and low cost.

At the low flow rates studied, the flow regime changes are caused by an instability in the homogeneous dispersion, as opposed to the type of instability responsible for turbulence in single phase flows. In the present work we extended Batchelor's (1986) findings and developed a bi-disperse flow model that showed that size distribution can be an important driving factor for the growth of concentration perturbations at high volume fractions of the disperse material. Indeed, a loss of stability in air-liquid mixtures was observed at high volume fractions ($\sim$ 40%). Churn-turbulent flows were found to exhibit nearly constant volume fraction (35-40%) even with increased air flow rates. Experiments also showed a fundamental difference between air-liquid and solid-liquid systems. The homogeneously dispersed state of solid-liquid flows were found to be stable under all conditions studied. The suspected explanation lies in the physical differences between the two systems, namely in the inability of the bubbles to withstand bubble-bubble forces beyond a threshold value dictated by the bubble size and surface tension.

The tendency of the medium to retain or lose structure and the propagation speed of the structure were evaluated experimentally in the present work by analyzing the coherent signal common to two IVFM's separated by .0735 m under steady state two-component flow conditions. The structure was found to propagate as small amplitude volume fraction waves (kinematic waves) whose velocities agreed with theoretical predictions, particularly for bubbly flows. The solid-liquid flow measurements exhibited more scatter. The kinematic waves were found to be non-dispersive for the wave numbers for which the measured volume fraction perturbations were significant. The frequency domain coherence function of the noise of the two IVFM's was derived for the purpose of determining the kinematic wave attenuation in terms of the wave number using

an HP 3562 spectral analyser. A low value of coherence at a certain frequency (which corresponds to a certain wave number) indicates that a perturbation of that frequency does not sustain itself or grow, thus keeping the original homogeneous state free of perturbations of that wave number. On the other hand, a high coherence value represents a sustained perturbation at that wave number, indicative of structure that persists in the flow and can lead to instability. Thus we were able to detect the onset of churn-turbulence in bubbly flows as a marked increase in the coherence function prior to a change in regime. In bubbly flows, the most persistent wave number was approximately .3 m for volume fractions up to 35 % and it rose to as high a value as .8 m prior to the onset of churn-turbulence. In solid-liquid flows, the structure was found to be increasingly persistent for flow volume fractions above 15%, but no change in regime was observed under any conditions. The homogeneous state was found to be stable for all conditions, despite the sustained structure in the flow. The most persistent wave number in these particulate flows was measured to be approximately .5 m up to a volume fraction of 40 % above which it decreased to .15 m. This decrease is believed to be a consequence of the general broad band increase in coherence at very high concentrations due to the process of solidification. The ability of particles to sustain large forces therefore introduces persistent structure to the medium particularly at high volume fractions. The kinematics of the flow may promote instability, but this is resisted by particle-particle forces. It was indeed shown theoretically by Garg & Pritchett (1975) and later by Needham & Merkin (1983) that the collisional pressure has a strong stabilizing influence on the uniform dispersion, but a direct measure of particle-particle pressure has eluded researchers to this day. There is a distinct need for better understanding of the disperse medium pressure and its effect on the stability of two- and three-component flows of low and high Reynolds numbers, as well as the in-

fluence of the related particle-pipe wall pressure on the corrosion of the wall. Savage (1979) and Jenkins & Savage (1983) have presented statistical models of two-component flows for the case of zero density and interstitial fluid viscosity, an asymptotic regime referred to as granular material flow. This approach needs to be extended for the general case of a viscous and dense interstitial fluid.

Finite kinematic waves undergo wave front steepening (due to non-linear properties of the flow), which ultimately leads to the formation of concentration shocks. The propagation of such jumps in volume fraction were studied for both air-water and solid-water mixtures. The direction of kinematic wave propagation was found to be of practical importance in throttling the solids at the top of the test section. In the case of upward propagating finite kinematic waves, which occur at large volume fractions, the effect of throttling the solids flow does not influence the medium downstream of the flow control device, despite the net downward flow of the particles. Under these conditions, adjustment of volume fraction should be done at the bottom of the test-section. In the present study of finite kinematic waves, this difficulty was overcome by imposing a net downward flow to force the created shock to travel downward. The Drift Flux Model was found to describe the propagation speed accurately in terms of the upstream and downstream shock volume fractions.

An obstruction at the bottom of the test section (the air-injector) is found to cause a finite amplitude solidification wave to travel up the test section in downward flows of large initial solid particle volume fraction ($> 50\%$) and total flux between .1 and .4 m/s. The moving packed bed below the wave has the property of transmitting stresses through the solid matrix. The resulting forces on the obstruction were found to be large and potentially damaging. This force originates predominantly from the body force the liquid imparts on the flowing bed, and to a lesser extent from the weight of the bed. This implies that this

process can also occur in horizontal flows of high concentration slurries in the presence of an obstruction. The obstruction was shown to create choking of the particle flux, which results in a sharp drop and a sign reversal in the drift flux function. The speed of these waves was found to be high compared to fluidized shocks, and in full agreement with the Drift Flux Model prediction based on the choked flow drift flux. The fast propagation of a sudden discontinuity in density therefore has a "water hammer"-like distructive property.

Three-component air-solid-liquid flow regimes were categorized into disperse and agitated states based on visual observations. The individual volume fractions of the constituents were measured and the results were compiled into a flow regime map which was compared to the stability boundary predicted by bi-disperse flow analysis, with reasonable agreement. The average air velocity relative to the combined solid-liquid flux was monitored and found to be a strong function of the total disperse volume fraction (as oppposed to the individual volume fractions). This function is shown to reach a minimum in magnitude (at $\alpha+\nu \approx 28\%$) which corresponds to the most hindered state in disperse flow. This minimum precedes the onset of the agitated vortical flows, for which the average air velocity relative to the liquid-solid flux undergoes a sharp increase. The size and propagation speed of small and large scale structure in churn-turbulent and three-component flows remains unexplored. Future efforts should be directed on combining auto-correlation and cross-correlation measuring techniques to help us better understand the mechanics of these complicated flows.

Friction pressure drop measurements were made in vertical bubbly and particulate flows, and friction factors up to two orders of magnitude higher than pure liquid values were obtained. The two-phase friction multiplier for air-water flows was shown to attain values up to 15 times higher than the predictions given by the Lockhart & Martinelli correlations (1949).

A shielded, temperature compensated and non-intrusive Impedance Volume Fraction Meter (IVFM) was built and shown to have good spatial and temporal resolution. The dynamic calibration of the device demonstrated that the volume fraction measuring device could also be used to measure both the dispersed medium velocity and concentration. This device enabled us to carry out measurements of small and large amplitude kinematic stability and wave propagation in two-component and three-component flows.

The large deviation in measured and previously accepted values of friction pressure drops in two-component flows exemplifies the lack of detailed understanding of multi-component flow phenomena . The small amount of information available on the flow kinematics has been primarily due to the primitive stage of development of two-phase flow instrumentation. In this thesis, we show that much can be learned about the complex nature of multi-component flows with adequate instrumentation. Better understanding of the flow is much needed for cheaper handling and efficient control of multi-component flow processes. We therefore emphasize the need for further development of critical flow measuring techniques for use not only in fundamental investigations but also in the monitoring and control of practical multiphase flow processes.

REFERENCES

1. Abuaf, N., Jones, O.C. and Zimmer, G.A., 1978, "Optical Probe for Local Void Fraction and Interface Velocity Measurements", Rev. Sci. Instrum. 49 (8), Aug. 1978.

2. Acrivos, A. and Herbolzheimer, E., 1979, "Enhanced Sedimentation in Settling Tanks with Inclined Walls", J. Fluid Mech., 92, 435-457.

3. Anderson, T.B., Jackson, R., 1967, Ind. Eng. Chem. Fund., Vol. 6, No. 4, p. 527.

4. Anderson, T.B., Jackson, R., 1968, Ind. Eng. Chem. Fund., Vol. 7, No. 1, p. 12

5. Aoki, S., Inoue, S., 1965, "Fundamental Studies in Pressure in an Air-Water Two-Phase Flow in Vertical Pipes", Reprint of 2nd Japan Heat Transfer Symp., p 137.

6. Araves, A.E. and Fickas, E.T., 1979, "Progress Report on LOFT Ultrasonic Density Detector for Fuel Inlet Blowdown Measurements", Proceedings of the U.S. Nuclear Regulatory Commission, Review Group Meeting on Two-Phase Flow Instrumentation, March 13-14, 1979, Troy, N.Y., (NUREG/CP-0006)

7. Barnea, E. and Mizrahi, J., 1973, "A Generalized Approach to the Fluid Dynamics of Particulate Systems: Part I. General Correlation for Fluidization and Sedimentation in Solid Multiparticle Systems"., Chem. Engng. J. 5, pp. 171-189.

8. Batchelor, G.K., 1967, Fluid Dynamics, Cambridge University Press.

9. Batchelor, G.K., 1972, "Sedimentation in a Dilute Dispersion of Spheres", J. Fluid Mech. 1972, Vol. 52, pp. 245-268

10. Batchelor, G.K., and Janse Van Rensbury, R.W., 1986, "Structure Formation in Bi-Disperse Sedimentation", J. Fluid Mech., Vol. 166, pp. 379-407.

11. Bernier, R.N.,1981, "Unsteady Two-Phase Flow Instrumentation and Measurement", Ph.D. Thesis, California Institute of Technology, Sept. 1981

12. Bernier, R.N. and Brennen, C.E., 1983, "Use of the Electromagnetic Flow Meter in a Two-Phase Flow", Int. J. Multiphase Flow, vol. 9, No. 3, pp. 251-257

13. Boure, J.A., Bergles, A.E. and Tong, L.S., 1971, "Review of Two-Phase Flow Instabilities", ASME-AIChE Heat Transfer Conference, Aug. 15-18, 1971, Tulsa, Okla.

14. Brennen, C.E., and Kytomaa, H.K., 1984, "Three Component Test Facility and Instrumentation for Slurry Flows", Caltech Report E200.10

15. Burgess, J.M., Calderbank, P.H., 1975, "The Measurement of Bubble Parameters in Two-Phase Dispersions - I", Chem. Engng. Sc., vol. 30, pp. 743-750.

16. Clarke, N., 1983, Personal Communication

17. Coughlin, J.L. and Brennan, M.F., 1980, "Control Valves for Erosion Services", The Proceedings of the 1980 Symposium on Instrumentation and Control for Fossil Energy Processes, June 9-11, 1980, (ANL 80-62, CONF-8000602)

18. Darcy, H., Les Fontaines Publiques de la Ville de Dijon, p. 590, 1856.

19. Delhaye, J.M. and Galaup, J.P., 1977, "Hot Film Anemometry in Air-water Flow", Proc. Symp. Turbulence in Liquids, Rolla 1975, pp. 83-90.

20. Einstein, A., 1906, "Eine Bestimmung der Molekuldimensionen", Annalen der Physik, 1906, Vol. 19, pp. 289-306.

21. Fessas, Y.P. and Weiland, R.H., 1981, "Convective Solids Settling Induced by a Buoyant Phase", A.I.Ch.E. Journal, Vol. 27, No. 4, July 1981.

22. Garrard G. and Ledwidge, T.J., 1971, "Measurement of Slip Distribution and Average Void Fraction in Air-water Mixture", Australian Atomic Energy Research Establishment, 1971, Lucas Heights, Sutherland, N.S.W.

23. Gibson, R.E., 1958, "The Progress of Consolidation in a Clay Layer Increasing in Thickness with Time", Geotechnique, 18, 171-182, 1958.

24. Glass, G. and Kadlec, J., 1976, "Survey of the Behavior of BWR Pressure Suppression Systems during the Condensation Phase of a LOCA", Paper contributed to American Nuclear Society, 1976, International Conference, Nov. 15-19, 1976, Washington, D.C.

25. Grobe P.B. and Burns J.Q., 1980, "Two-and Three Phase Flow in Deep Ocean Mining Lift-pipes", Paper contributed to report on Workshop on Deep Ocean Mining Research Requirements for the 1980's. Center for Dredging Studies report No. 236.

26. Hewitt, G.F., 1972, "Role of Experiments in Two-Phase Flow with Particular Reference to Measurement Technique", Progress in Heat and Mass Transfer, Pergamon Press, No. 6.

27. Hewitt, G.F., 1978, "Measurement of Two-Phase Flow Parameters", Academic Press, New York.

28. Homsy, G.M., El-Kaissey, M.M., and Didwania, A., 1980, "Instability Waves and the Origin of Bubbles in Fluidized Beds-II", Int. J. Multiphase Flow, Vol. 6, p. 305.

29. Jackson, R., 1963, Trans. Inst. Chem. Eng., Vol. 41, p. 13.

30. Jallouk, P.A., Leavell, W.H., Shahrochi, F. and Hardy, J.E., 1979 "Advanced Instrumentation for Reflood Studies", Proceedings of the U.S. Nuclear

Regulatory Commission, Review Group Meeting on Two-phase Flow Instrumentation, March 13-14, 1979, Troy, N.Y. (NUREG/CP-0006)

31. Jenkins, J.T., and Savage, S.B., 1983 "A Theory for the Rapid Flow of Identical Smooth, Nearly Elastic Particles", J. Fluid Mech., vol. 130.

32. Jones, O.C., 1966, "Preliminary Investigation of Hot Film Anemometer in Two-Phase Flow", USAEC Report TID-24104.

33. Jones, O.C., and Zuber, N., 1975, "The Interrelation between Void Fraction Fluctuations and Flow Pattern in Two-Phase Flow", Int. J. Multiphase Flow, Vol. 2, pp. 273-306.

34. Jones, O.C. and Delhaye, J. M., 1976, "Transient and Statistical Measurement Techniques for Two-Phase Flows: A Critical Review", Int. J. Multiphase Flow, Vol. 3, pp. 89-113.

35. Kynch, G.J., 1952, "A Theory of Sedimentation", Trans. Faraday Society, 1952, Vol. 48, pp. 166-176.

36. Kytomaa, H.K., and Brennen, C.E., 1986, "Measurement of Friction Pressure Drops in Vertical Slurry and Bubbly Flows", Presented at ASME Cavitation and Multiphase Flow Forum.

37. Kytomaa, H.K., and Brennen, C.E., 1986, "Some Observations of Flow Patterns and Statistical Properties of Three Component Flows", Presented at ASME International Symposium on Slurry Flows.

38. van der Lans, R., "Hydrodynamics of a Bubble Column Loop Reactor", Ph.D. Thesis, Technische Hoges School, Delft, Holland, 1985.

39. Lighthill, M.J. and Whitham, G.B., 1955, "On Kinematic Waves, I-Flood Movement in Long Rivers", Proceedings of the Royal Society, 1955, Vol. 229, pp. 281-316.

40. Lighthill, M.J. and Whitham, G.B., 1955, "On Kinematic Waves, II-A Theory of Traffic Flow on Long Crowded Roads, 1955, Vol. 6, pp. 317-347.

41. Lockhart, R.W. and Martinelli, R.C., 1949, "Proposed Correlation of Data for Isothermal Two-Phase, Two-Component Flow in Pipes", Chem. Engng. Progress 1940, Vol 45, No. 1, pp. 39-48.

42. Lockett, M.J. and Al-Habbooby, H.M., 1973, "Differential Settling by Size of Two-Particle Species in a Liquid", Trans. Instr. Chem. Engrg., vol. 51, pp. 281-292.

43. Lockett, M.J. and Al-Habbooby, H.M., 1974, "Relative Particle Velocities in Two-Species Settling", Powder Technol., vol. 10, pp. 67-71.

44. Nakoryakov, V.E., Kashinsky, O.N., Burdukov, A.P., Odnoral, V.P., 1981, "Local Characteristics of Upward Gas-Liquid Flows", Int. J. Multiphase Flow., Vol. 7, pp. 6371

45. Olsen, H.O., 1967, "Theoretical and Experimental Investigation of Impedance Void Meters", Institutt for Aromenergi, Kjeller Research Establishment, August 1967, Kjeller, Norway.

46. Papoulis, A., 1965, "Probability, Random Variables, and Stochastic Processes, McGraw Hill.

47. Richardson, J.F., 1971, Fluidization (editors Davidson J.F. and Harrison, D.), Academic Press.

48. Roco, M.C., 1983, "Analytical Model and Experimental Studies on Slurry Flow and Erosion in Pump Casings", Slurry Transportation, STA, Vol. 8, pp. 263-276, 1983.

49. Savage, S.B., 1979, "Gravity Flow of Cohesionless Granular Material in Chutes and Channels", J. Fluid Mech., vol. 92, part 1.

50. Schrock, V.E. and Selph, F.B., 1963, "Reactor Heat Transient Research. An X-ray Densitometer for Transient Steam-Void Measurement", Univ. California Institute of Engineering, Report No. SAN-1005, TID-4500, 1963.

51. Scott, R.F., 1986, "Solidification and Consolidation of a Liquefied Sand Column", paper submitted to Soils and Foundations (Journal of Japanese Society of Soil Mechanics and Foundation Engineerings).

52. Slattery, J.C., 1967, A.I.Ch.E. Journal, Vol. 13, p. 1066.

53. Smith, T.N., 1966, "The Sedimentation of Particles Having a Dispersion of Sizes", Trans. Inst. Chem. Engrs., Vol. 44, pp. 153-157.

54. Symington, W.A., 1978, "Analytical Studies of Steady and Non-Steady Motion of a Bubbly Liquid", Ph.D. Thesis, California Institute of Technology, May 1978.

55. Taylor, D.G. Porter, E.H. and Orvis, W.J., 1979, "PBF Radiation Hardened Gamma Densitometer", Proceedings of the U.S. Nuclear Regulatory Commission, Review Group Meeting on Two Phase Flow Instrumentation, March 13-14, 1979, Troy, NY (NUREG/CP-0006)

56. Terzaghi, K., 1943, "Theoretical Soil Mechanics.", Wiley, New York

57. Toral, H., 1981, "Study of the Hot-Wire Anemometer for Measuring Void Fraction in Two Phase Flow", J. Phys. E., vol. 14, pp. 822-827

58. Wallis, G.B., 1962, "A Simplified One-Dimensional Representation of Two Component Vertical Flow and Its Application to Batch Sedimentation", Proc. Symp. on Interaction Between Fluid and Particles, Inst. of Chem. Engrs., 1962, London.

59. Wallis, G.B., 1969, One Dimensional Two-Phase Flow, McGraw-Hill, New York

60. Whitaker, S., 1973, "The Transport Equations for Multiphase Systems", Chem. Eng. Sci., Vol. 28, p. 139.

61. van Wijngaarder, L., 1976, "Hydrodynamic Interaction between Gas Bubbles in Liquid", J. Fluid Mech., Vol. 77, part 1, pp. 27-44.

62. Zenz, F.A., 1971, Fluidization (editors Davidson J.F. and Harrison, D.), Academic Press

63. Zuber, N. Staub, F.W., Bijwaard, G and Kroeger, P.G., 1967, "Steady State and Transient Void Fraction in Two-Phase Flow Systems - Final Report for the program of Two-Phase Flow Investigation", EURAEC GEAP-5417 Volume I, January 1967.

64. Zuber, N., 1964, "On the Disperse Two-Phase Flow in Laminar Flow Regime", Chemical Engineering Science, 1964, Vol. 19, pp. 897-917.

65. Zuber, N. and Staub, F.W., 1966, "The Propagation and Wave Form of the Vapor Volumetric Concentration in Boiling Forced Convection Systems Under Oscillatory Conditions", Journal of Heat Transfer, 1966, vol. 9, pp. 871-895.